**The Dissertation Committee for Ye Chen**
**Certifies that this is the approved version of the following dissertation:**

# Design of Magneto-Inductive Waveguide for Sensing Applications

**Committee:**

Dean P. Neikirk, Supervisor

Hao Ling

Sharon L. Wood

Andrea Alù

Neal A. Hall

# Design of Magneto-Inductive Waveguide for Sensing Applications

**by**

**Ye Chen, B.E.; M.E.; M.S.E.**

**Dissertation**

Presented to the Faculty of the Graduate School of

The University of Texas at Austin

in Partial Fulfillment

of the Requirements

for the Degree of

**Doctor of Philosophy**

**The University of Texas at Austin**

**May 2014**

*To My Parents*

# Acknowledgements

First and foremost, I would like to express my deepest gratitude to my Ph.D. advisor, Dr. Dean P. Neikirk, for his guidance, patience, and support throughout my graduate study. He has been an invaluable resource as an advisor. I benefited much from discussions with him, and I would not have been able to complete this dissertation without his guidance. He is very patient, affable, and accommodating. I am privileged to have had the opportunity to work with him.

I would also like to thank Praveen Pasupathy for his helpful suggestions and technical assistance. He helped me to be at ease during the most difficult part of my work. I would also like to thank the other members of "Team Neikirk" for their assistance in experiments and for always being available to answer my questions.

I thank Dr. Sharon Wood and her group at the Ferguson Structural Engineering Laboratory for giving me insight into structural health monitoring, the topic of my research.

Finally, I would like to express gratitude to my parents for their continual love and support throughout my life and studies. This dissertation is dedicated to them.

# Design of Magneto-Inductive Waveguide for Sensing Applications

Ye Chen, Ph.D.

The University of Texas at Austin, 2014

Supervisor: Dean P. Neikirk

This dissertation has been motivated by the increasing application of sensing technologies in structural health monitoring. Many wireless sensor techniques exist for structural health monitoring while a challenge faced is the finite lifetime of batteries. The objective of this dissertation is to develop passive wireless technology to provide early warning of conditions that damage the structure. In this dissertation, sensing mechanism is proposed based on time and frequency domain characteristics of magneto-inductive (MI) waves. Experimental results are also presented to demonstrate the sensing mechanism.

MI waves are predominantly magnetic waves that are supported in periodic arrays of magnetically coupled resonators and propagate within a narrow frequency band around the resonant frequency. The array is to be embedded in a structure and different types of transducers can be integrated for different sensing applications. With the onset of structure defect, the transducer introduces an impedance discontinuity that generates reflected MI waves along the array, which are monitored and processed by Smoothed Wigner-Ville distribution (WVD) to extract time-of-flight for frequency components in the narrow passband. The transmission and reflection coefficients of MI waves are also investigated based on the lumped-element circuit

model of the array. Based on MI waves travel time, amplitude and group velocity, the position and severity of structure defect are decided. The sensing mechanisms for different distribution of defects are proposed.

The validity of the sensing mechanism is examined in experiments. The guided wave testing is implemented in one-dimensional square-shaped printed spiral resonators with Q-factor of 161 at 13.6 MHz. It demonstrates that low MI waves propagation loss is achieved with value of 0.098 dB per element at mid-band with center-to-center distance of half an inch. A pitch-catch measurement system is built to capture traveling MI signal in resonant element and extract group velocity, and a pulse-echo measurement system is designed to monitor reflected MI signal and locate structure discontinuity. In both measurement systems, MI waves are excited with wide bandwidth voltage pulse, and a digitizer is attached to sense the MI signal in a specific resonant element circuit. A baseline signal is obtained from the healthy state to use as reference and comparison with the test case using pitch-catch system. The test signal subtracted from baseline signal infers the structure damage information with time and frequency domain characteristics. It can offer an effective method to estimate the structure discontinuity location, severity and type of damage. The experimental results are consistent with the theoretical predictions. At the end, future directions for the research to integrate with other technologies are suggested.

# Table of Contents

# List of Tables

# List of Figures

# Chapter 1 Introduction

## 1.1 BACKGROUND

The properties of guided electromagnetic waves have been investigated in great detail over the last several decades, from coaxial lines to optical fibers. Many transducers, resonators, couplers, filters, directional couplers, etc. have been designed to exploit the properties of guided waves. In recent years, the so-called magneto-inductive (MI) waves were proposed when investigating the properties of metamaterials [1] and the interaction between the resonant elements [2, 3]. MI waves are dispersive waves, and the periodic array of magnetically coupled resonant elements has been shown to theoretically support the propagation of MI waves [2]. Recent research has characterized the behavior and properties of MI waves, the design of waveguide elements, coupling mechanisms, dispersion relationships, and different MI waveguide structures [4–9].

The first proposed MI waveguide consisted of a line of equally spaced, capacity-loaded metallic loops and was proven experimentally by Wiltshire *et al*. [6]. A one-dimensional array of Swiss Rolls was also demonstrated to support the propagation of MI waves [8]. Freire *et al.* built a MI waveguide with a periodic array of metallic split-squared ring resonators [10]. In addition to the one-dimensional waveguide, investigations were also concerned with the arrays of identical elements in two- and three-dimensions [11–14].

The subject of intensive investigation in recent memory involves the development of the MI waveguide structure and design of MI devices for different applications. The MI waveguides have been designed for applications as phase shifters, imaging lenses, MI cables, communication channels, and pipeline monitoring [4, 10, 12, 15–23]. Freire *et al.* proposed planar MI transducers as a delay line and two parallel planar arrays of broadside coupled split-ring

resonators (BC-SRRs) for subwavelength imaging [12]; Nefedov *et al.* incorporated the MI waveguide into the design of a broadband phase shifter [22]; Chan *et al.* explored the potential for MI waveguides to be used as one- and two-dimensional data-transfer channels [24]; Solymar *et al.* designed the detectors for magnetic resonance imaging based on the propagation of MI waves [25]; Syms *et al.* proposed thin-film MI cables using single-turn inductors and parallel-plate capacitors [26]; Sun *et al.* used magneto-induction to accomplish underground wireless communication and pipeline monitoring [17–19, 23]; and we adopted the MI waveguide constructed by inductively coupled passive wireless sensors for sensing the onset of corrosion in reinforced concrete [27–29].

The main objective of the research is to develop defect sensing mechanism with MI waveguide and demonstrate suitability for SHM applications.

## 1.2 MOTIVATIONS

The proposed dissertation research has been motivated by an increased application of sensing technologies in structural health monitoring, specifically as it relates to the corrosion of embedded steel reinforcements. It is a serious problem worldwide since corrosion degrades the integrity of the steel, produces cracks and spalling, thereby decreases the lifespan of an infrastructure. Each year $22.6 billion are spent on replacing and repairing structurally deficient highway bridges due to corrosion [30]. The indirect cost resulting from traffic delays and lost productivity are approximately ten times this amount. Structures located in the coastal marine environment are even more susceptible. Early detection of corrosion, therefore, not only extends the service lift of structures but also significantly decreases the costs of maintaining those structures. Both wired and wireless sensor systems have also been developed to addresses the structural health problems by research groups and company.

The University of Texas at Austin developed the passive wireless Electronic Structural Surveillance (ESS) platform to monitor corrosion conditions in civil infrastructure [27, 35–42]. The ESS platform uses two circuits magnetically coupled through the inductive reader and tag coils. The ESS sensors operate using inductive coupling between a passive embedded sensor and an external reader. The embedded sensors provide real-time local information about existing reinforced concrete structures. The passive wireless corrosion sensors are effective in monitoring corrosion, and they are extremely simple and cost efficient for large-scale deployment. Since the sensors are battery-free and interrogated via inductive coupling, extending the read range of these sensors is a challenge.

ElectraWatch developed the Embedded Corrosion Instrument (ECI), which provides early warnings of conditions that damage steel reinforcement, leading to cracking, spalling, and other deterioration of concrete structures [31]. All embedded ECIs are components of a wired local-area network. Coaxial wires are employed in this structural monitoring system for communication between sensors and repositories. Wired network can guarantee that measurement data are collected and distributed reliably. But wires have to be deployed all over the structure. Their installation can be expensive and maintenance labor-intensive.

The Mote Wireless Sensor platform developed by University of California–Berkeley received great attention because both software (TinyOS) and hardware are open source [32]. Systems based on Mote have been deployed in a number of large-scale monitoring applications. For example, over 150 Motes have been implemented to monitor the weather and nesting condition of birds on Great Duck Island, Maine [33]. Fifty-nine nodes have been distributed over the span and tower of the Golden Gate Bridge to supervise acceleration of the structure [34]. Such studies have demonstrated that the high cost of installing wired sensors can be reduced by

taking advantage of wireless sensors, but feasibility and widespread adoption of wireless sensors is constrained by reliable power supply.

Therefore, the objective of this research is to develop a new kind of sensing technology that is battery-free, low-cost, and has the ability to cover a relatively large area. The low-loss MI waveguide is proposed for SHM sensing applications and shows great potential in the area. First, the MI waveguide is constructed by passive resonators, which are battery-free and low-cost to fabricate. Second, the MI waveguide has larger coverage than a reader-tag pair due to a line of coupled resonators. Third, the MI waves can be excited in a prescribed, repeatable manner and received using coils. The propagating waves can be examined to estimate the location, severity, and even type of damage with a choice of transducers.

The dissertation focuses on a design of the MI waveguide that generates and receives guided waves, explains how MI waves propagate along with the signal processing methodology to process MI waves. The one-dimensional MI waveguide lumped-element model for MI wave excitation and sensing is established. The validity of the model is examined in extensive simulations and experiments. In sum, the model is exploited to furnish design guidelines for the low-loss MI waveguide and sensing mechanism.

## 1.3 SCOPE OF RESEARCH

The methodology is to design one-dimensional low-loss MI waveguides and develop sensing mechanisms to monitor and locate defects. First, I will develop a one-dimensional low-loss waveguide to support MI waves. Second, I will establish the relationship between defects and the characteristics of propagating MI waves. Finally, I will build the measurement system and execute the experiments and processing to validate theoretical predictions.

Chapter 2 designs the inductively coupled resonator consisting of low-loss MI waveguides and provides a detailed explanation of MI wave theory. The circuit model of the resonant element is given to help us optimize quality factor and magnetism. MI wave characteristics are understood by establishing circuit models, obtaining characteristic impedance, and solving dispersion relationship and group velocity. The effects of circuit component tolerance on the propagation of MI waves are also discussed.

Chapter 3 investigates the sensing mechanism based on different MI waveguide structures. The discontinuities are introduced by variance of circuit components in the circuit model of MI waveguides. MI waveguides with different distribution of defects are discussed. The reflection and transmission coefficients and group-velocity change due to impedance discontinuities are studied, and sensing mechanisms are proposed.

Chapter 4 builds measurement systems and verifies the design of the low-loss MI waveguide and proposed sensing mechanism. The experimental setups are designed for both frequency- and time-domain measurements. The measured incident and reflected MI waves caused by intended defects are processed by Time-Frequency Representation (TFR) methods to validate the sensing mechanism.

Chapter 5 summarizes the findings of the research and identifies possible topics for future study.

# Chapter 2 Design of Low-Loss Magneto-Inductive Waveguide

## 2.1 INTRODUCTION

The periodic structure consists of a set of magnetically coupled resonators that can support the propagation of MI waves within a narrow frequency band around the resonant frequency of the individual element. A key requirement in developing the MI waveguide is to demonstrate low propagation loss that depends on the quality factor of element and the strength of coupling between elements. Since traveling MI waves were first demonstrated in [6], much has been published about MI waveguides based on different individual resonators. Capacitively loaded loops [6, 17, 19], Swiss rolls [8], single-layer printed spiral coils (PSC) [24, 43–45], double-layer PSC [9], varactor-loaded split-ring resonators [46], capacitively loaded split-pipes [47], double-sided printed inductor and capacitors on interlayer dielectric, [48] and various kinds of split ring resonators [10, 49] have been proposed in the form of one- or two-dimensional periodic arrays to support MI waves. They are modeled using lumped-element circuits and operate at frequencies between 20 MHz to 4.5 GHz for different applications. The maximum quality factor designed is 123 with square split-ring resonators working at 240 MHz [24]. Attenuation as small as 0.12 dB per element at mid-band is achieved by a line of double-layer PSC with a resonant frequency of 156.4 MHz, $Q$-factor of 110, and spacing of 2.5 mm [9].

The aim of this chapter is to design high $Q$-factor resonant components to construct MI waveguides. First, the resonator geometry with lumped-element circuit parameters of individual element are provided and measured; secondly, MI wave theory is reviewed, and MI waveguides based on the designed resonator are studied; and finally, statistics about the effect of waveguide geometry on MI waves are discussed.

## 2.2 DESIGN OF PRINTED SPIRAL COILS

The MI waveguide is a periodic magnetically coupled resonator array. The wave-guiding action occurs due to magnetic coupling between elements. This section describes the size and geometry of printed square spiral inductors and design specifications, including self-resistance, self-inductance, and capacitance.

### 2.1.1 Geometry of Printed Spiral Coils

To make use of MI waveguides for sensing application, it is desirable to adopt a high-$Q$ component with strong magnetic coupling to achieve low propagation loss and a strong signal. As discussed in [28], capactively loaded loops is a candidate with a good form factor and a well understood design methodology. The solenoid coils are easy to make and the quality factor can reach 115 at 9.32 MHz by wrapping an enamel-coated 22AWG wire around a two-inch plastic cylinder for five turns, and minimum loss reaches 0.16 dB per tag when they are placed coaxially with a center-to-center distance of half an inch [28].

In this work, the single-layer square-shaped print spiral coil (PSC) with a lumped capacitor is adopted as the resonant element. That is because a printed PCB resonator is used to achieve a quality factor of 150 first and the design methodology is well established. The performance of coil can be optimized by adjusting its geometric parameters. Furthermore, the square-shaped PSC is comparatively easy to fabricate and is low-cost. It also holds the potential to be fabricated in conjunction with sensors or signal processing circuits in the same board. We limit our design to single-layer PSC, since internal parasitic capacitance of a multilayered structure is much larger and may limit the choice of resonant frequency of an individual element. Thus the single-layer printed spiral resonators are used to construct the MI waveguide.

The initial geometry of a single-layer square-shaped PSC is shown in Figure 2.1. The resonant element is designed to operate around 13.56MHz and have a quality factor greater than 120. The resonant frequency is chosen at 13.56MHz, since one of the potential applications is in the RFID sensor system.

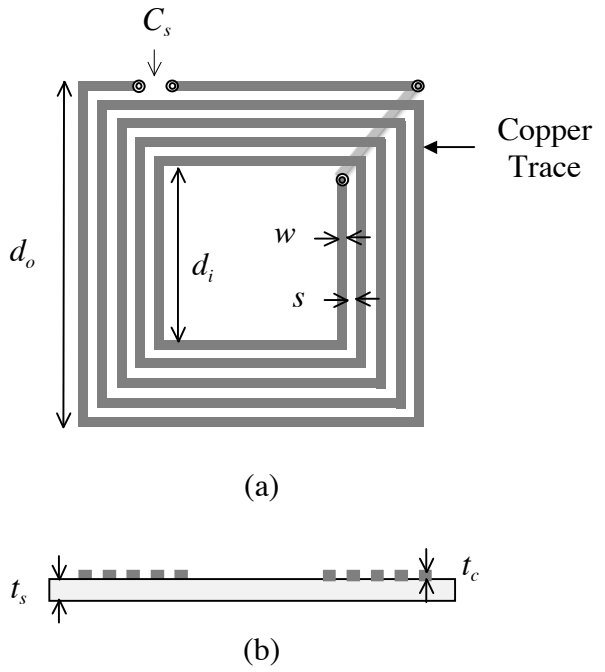


Figure 2.1 Geometry of printed spiral coil: (a) Top view (b) Side view

Figure 2.1 (a) and (b) are the top view and side views of a single-layer square-shaped PSC respectively. The dark grey portion indicates a copper trace with width $w$ and thickness $t_c$ = 43μm. The light grey trace on the right upper corner is a copper trace on the rear side connecting inner and outer turns. The copper spiral inductor is lithographically defined on the FR4 dielectric substrate with a measurement of 5.08 cm x 5.08 cm (2 inches x 2 inches) and a thickness of $t_s$ = 1.6mm. The outer diameter $d_o$ is chosen as 4.57 cm (1.8 inch). The inner diameter $d_i$ depends on outer diameter $d_o$, a number of turns $n$ and spacing between turns $s$. An externally lumped capacitor $C_s$ with capacitance of 101 pF is soldered between two vias along one side of the PSC.

All geometric parameters and corresponding symbols are listed in Table 2.1. The lumped-element circuit model based on the geometry parameters is described in the following section.

Table 2.1 Geometrical parameters and symbols of a single-layer PSC

| Parameter | Symbol |
|---|---|
| Number of turns | $n$ |
| Coil outer diameter | $d_o$ |
| Coil inner diameter | $d_i$ |
| Trace width | $w$ |
| Spacing between trace | $s$ |
| Trace thickness | $t_c$ |
| Substrate thickness | $t_s$ |
| Relative permittivity of trace | $\mu_c$ |
| Relative permittivity of the substrate (FR4) | $\varepsilon_{rs}$ |

### 2.1.2 Lumped-Element Circuit Model

We model the single-layer PSC with external capacitor $C_s$ as a series circuit shown in Figure 2.2. It is a resonant L-C tank circuit with lumped elements — parasitic resistance of PSC $R_p$, self-inductance of PSC $L_s$, and an external capacitance $C_s$.

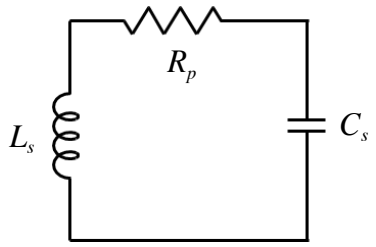


Figure 2.2 Lumped-element circuit model of PSCs

The parasitic capacitance of PSC is not taken into consideration since the value is much smaller than the external capacitance. An empirical approach combing of theoretical, simulation and measurement results is used to find the parasitic capacitance of the PSC [50]. Figure 2.3 shows the side view of two traces of PSC turns. The parallel plate parasitic capacitor forms between conductor side walls with air $C_{pc}$ and FR4 substrate dielectrics $C_{ps}$.

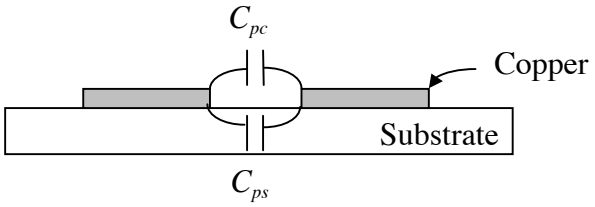


Figure 2.3 Side view of a PSC conductive trace

The total parasitic capacitor is the sum of $C_{pc}$ and $C_{ps}$ [50],

$$C_P = C_{pc} + C_{ps} = (\alpha\varepsilon_{rc} + \beta\varepsilon_{rs})\varepsilon_0 \frac{t_c}{s} l_g \tag{2.1}$$

where $(\alpha, \beta) = (0.9, 0.1)$, $\varepsilon_{rc}$ and $\varepsilon_{rc}$ are the relative dielectric constants of air and FR-4 substrate with $(\varepsilon_{rc}, \varepsilon_{rs}) = (1, 4.4)$, $t_c$ is the conductor thickness, $s$ is the gap between two traces and $l_g$ is the length of the spiral coil gap given in (2.2),

$$l_g = 4(d_o - w \cdot n)(n-1) - 4s \cdot n(n+1) \tag{2.2}$$

Given the outer diameter of 4.57 cm, the parasitic capacitance curve as a function of a number of turns is shown in Figure 2.4. The trace width and spacing are designed to be the same. The square spiral goes from the edge to the center. The capacitance increases as the number of turns increases. The minimum width and gap are chosen 0.25 mm. It can go up to 45 turns within the substrate area. The estimated maximum parasitic capacitance is around 8 pF, which is much less than the soldered external capacitance of 101pF that makes the current flow through the

external capacitor. Thus the parasitic capacitance is not considered in the circuit model of the PSC.

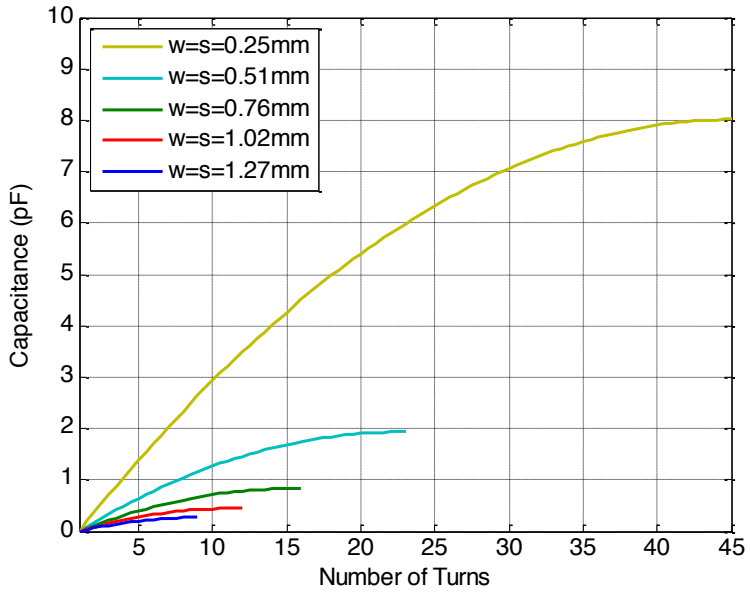


Figure 2.4 Simulated self-capacitance vs. Number of turns

To make the resonant frequency of 13.56 MHz, the geometry of single-layer PSC is designed to have self-inductance of 1.36 μH given external capacitance of 101 pF. Several approximation methods have been proposed to approximate self-inductance of a PSC [51]. We adopt simplified equation from [50] to evaluate the self-inductance of square-shaped spiral coils,

$$L_s = \frac{1.27\mu_0 n^2 d_{avg}}{2}\left[\ln\left(\frac{2.07}{\varphi}\right) + 0.18\varphi + 0.13\varphi^2\right] \tag{2.3}$$

where $\mu_0$ is permeability of free space, $n$ is the number of turns, $d_{avg}$ is the mean of coil outer diameter $d_o$ and inner diameter $d_i$, $\varphi$ is a parameter known as the fill factor expressed in (2.4). When all the turns are concentrated on the perimeter and the turns go all the way to the center of the coil, its value changes from 0 to 1.

$$\varphi = \frac{d_o - d_i}{d_o + d_i} \tag{2.4}$$

The self-inductance variances with different number of turns and different set of trace width and spacing are shown in Figure 2.5. The outer diameter $d_o$ is fixed at 4.57 cm. The black dash line corresponds to a self-inductance of 1.36 μH. When $w$ and $s$ are 0.25 mm, 0.51 mm, 0.76 mm, 1.02 mm and 1.27 mm respectively, the number of turn should be 3, 3.25, 3.75, 4 and 4.75. In addition to resonant frequency, quality factor is another parameter to be optimized, since high-Q resonators help to decrease propagation loss of MI waves.

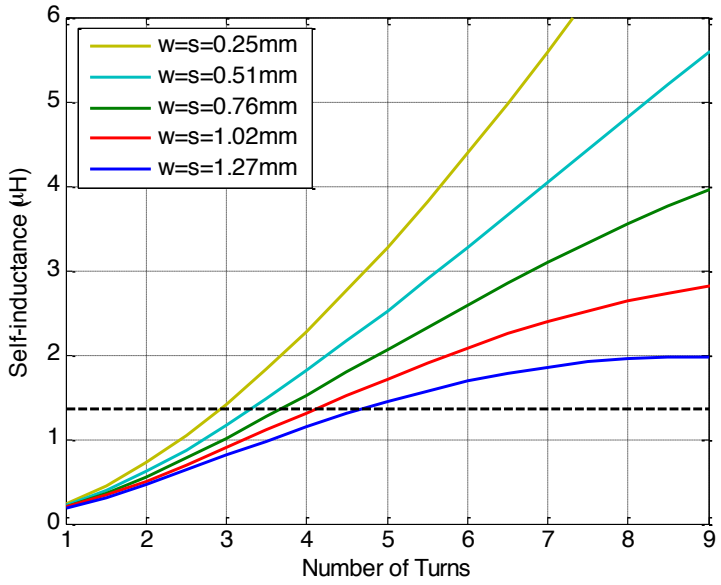


Figure 2.5 Simulated self-inductance vs. Number of turns

For an ideal series RLC circuit, the quality factor can be estimated by $\omega_0 L/R$. With known resonant frequency and self-inductance, the parasitic resistance $R_p$ determines the value of the quality factor.

The parasitic resistance $R_p$ is dominated by dc resistance $R_{dc}$ at low frequency, which depends on the total length of the conductive trace $l$, resistivity of the conductive material $\rho_c$, and its thickness $t_c$ as expressed as,

$$R_{dc} = \rho_c \frac{l}{wt_c} \tag{2.5}$$

where the total length of a square-shaped PSC is given by,

$$l = 4nd_o - 4nw - (2n+1)^2(s+w) \tag{2.6}$$

where $n$ is the number of turns, $w$ and $s$ are the copper trace width and gap between turns respectively. When the frequency goes up, the skin effect should be taken into account, and then the parasitic resistance $R_p$ becomes [50],

$$R_p = R_{dc}\frac{t_c}{\delta\left(1-e^{-t_c/\delta}\right)} \tag{2.7}$$

where $\delta$ is the skin depth related to metal resistivity $\rho_c$ and frequency $f$,

$$\delta = \sqrt{\frac{\rho_c}{\pi\mu_c\mu_0 f}} \tag{2.8}$$

With the same geometric parameters used to calculate self-inductance, the variation of parasitic resistances with a different number of turns are simulated and presented in Figure 2.6. Given the geometries with self-inductance of 1.36 μH, the corresponding parasitic resistances are 2.1 Ω, 1.1 Ω, 0.79 Ω, 0.58 Ω and 0.48 Ω for $w$ and $s$ are 0.25 mm, 0.51 mm, 0.76 mm, 1.02 mm and 1.27 mm respectively. Thus we have quality factors 55, 104, 149, 196 and 242. The later three geometries are candidates that have a quality factor of more than 120, and the highest quality factor with a value of 242 is achieved by 4.75-turn coil with $w$ and $s$ equal to 1.27 mm.

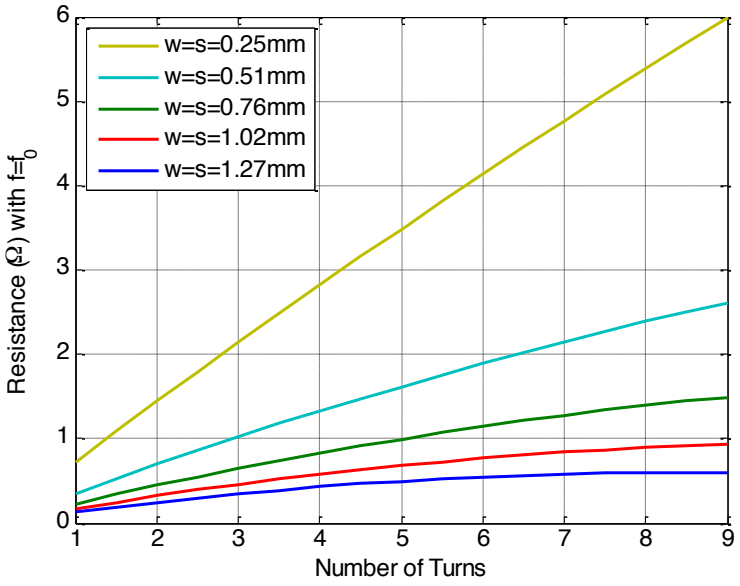


Figure 2.6 Simulated parasitic resistance vs. Number of turns

Since the MI wave-guiding action along an array of printed spiral resonators occurs due to magnetic coupling between elements, the coupling factor is also critical to low propagation loss. It is defined by formula $\kappa = M/\sqrt{(L_1 L_2)}$ , where $M$ is mutual inductance between two inductors. It not only relates to PSC geometry but also the center-to-center distance between them. For coaxially spaced square-shaped PSCs shown in Figure 2.7, the partial inductance method is adopted to estimate the mutual inductance [52].

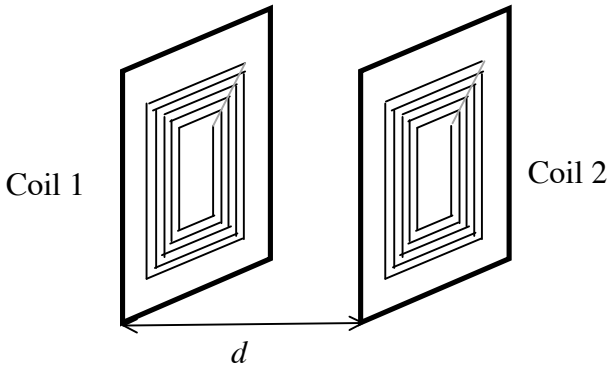


Figure 2.7 Geometry of coaxially spaced PSCs

where $d$ is the center-to-center distance between two coils. The $n$-turn single-layer PSCs are simplified as $4n$ filaments. According to partial inductance method [52], the total mutual inductance is the sum of all positive mutual inductances between parallel filaments and all negative mutual inductances between parallel filaments. When current flow in two conductors exhibits the same directions, the mutual inductance is positive, otherwise negative.

Figure 2.8 is a simplified $n$-turn ($n$=5) square PSC, and all segments are assigned serial numbers from 1 to 20. Numbering increases from outside to inside. The odd-numbered segments are all perpendicular to even-numbered segments.

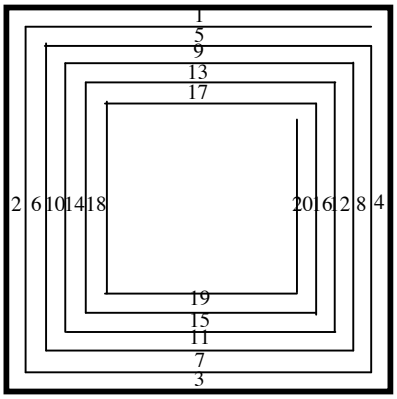


Figure 2.8 Schematic diagram of five-turn square PSC

If two single-layer PSCs are placed coaxially with a center-to-center distance of $d$, the currents in segment pairs—segment $i$ in Coil 1 and segment $j$ in Coil 2 ($i = m+4(n_1-1)$ & $j = m+4(n_2-1)$, $m$ = 1,2,3,4, $n_1$ = 1,2,…,5, $n_2$ = 1,2,…,5) are in the same direction and mutual inductions are positive, while the current flow in segment $i$ in Coil 1 ($i$ = 1+4($n$-1) or 2+4($n$-1), $n$=1,2,…5) is opposite in direction to the current flow in parallel segment $j$ in Coil 2 ($j$ = 3+4($n$-1) or 4+4($n$-1), $n$=1,2,…5), which results in negative mutual inductance.

With the partial inductance method [52], the total mutual inductance is equal to the sum of the positive mutual inductance ($M_{i,i\pm4n}$, $i$ = 1,2,…,20 and $n$ = 0,1,…4) and the negative mutual

inductance ($M_{i,i+2\pm4n}$, $i$ = 1,2,…,20 and $n$ = 0,1,…4), where $M_{i,j}$ means the mutual inductance between segment $i$ in Coil 1 and segment $j$ in Coil 2. $M_{i,j}$ between two parallel segments depends on their lengths and the geometric mean distance (GMD) between them. A pair of parallel segments with different lengths is shown in Figure 2.9.

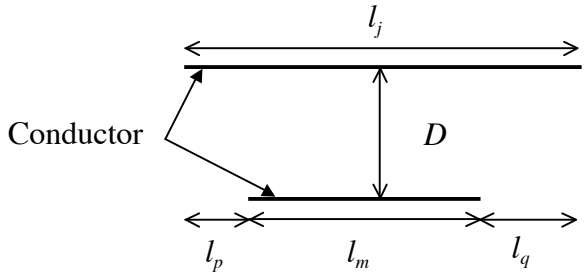


Figure 2.9 Geometry of two parallel filaments

Consider two filaments geometry represented schematically in Figure 2.9, where two parallel filaments of length $l_j$ and $l_m$ are separated by distance $D$. Filament $j$ is longer than filament $m$, and the lengths satisfy $l_j = l_p + l_m + l_q$. The mutual inductance between them can be estimated by [52]

$$M_{j,m} = \frac{1}{2}\left(M_{m+p} + M_{m+q} - M_p - M_q\right) \tag{2.9}$$

where $M_i$ ($i$=$m$+$p$, $m$+$q$, $p$ or $q$) is the mutual inductance between two filaments with the same length ($l_i$=$l_m$+$l_p$, $l_m$+$l_q$, $l_p$ or $l_q$), and can be calculated by

$$M_i = 2l_iQ_i \tag{2.10}$$

where $Q_i$ is a mutual inductance parameter expressed as

$$Q_i = \ln\left(\left(l_i/GMD\right) + \left(1 + \left(l_i^2/GMD^2\right)\right)^{1/2}\right) - \left(1 + \left(GMD^2/l_i^2\right)\right)^{1/2} + \left(GMD/l_i^2\right) \tag{2.11}$$

where GMD is approximately equal to the distance $D$ between the conductor centers. The total mutual inductances $M$ between two uniform coaxial 5-turn PSCs are calculated by summing up

positive mutual inductances and negative mutual inductances between parallel segments. Since each straight conductor is simplified as filament, the GMD between two parallel conductors is approximately equal to the center-to-center distance. The mutual inductance between each pair of parallel conductors is calculated by (2.10). The coupling factor is obtained by normalizing the total mutual inductance with Coil 1self-inductance $L_1$ and Coil 2 self-inductance $L_2$.

Based on quality factor results above, the best three configurations are picked to calculate the coupling factor curve. The three configurations are 3.75-turn PSC with $w$ and $s$ of 0.76 mm, a 4-turn PSC with $w$ and $s$ of 1.02 mm and 4.75-turn PSC with $w$ and $s$ of 1.27 mm. The relationship between coupling factor $\kappa = M/\sqrt{(L_1 L_2)}$ and distance $d$ is presented in Figure 2.10.

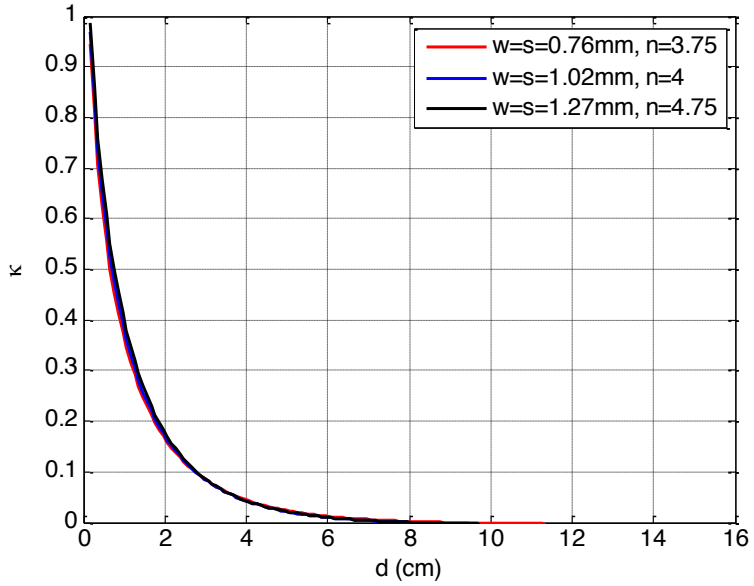


Figure 2.10 Simulated coupling factor vs. Axial spacing

Figure 2.10 shows that the coupling factor curves for three candidates, all curves decreases sharply as the gap $d$ becomes larger and the value is roughly proportional to the inverse of distance. The coupling is negligible when the gap goes above 8 cm. Since there is no big difference between the three curves, the optimal geometry is a 4.75-turn PSC with $w$ and $s$ of 1.27 mm. The geometry details are listed in Table 2.2.

Table 2.2 Geometrical parameters of single-layer PSC

| Parameter | Symbol | Value |
|---|---|---|
| Number of turns | $n$ | 4.75 |
| Coil outer diameter (cm) | $d_o$ | 4.57 |
| Coil inner diameter (cm) | $d_i$ | 2.54 |
| Trace width (mm) | $w$ | 1.27 |
| Spacing between trace (mm) | $s$ | 1.27 |
| Trace thickness (μm) | $t_c$ | 43 |
| Substrate thickness (mm) | $t_s$ | 1.6 |
| Relative permittivity of trace | $\mu_c$ | 1 |
| Relative permittivity of the substrate (FR4) | $\varepsilon_{rs}$ | 4.4 |

### 2.1.3 Experimental Results

To verify the designs above, the 4.75-turn printed square spiral coils are fabricated on 1.6 mm thick FR-4 substrate. The design is shown in Figure 2.11.

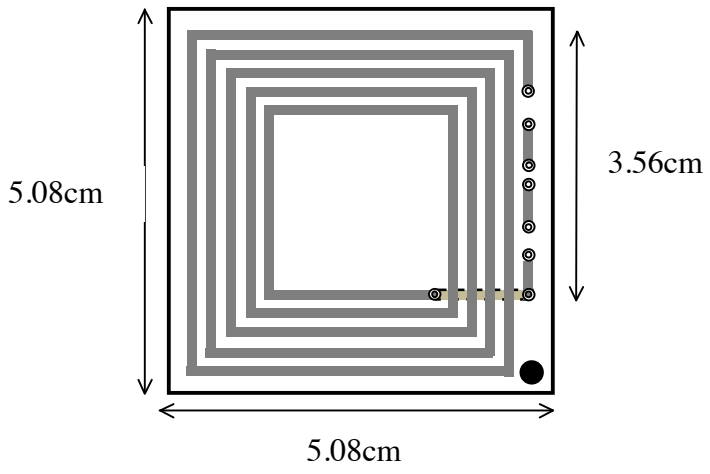


Figure 2.11 Geometry of PSC

The size of this single PCB board is 5.08 cm by 5.08 cm. The gray portion is the metal trace with a width *w* of 1.27 mm. The gap *s* between turns is 1.27 mm. To bridge inner terminal and outer turn, several pieces of copper trace with a total length of 3.56 cm are printed and the three gaps between them can be shorted by jumper wire or inserted with lumped external capacitor, characteristic impedance, or power source as needed. The capacitor is required to make a resonant element. The power source connects to the driver coil to excite the MI waves. When a specific element serves as the end termination of an MI waveguide, the characteristic impedance of the MI waveguide is inserted as the load to minimize end reflections. The gray rectangle with dashed outline is printed on the bottom side of the board to connect the terminals at inner and outer turns, as shown in Figure 2.11. At the right lower corner, the black dot is a hole designed for inserting plastic spacers with specific length to construct the MI waveguide.

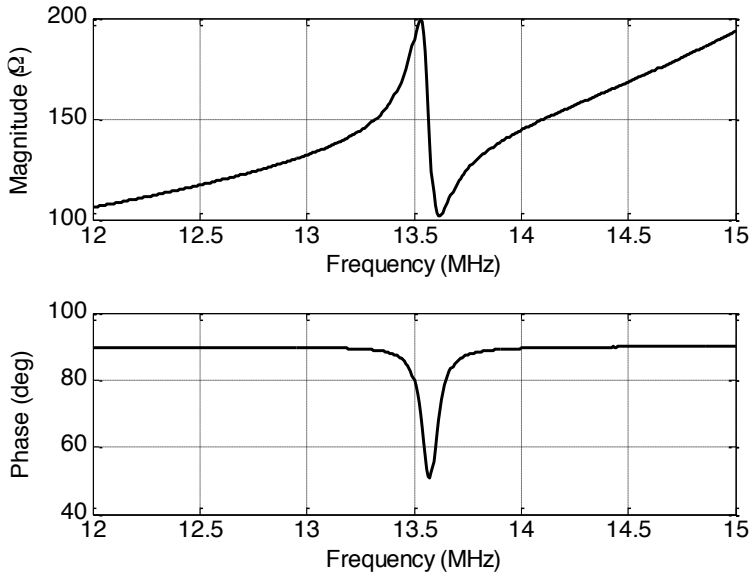


Figure 2.12 Input impedance of PSC

Figure 2.12 shows the input impedance of PSC with an external capacitor of 101 pF by the HP 4194A Impedance/Gain-Phase Analyzer. The resonant frequency $f_0$ and quality factor $Q_0$ can be obtained by the input impedance characteristics. The resonant frequency $f_0$ is the point

corresponding to the minimum phase, and the quality factor is extracted by Lorentzian fit. Fifty resonant elements are measured. The results show that resonant frequency is in the range of 13.6±0.1 MHz and the quality factor achieves 161±12. The quality factor value is smaller than the simulated value of 242. It may be due to extra resistance from the external capacitor. The experimental quality factor is still larger than the reported maximum quality factor of resonant elements, 123. The experimental lumped-element parameters are summarized in Table 2.3.

Table 2.3 Experimental lumped-element parameters of single-layer PSC

| Parameter | Symbol | Value |
|---|---|---|
| Self-inductance (μH) | $L_s$ | 1.36 |
| Parasitic resistance (Ω) | $R_p$ | 0.72 |
| External capacitance (pF) | $C_s$ | 101 |
| Resonant frequency (MHz) | $f_0$ | 13.6±0.1 |
| Quality factor | $Q_0$ | 161±12 |

The coupling factor between two identical elements with a defined axial separation is measured by the method described in [9]. A weak inductive coil is used to read the input impedance of the system. The symmetric and anti-symmetric modes of the two-element system are observed with two resonances. The corresponding frequencies are frequency $f_1$= $1/(2\pi\sqrt{(C(L+M))})$ for a symmetric mode and $f_2$= $1/(2\pi\sqrt{(C(L-M))})$ for an anti-symmetric mode, where $L$, $C$, and $M$ are self-inductance, capacitance of PSCs, and mutual inductance between them respectively. Then the coupling factor can be calculated by

$$\kappa = M/L = \left(f_0/f_1\right)^2 - 1 = 1 - \left(f_0/f_2\right)^2 \tag{2.12}$$

where $f_0$ is the resonant frequency of PSCs.

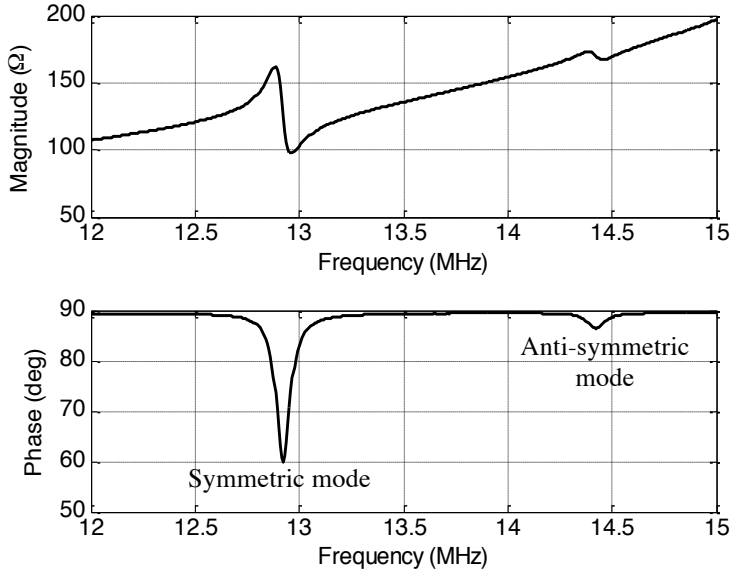


Figure 2.13 Measured input impedance of two coaxial PSCs

Figure 2.13 is the measured input impedance of two coaxial PSCs separated by 2.7 cm, $f_1$ and $f_2$ are frequency points when two phase dips take place, and $\kappa$ is obtained at about 0.1. Then the input impedances with different axial spacing are measured, and the corresponding coupling factors are summarized in Figure 2.14. The dots are experimental results, and the black curve represents simulated results with the use of a partial mutual inductance method. They match each other well.

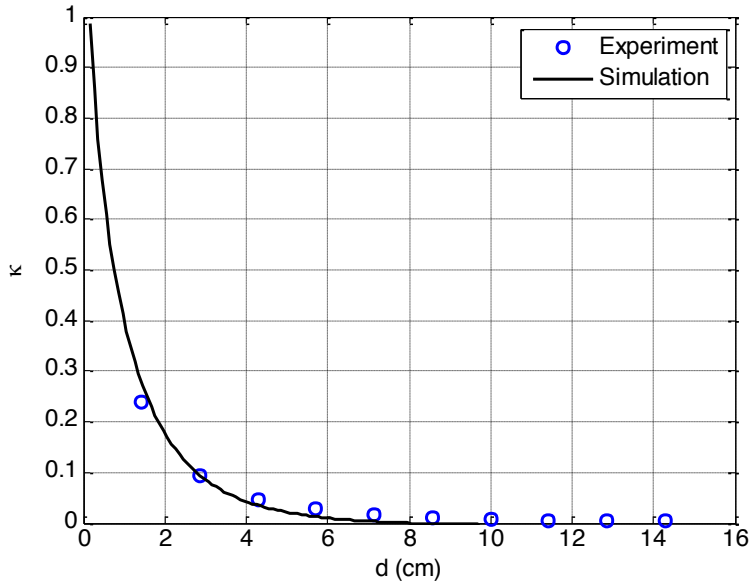


Figure 2.14 Measured coupling factor vs. Axial spacing

## 2.3 One-Dimensional Magneto-inductive Waveguide

A one-dimensional MI waveguide is constructed by a line of equally spaced inductively coupled resonators. In this section, we review the theoretical background of MI waves and investigate MI waves that can be supported by waveguides with PSCs designed in Section 2.2.

### 2.3.1 Circuit Model

Consider an inductively coupled resonator array in Figure 2.15, the square-shaped PSC coils are spaced uniformly by distance $d$, and the coil plane is perpendicular to the line connecting the centers of the loops.

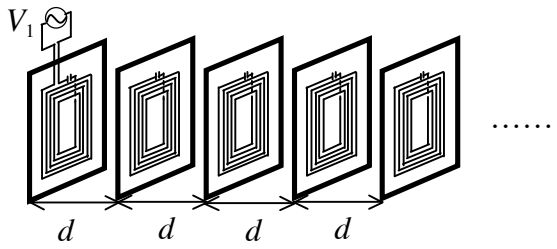


Figure 2.15 Schematic diagram of inductively coupled resonators

MI waves are excited by a voltage source at the first element. The current in the first loop induces a current in the adjacent coil by a magnetically linked flux, which induces further a current in the same principle. This results in MI waves propagating along the resonators.

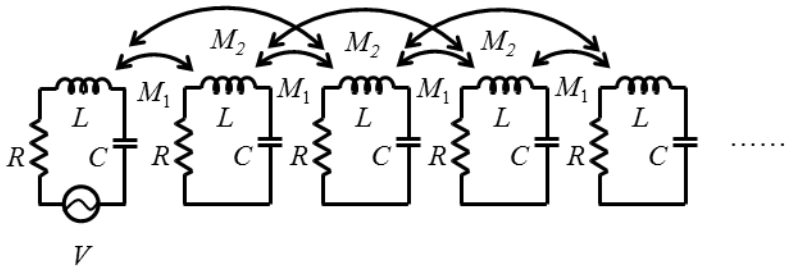


Figure 2.16 Lumped-element circuit model of inductively coupled resonators

Since the dimensions of the waveguide are small relative to the free space wavelength, the MI waveguide can be modeled as a line of inductively coupled resonant lumped-element circuit, as shown in Figure 2.16, where $R$, $L$, and $C$ are self-impedance, self-inductance, and capacitance of resonators, and $M_s$ is the mutual inductance between $i$th element and ($i$+$s$)th element. The current in Coil $n$ will induce a voltage $j\omega M_s I_n$ in Coil $n$+$s$. With analysis in Section 2.2, the self-impedance $Z_n$ (n=1,2,3…$N$) for PSC is,

$$Z_n = R + j\left(\omega L - \frac{1}{\omega C}\right) \tag{2.13}$$

where $\omega$ is the angular frequency, $R = R_s + R_p$, $L = L_s$, and $C = C_s + C_p$. If we define $I_n$ and $V_n$ as current and voltage in $n^{\text{th}}$ resonator, $V_n$ is zero elsewhere except at driver coil, then $I_n$ and $V_n$ satisfy Kirchhoff's voltage law,

$$V_n = Z_n I_n + \sum_{n \neq m} j\omega M_{|m-n|} I_m \tag{2.14}$$

(2.14) can be also written in Matrix form $\boldsymbol{V} = \boldsymbol{ZI}$ for an $N$-element terminated MI waveguide as follows:

$$\begin{bmatrix} V_1 \\ 0 \\ 0 \\ \vdots \\ 0 \\ 0 \\ 0 \end{bmatrix} = \begin{bmatrix} Z_1 & j\omega M_1 & \cdots & j\omega M_S & 0 & \cdots & 0 \\ j\omega M_1 & Z_2 & j\omega M_1 & \cdots & j\omega M_S & 0 & 0 \\ \cdots & j\omega M_1 & Z_3 & j\omega M_1 & \cdots & j\omega M_S & 0 \\ \vdots & \ddots & \ddots & \ddots & \ddots & \ddots & \vdots \\ 0 & j\omega M_S & \cdots & j\omega M_1 & Z_{N-2} & j\omega M_1 & \cdots \\ 0 & 0 & j\omega M_S & \cdots & j\omega M_1 & Z_{N-1} & j\omega M_1 \\ 0 & \cdots & 0 & j\omega M_S & \cdots & j\omega M_1 & Z_N \end{bmatrix} \begin{bmatrix} I_1 \\ I_2 \\ I_3 \\ \vdots \\ I_{N-2} \\ I_{N-1} \\ I_N \end{bmatrix} \tag{2.15}$$

where voltage $\boldsymbol{V}$ and current $\boldsymbol{I}$ are $N \times 1$ vectors, and the impedance matrix $\boldsymbol{Z}$ is a $N \times N$ symmetrical matrix. The main diagonal elements of the impedance matrix are self-impedance of the $n$th ($n$=1,2…$N$) element. The off-diagonal expression $j\omega M_s$ is the mutual impedance induced by another inductor. From the matrix form, we can see that if parameters ($R$, $L$, $C$, $V_1$, and $M_s$) of each passive wireless sensors are given, the current distribution for a given frequency along the array can be solved as product of the inverse impedance matrix and voltage.

### 2.3.2 Dispersion Relationship

The properties of guided MI waves are characterized by the dispersion relationship. The dispersion relationship of MI waves is calculated by considering the traveling wave solution $I_n=\Gamma_1\exp(-(n-1)kd)$ for (2.14), where $k$ is the complex propagation constant $\alpha+j\beta$, and the dispersion relationship can be obtained after manipulation [2],

$$\frac{\omega_0^2}{\omega^2} - 1 + \frac{j}{Q} = \sum_{s=1}^{S} 2\kappa_s \cosh(skd) \tag{2.16}$$

where $\omega_0=1/(2\pi\sqrt{(LC)})$, $Q=\omega L/R$, $\kappa_s=M_s/L$ and $S$ is the maximum value of $s$, which means the magnetic coupling from all elements within the distance of $Sd$ will be considered. The theoretical dispersion characteristic contains three free parameters: the resonant frequency $\omega_0$, the quality factor $Q$, and the coupling constant. Of the three, the resonant frequency $\omega_0$ and the quality factor

$Q$ relate to an individual element only. The coupling constant also depends on the relative position between the two elements.

To present the characteristics of a dispersion relationship, we consider an MI waveguide consisting of an array of PSC designed in Section 2.2. The elements are coaxially spaced by a center-to-center distance $d$ of 2.7 cm. The circuit parameters $R$, $L$, and $C$ are 0.72Ω, 1.36μH, and 101 pF respectively. The measured coupling factor between two coaxial coils within distance of $3d$ are $\kappa_1$=0.094, $\kappa_2$=0.028, and $\kappa_3$=0.01. Then the dispersion relationship for the coaxial array with $S$=1 and $S$=3 are presented in Figure 2.17.

.

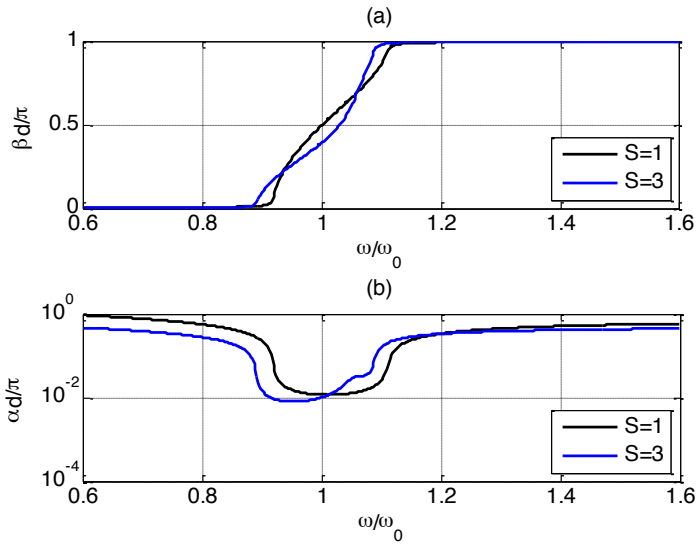


Figure 2.17 Dispersion relationship for MI waveguide with $d$=2.7 cm: (a) Phase constant (b) Attenuation constant

The x-axis is normalized to the resonant angular frequency of element in Figure 2.17. The upper and lower plots are the phase constant and the attenuation constant, respectively. The phase constant shows that MI waves are dispersive waves. The attenuation constant curve demonstrates that MI waves can only propagate within a bandwidth around the resonant frequency. The structure supports the waves in range from $\omega/\omega_0$=0.91 to $\omega/\omega_0$=1.11, with a

bandwidth of 2.71 MHz by the black curve ($S$=1). And the minimum attenuation happens at $\omega/\omega_0$=1.07 when $\alpha d/\pi$=0.013. From the blue curve ($S$=3), the passband is found between $\omega/\omega_0$=0.89 and $\omega/\omega_0$=1.09 with the same bandwidth. The lowest value of the attenuation occurs at $\omega/\omega_0$=0.95, giving $\alpha d/\pi$=0.0081. In the frequency range outside the passband, the evanescent waves will decay quickly.

If the coupling factor with the farther neighbor is small enough, the nearest neighbor interaction would give a sufficiently accurate description and present the salient features. Let us explore the rough relationship between the propagation constant and the frequency by only taking the nearest interaction ($S$=1). If we replace $k$ with attenuation constant $\alpha$ and phase constant $\beta$, then the equation in (2.16) with only the coupling factor $\kappa_1$ can be simplified as

$$\frac{\omega_0^2}{\omega^2} - 1 = 2\kappa_1 \cos(\beta d)\frac{\exp(\alpha d) + \exp(-\alpha d)}{2} \tag{2.17}$$

$$\frac{j}{Q} = 2j\kappa_1 \sin(\beta d)\frac{\exp(\alpha d) - \exp(-\alpha d)}{2} \tag{2.18}$$

The product of attenuation coefficient $\alpha$ and distance $d$ is very small within the passband, so $\exp(\pm\alpha d)$ can be approximated as $1\pm\alpha d$. Then (2.18) and (2.19) are simplified as

$$\frac{\omega_0^2}{\omega^2} - 1 = 2\kappa_1 \cos(\beta d) \tag{2.19}$$

$$\frac{j}{Q} = 2j\kappa_1 \sin(\beta d)\alpha d \tag{2.20}$$

(2.19) shows that MI waves can only propagate over the frequency range $1/(1+2\kappa_1) \le (\omega/\omega_0)^2 \le 1/(1-2\kappa_1)$. The lower frequency edge corresponds to $\beta d$=0, while the high frequency edge is reached at $\beta d=\pi$. The higher coupling factor $\kappa_1$ contributes to a wider passband. For a frequency less than lower edge $(\omega/\omega_0)^2 = 1/(1+2\kappa_1)$, the currents in all elements are in phase

because $\beta d$=0, while currents in neighboring elements are always in antiphase due to $\beta d$=$\pi$ in the higher stopband.

(2.20) shows that the attenuation coefficient $\alpha d$ gets a minimum value of $1/(2\kappa_1 Q_0)$ with $\beta d = \pi/2$ at mid-band. Therefore, elements with a high quality factor and a strong coupling coefficient should be adopted to achieve low propagation loss and wider passband. For the same coaxial PSC array, stronger coupling can be achieved by reducing the distance between the elements. If the axial spacing is reduced to 1.4 cm, the dispersion relationship with the coupling factors $\kappa_1 = 0.24$, $\kappa_2 = 0.094$, and $\kappa_3 = 0.045$ is shown as,

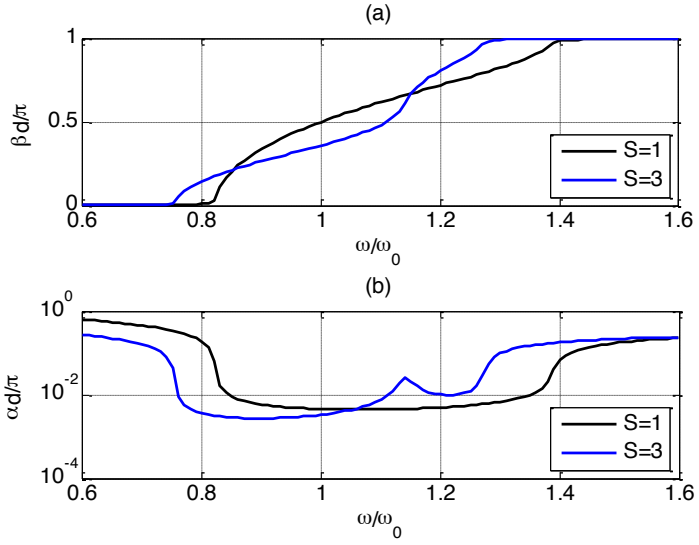


Figure 2.18 Dispersion relationship for MI waveguide with $d$=1.4 cm: (a) Phase constant (b) Attenuation constant

The dispersion curves in Figure 2.18 are quite similar. There are frequencies for which propagation is possible ($0.82 \le \omega/\omega_0 \le 1.39$ with $S$=1; $0.75 \le \omega/\omega_0 \le 1.28$ with $S$=3) and other frequencies outside this band for which propagation is stopped. The resulting frequency passband is around 7.19 MHz, which is much wider than a bandwidth of 2.71 MHz with $d$=2.7 cm with. And this waveguide holds the minimum attenuation of $\alpha d/\pi$=0.0045 at $\omega/\omega_0$=1.05

($S$=1), and $\alpha d/\pi$=0.0029 at $\omega/\omega_0$=0.9 ($S$=3). It is almost one-fourth the value of $d$=2.7 cm. Comparing the dispersion relationship for the two MI waveguides with different axial spacing, we can see that a smaller gap improves both propagation loss and passband width, so smaller values of attenuation are possible by reducing the distance between the resonant elements.

### 2.3.3 Group Velocity

MI waves are dispersive waves from the dispersion relationship. The wave shapes are distorted when propogated along a waveguide. We are interested about the group velocity that is the speed of the wave packet because the wave travel distance can be estimated by multiplying time of flight and group velocity. For a wave characterized by dispersion relationship (2.16), the group velocity $v_g$ can be derived by the derivative of angular frequency to wavenumber and expressed as

$$v_g = \frac{\omega^3}{\omega_0^2} \sum_{s=1}^{S} js\kappa_s d \sinh(skd) \tag{2.21}$$

Substitute $k$ with $\alpha + j\beta$ into (2.21),

$$v_g = \frac{\omega^3}{\omega_0^2} \sum_{s=1}^{S} js\kappa_s d \frac{\exp(s\alpha d)(\cos(s\beta d) + j\sin(s\beta d)) - \exp(-s\alpha d)(\cos(s\beta d) - j\sin(s\beta d))}{2} \tag{2.22}$$

If only the nearest interaction is taken in account, the frequency-dependent group velocity can be simplified as (2.23) with negligible attenuation within the passband as follows:

$$v_g = \frac{\omega^3}{\omega_0^2} \kappa_1 d \sin(\beta d) \tag{2.23}$$

where $\sin(\beta d)$ is always greater than zero within the passband because of $0<\beta d<\pi$. The direction of group velocity is decided by the sign of coupling factor $\kappa_1$ and the value is proportional to the absolute value of the coupling factor. When the coupling factor is negative, the MI waves are

backward waves. The wave packet travels fast when the coupling is strong. For the two MI waveguides characterized by Figure 2.17 and Figure 2.18, the group velocity as a function of frequency is plotted as

(a)

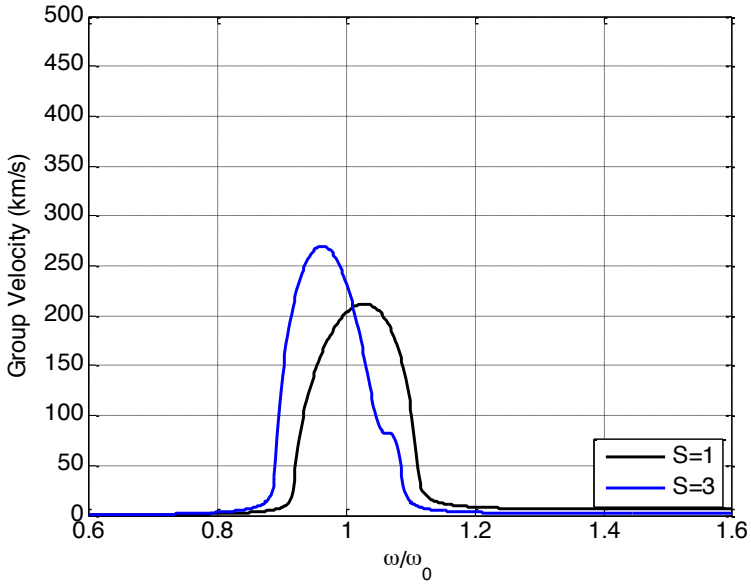


(b)

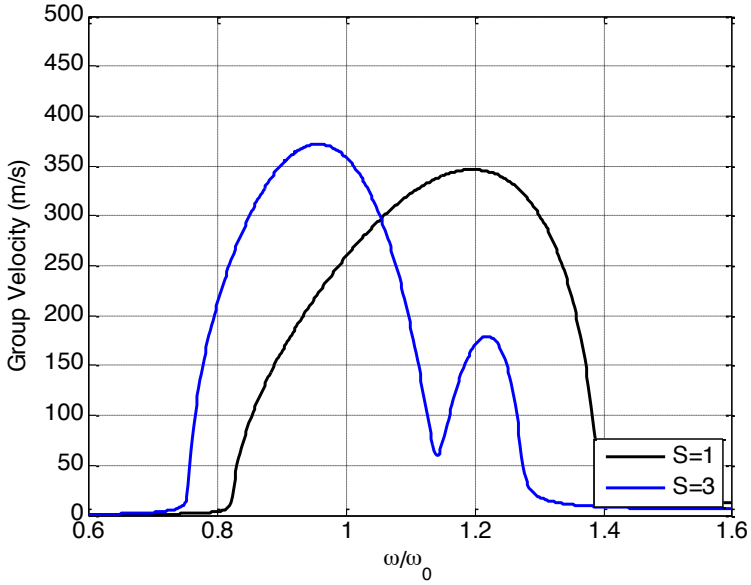


Figure 2.19 Group velocity vs. Normalized frequency: (a) $d$=2.7 cm (b) $d$=1.4 cm

Figure 2.19 presents the group velocity of MI waves supported by the coupled PSCs with $d$=2.7 cm and $d$=1.4 cm. During the passband, the wave envelope does not move at a single velocity, and stronger coupling due to a narrower gap makes high group velocity. It is observed in Figure 2.19(a) that the maximum group velocity for an MI waveguide with $d$=2.7 cm is 212 km/s at $\omega/\omega_0$=1.03 ($S$=1) and 270 km/s at $\omega/\omega_0$=0.96 ($S$=3), respectively. Figure 2.19(b) shows the group velocity variation with $d$=1.4 *cm*. The maximum group velocity goes up to 346 km/s at $\omega/\omega_0$=1.2 ($S$=1) and 372 km/s at $\omega/\omega_0$=0.96 ($S$=3).

### 2.3.4 Characteristic Impedance and Insertion Loss

According to the transmission line theory, reflections will be introduced unless the transmission line is terminated by its characteristic impedance $Z_t$. For an $N$-element resonator array, the current and voltage in the last element obey the following relation with (2.14):

$$Z_N I_N + j\omega M_1 \left(I_{N-1} + I_{N+1}\right) + j\omega M_2 \left(I_{N-2} + I_{N+2}\right) + \ldots + j\omega M_S \left(I_{N-S} + I_{N+S}\right) = 0 \qquad (2.24)$$

However, the current $I_{N+s}$ ($s$=1,2,…$S$) does not exist, so the traveling wave $I_n=I_0\exp(-nkd)$ is not the solution for (2.23). The current assumed in the form of a traveling wave may still be satisfied if we include characteristic impedance $Z_t$ in the last element, then we have

$$\left(Z_N + Z_t\right) I_N + j\omega M_1 I_{N-1} + j\omega M_2 I_{N-2} + \ldots + j\omega M_S I_{N-S} = 0 \qquad (2.25)$$

where the characteristic impedance $Z_t$ equals

$$Z_t = j\omega M_1 \exp\left(-kd\right) + j\omega M_2 \exp\left(-2kd\right) + \ldots + j\omega M_S \exp\left(-Skd\right) \qquad (2.26)$$

where the characteristic impedance $Z_t$ is a function of angular frequency, mutual inductance, and propagation constant $k$. Specific value of terminal impedance will only match the transmission line at one frequency while still introduce reflections at other frequencies. If we only take the

nearest interaction into consideration, $Z_t$ equals one item $j\omega M_1 \exp(-kd)$. We can plot the matched impedance variance with frequency as

(a)

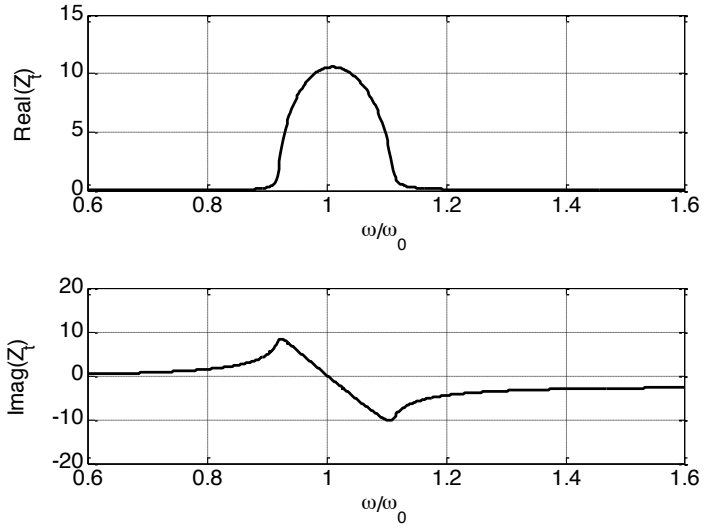


(b)

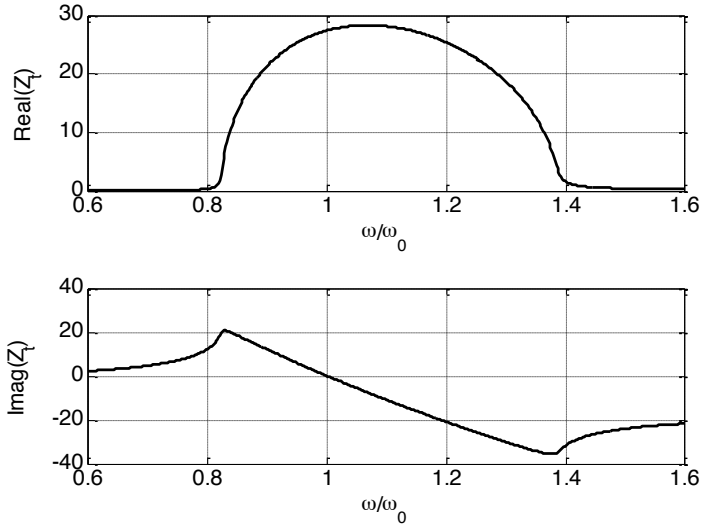


Figure 2.20 Characteristics impedance vs. Frequency: (a) $d$=2.7 cm (b) $d$=1.4 cm

Figure 2.20 shows the real and imaginary parts of charateristic impedance $Z_t$ of an MI waveguide with $d$=2.7 *cm* and $d$=1.4 *cm*, respectively. At resonant frequency, the propagation coefficient $\beta d$ equals $\pi/2$, and $Z_t$ is purely resistive $\omega_0 M_1$. The value is 10.9 Ω and 27.8 Ω for an MI waveguide with $d$=2.7 *cm* and $d$=1.4 *cm*, respectively. Since the resistive impedance is most feasible and is the matched impedance at resonant frequency, we use it as the load at the last element to minimize end reflections.

Insertion loss is another measure of attenuation during the passband and defined as the loss of signal power resulting from the insertion of device. If the transmitted power is $P_i$ and the power received by the load is $P_o$, the insertion loss in dB is defined by

$$\text{Loss} = 10\log_{10}\left(\frac{P_o}{P_i}\right) \tag{2.27}$$

If the MI waveguide is driven by voltage $V_1$ in the first coil, then power is transmitted along the $N$-element waveguide through the magnetic coupling between elements. The input power at the first element and output power delivered to the matched load $Z_t$ can be expressed as

$$P_i = 1/2\,\text{Re}\left(I_1 V_1^*\right) \tag{2.28}$$

$$P_0 = 1/2\left|I_N\right|^2 \text{Re}\left(Z_t\right) \tag{2.29}$$

Substitute input and output power expression (2.28) and (2.29) into (2.27), we obtain the insertion loss as

$$\text{Loss} = 10\log_{10}\left(\frac{\left|I_N\right|^2 \text{Re}\left(Z_t\right)}{\text{Re}\left(I_1 V_1^*\right)}\right) \tag{2.30}$$

Consider a $N$-element MI waveguide terminated with its characteristic impedance $Z_t$ and supporting a traveling wave $I_n$=$I_1$ exp(-($n$-1)$kd$), it yields the following expression with $I_N$=$I_1$ exp(-($N$-1)$kd$) and $V_1$=$I_1$ ($Z_0$+$Z_t$):

$$\text{Loss} = 10\log_{10}\left(\frac{\exp\left(-2(N-1)\alpha d\right)\text{Re}\left(Z_t\right)}{\text{Re}\left(Z_0+Z_t\right)}\right)$$
$$= -8.69(N-1)\alpha d + C \tag{2.31}$$

where $C$ equals $10\log_{10}(\text{Re}(Z_t))$-$10\log_{10}(\text{Re}(Z_0+Z_t))$ that depends only on $Z_0$ and $Z_t$. After the single resonator is designed and matched impedance is selected, the insertion loss in dB rises linearly with the number of resonators $N$ by (2.30), and loss per element in dB is -8.69$\alpha d$. If we extract the value $\alpha d$ from dispersion relationship curves ($S$=3) in Figure 2.17 and Figure 2.18, then the minimum loss per tag for waveguide with $d$ = 2.7 cm and $d$ = 1.4 cm are 0.27 dB and 0.096 dB, respectively.

Given the parameters ($R$, $L$, and $C$) of a coaxial $N$-element MI waveguide listed in Table 2.3, the dominant mutual inductance $M_1$ is 0.13μH and 0.33μH for one-dimensional MI waveguides with $d$ = 2.7 cm and 1.4 cm. Then the insertion loss curves are plotted as

(a)

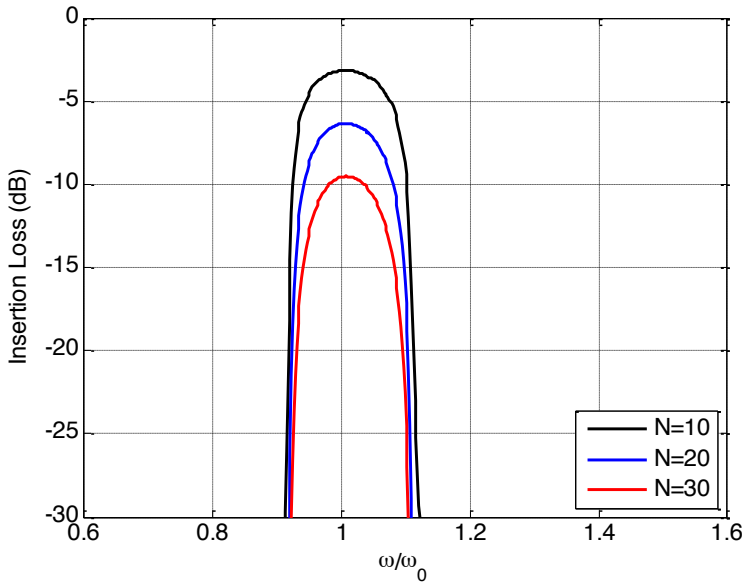

(b)

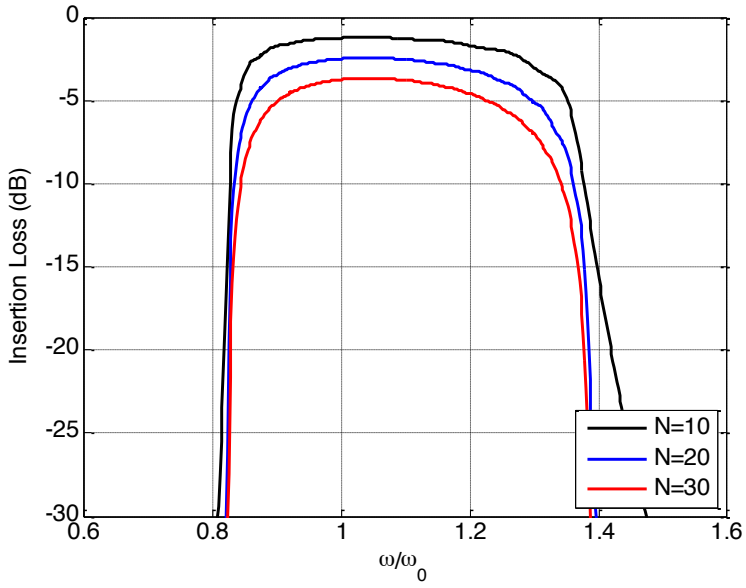


Figure 2.21 Insertion loss vs. Frequency: (a) $d$=2.7 cm (b) $d$=1.4 cm

Figure 2.21 (a) presents the frequency characteristics of a coaxial resonator array with $d$=2.7 cm, the number of elements is chosen 10, 20, and 30, respectively. The corresponding matched impedance is 10.9 Ω. The frequency characteristics show passive wireless sensor array as the MI waveguide act as a bandpass filter. MI waves can travel along the waveguide over the normalized frequency range ($0.91<\omega/\omega_0<1.11$) that agrees with the bandwidth by dispersion relationship. As the passive wireless sensor array contains more elements, the minimum insertion losses increase linearly at each frequency point, while the passband width remains the same.

The same simulation is repeated with $d$ = 1.4 cm and $Z_t$ =27.8 Ω. The results are shown in Figure 2.21(b). Since the coils with narrower gap have stronger magnetic coupling, the insertion loss over the passband are less and the bandwidth is wider. MI waves can propagate along the MI waveguide within the normalized frequency range ($0.82\leq\omega/\omega_0\leq1.39$).

### 2.3.5 Tolerance

If the aim is to produce a traveling wave of the form $I_n=I_0\exp(-nkd)$, it can only be done if the power traveling in the wave is dissipated without any reflections. An MI waveguide that consists of a periodic array of resonators needs to be terminated with its characteristic impedance. But what will happen if there are manufacturing tolerances? Transmission will clearly be affected since the circuit parameters would vary around its nominal value.

Manufacturing tolerance is the extent to which the actual capacitance changes from its nominal value and can be expressed as a plus-or-minus value (±) or as a percentage (±%). Here we use percentage $\delta$ to indicate the tolerance, where $\delta$ is positive. Then an $L\pm\delta_L$ tolerance inductor may have a maximum value of $L(1+\delta_L)$ and a minimum value of $L(1-\delta_L)$, where $L$ is the nominal inductance value and $\delta_L$ is the inductance tolerance percentage. We assume the inductance is subject to the truncated normal distribution with mean $\mu$ and standard deviation $\sigma$. The mean $\mu$ and standard deviation $\sigma$ for $L\pm\delta_L$ tolerance inductors are considered as $L$ and $L\delta_L/3$ respectively. The inductance value always lies within the range from $L(1-\delta_L)$ to $L(1+\delta_L)$.

The power transmission characteristics are investigated over a range of frequencies when inductor, capacitor, and resistor are subject to this statistics model respectively. The value will be normalized with the output power when each tolerance is zero.

Consider a 20-element MI waveguide using resonant PSCs in Section 2.2: it is driven by a voltage $V_1$ applied to the first element and terminated with the simplified waveguide characteristic impedance $Z_t= \omega_0 M_1$ at resonant frequency. With the same set of circuit parameters as shown in Table 2.3, the capacitance and resistance are fixed at 101 pF and 0.72 Ω. The nominal inductance value is $L$=1.36 μH. The inductance value in each resonator is generated

following the truncated normal distribution $N$ ($L$, $(L\delta_L/3)^2$) and all numbers are guaranteed positive.

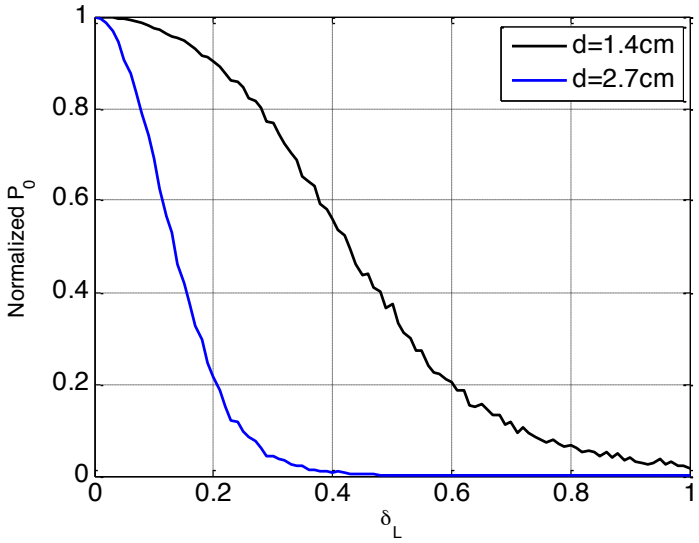


Figure 2.22 Normalized transmitted power vs. Inductor tolerance for MI waveguide with different axial spacing

At resonant frequency ($ka = \pi/2$), the normalized output power in linear scale with increasing $\delta_L$ are shown in Figure 2.22. The power reaching the load is calculated with the three nearest neighbor interactions ($S$=3) and normalized to the transmitted power when resonator circuit parameters in each element are identical. For every tolerance point, the normalized power is the average of 1,000 calculations. The black curve and blue curve are for MI waveguides with axial spacing of 1.4 cm and 2.7 cm, respectively. It shows that an MI waveguide with narrower gap has more manufacturing tolerance and the decline is more moderate. For $\delta_L$ = 5%, the normalized power reaching the load is still 99.5% in contrast to 91.5% with gap doubled.

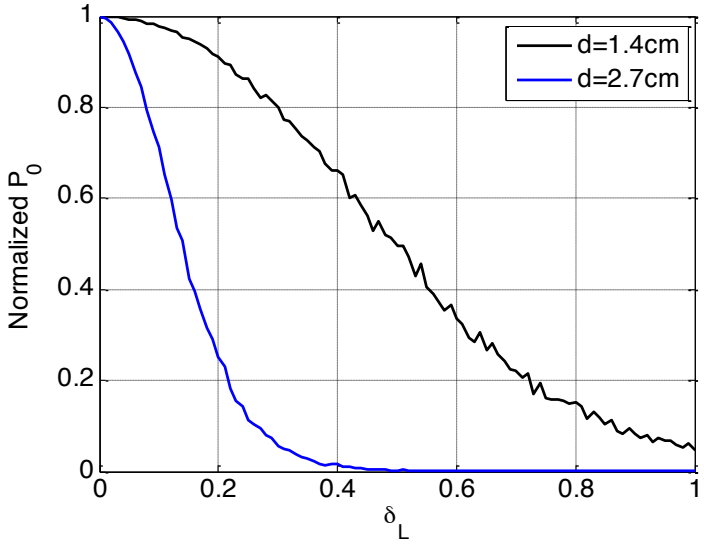


Figure 2.23 Normalized transmitted power vs. Capacitor tolerance for MI waveguide with different axial spacing

The same scenario is observed when capacitances along the line vary in the same manner. The capacitance for each element is generated by the truncated normal distribution with a mean of 101 pF and a standard deviation $33.67\delta_C$ pF. The tolerance percentage $\delta_C$ goes from 0 to 1. The results are presented in Figure 2.23. When $\delta_C$ equals 5%, the transmitted power drops to 99.4% with $d$=1.4 cm and 91.5% with $d$=2.7 cm of the value when capacitance are unchanged.

We repeat the same calculation with resistor manufacturing tolerance. It shows that the transmitted power is almost unaffected by resistance variance when $\delta_R \leq 1$. This is because resistance is small compared to the magnitude of self-impedance.

The delivered power to load by one-dimensional MI waveguides is also compared with different lengths. Figure 2.24 shows the results with inductance tolerance variances for both 20-element and 40-element MI waveguide constructed by the same resonators with $d$=1.4 cm. The normalized transmitted power decreases from 99.4% to 98.6% when 40 coupled elements work along the line. The calculated results with capacitances subject to the truncated normal

distribution also show the similar phenomenon, and the transmitted power percentage goes down 99.5% from 98.6%. The shorter MI waveguide is more robust to the circuit parameter variances.

In the actual design, the effect of tolerances cannot be overlooked. We need to adopt circuit components with the least amount of tolerance as possible. Then the individual elements should be placed with narrower gap between them to maximize power delivered to the load.

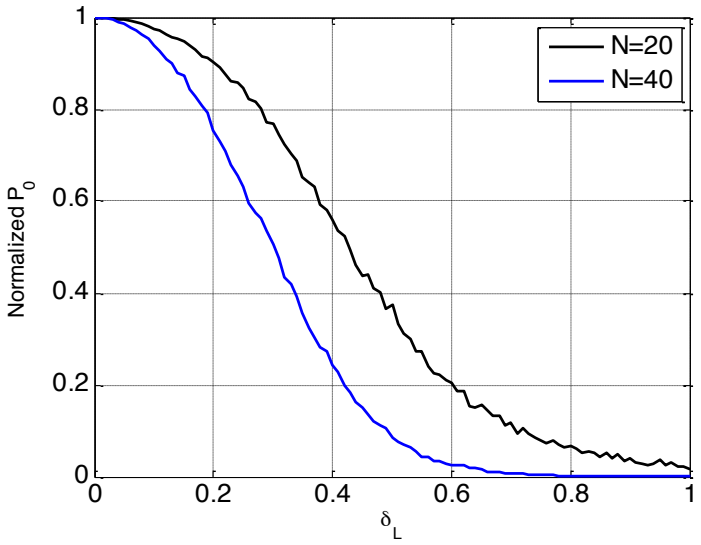


Figure 2.24 Normalized transmitted power vs. Inductor tolerance for MI waveguide with different number of elements ($d$=1.4 cm)

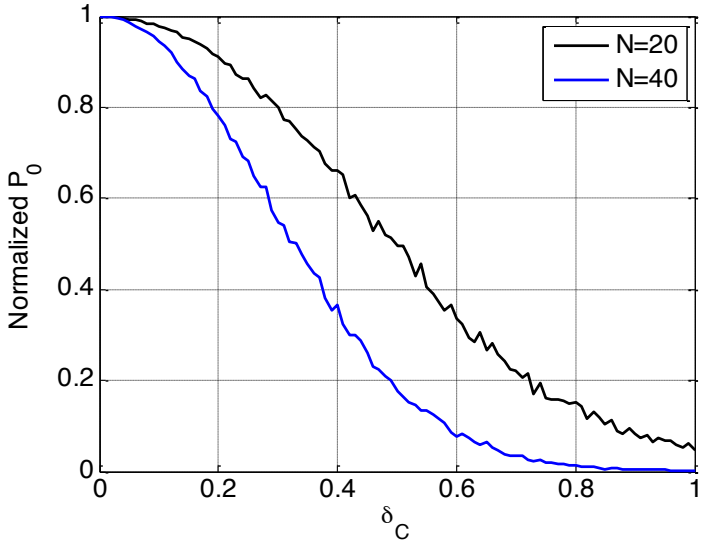


Figure 2.25 Normalized transmitted power vs. Capacitor tolerance for MI waveguide with different number of elements ($d$=1.4 cm)

## 2.4 SUMMARY

The chapter described the development of the low-loss magneto-inductive waveguide constructed by a line of inductively coupled PSCs. First, high-Q PSCs were designed to work at 13.56 MHz; then one-dimensional MI waveguides constructed by the PSC array were studied; the dispersion relationship showed passband behaviors, and the group velocity of the supported MI waves showed they were set of slow waves; high-Q factor and strong magnetic coupling would contribute to a lower attenuation constant and a wider passband frequency range. Finally, the statistics about the effect of geometry on MI waves were discussed. The circuit components with high tolerance decreased power delivered along the waveguide.

# Chapter 3 Low-Loss Magneto-Inductive Waveguide for Sensing Applications

## 3.1 INTRODUCTION

MI waveguide performs as a passband filter within a band of frequencies. The dispersion relationship has been studied in the previous chapter. Many applications have been proposed, including delay lines, phase shifters, couplers and splitters, concentrators, near-field lenses, detectors for magnetic resonance imaging, safe interconnects of internal MRI, data transfer channels, and underground wireless networks.

This chapter focuses attention on the sensing application of the MI waveguide. The self-impedance or mutual impedance discontinuity is introduced along the line of inductively coupled resonators when a specific transducer incorporates with resonant elements. The discontinuities are referred to as defects in this chapter. The investigation begins by studying the transmission and reflection coefficients for the MI waveguide with one defect. MI waves in the time domain is simulated with a circuit model implemented in PSpice. Then we will illustrate how distributed defects in the resonator array affect wave propagations. The corresponding sensing mechanism is developed by processing the reflected MI waves.

## 3.2 LOW-LOSS MI WAVEGUIDE WITH ONE DEFECT

When designing the passive wireless corrosion sensor [36–38], we connected an exposed wire in the resonant sensor circuit as resistive transducer to detect rebar corrosion. The principle involved in the transducer is that the sensor, embedded in the same corrosive environment as the reinforcing steel, and exposed wire resistance would increase as the wire corroded. Since the corrosion process begins in the wire and the cross-sectional areas are reduced, the resistance of

the sensor circuit increases and causes a reduction in the phase dip depth at sensor resonant frequency. This kind of sensor is embedded in concrete and interrogated by an external reader to determine if a corrosion threshold has been reached.

This resistive transducers can also be incorporated with the resonant element used to construct the MI waveguide. When corrosion happens, the resonant element self-impedance could be changed due to the transducer. In this section, we discuss the feasibility of monitoring the change by analyzing MI waves instead of reading input impedance. One obvious advantage is the read range would be larger using the waveguide instead of the single sensor.

### 3.2.1 Circuit Model

The impedance discontinuity in a MI waveguide could be caused by variances of circuit parameters, for example, self-impedance or mutual impedance variance.

In the self-impedance case, one element is assumed to have a self-impedance change $\Delta Z$, which could be introduced by an attached transducer, as shown in Figure 3.1.

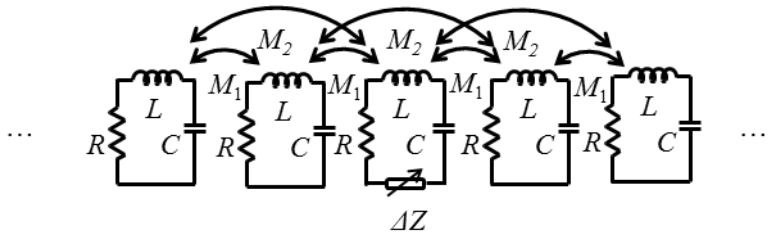


Figure 3.1 Circuit model of MI waveguide with self-impedance defect

where $\Delta Z$ could be resistive, inductive, or capacitive. An element along an MI waveguide attaching the resistive transducer will have extra resistance due to the onset of corrosion. The coupling between the defective element and other elements are supposed to be unchanged. For the $N$-element terminated resonator array with $n$th defect, the matrix form of Kirchhoff Circuit Laws becomes

$$\begin{bmatrix} Z_1 & j\omega M_1 & \cdots & j\omega M_S & & & & \\ j\omega M_1 & Z_2 & j\omega M_1 & \cdots & & & & \\ \cdots & \ddots & \ddots & \ddots & \cdots & & & \\ & \cdots & j\omega M_1 & Z_n' & j\omega M_1 & \cdots & & \\ & & \cdots & \ddots & \ddots & \ddots & \cdots & \\ & & & \cdots & j\omega M_1 & Z_{N-1} & j\omega M_1 & \\ & & & j\omega M_S & \cdots & j\omega M_1 & Z_N + Z_t & \end{bmatrix} \begin{bmatrix} I_1 \\ I_2 \\ \vdots \\ I_n \\ \vdots \\ I_{N-1} \\ I_N \end{bmatrix} = \begin{bmatrix} V_1 \\ 0 \\ \vdots \\ 0 \\ \vdots \\ 0 \\ 0 \end{bmatrix} \tag{3.1}$$

where $Z_n' = R+j\omega L+1/(j\omega C)+\Delta Z$, impedance $\boldsymbol{Z}$ is a $N \times N$ matrix with a different self-impedance at the $n$th element. Then the pure traveling waves no longer suffice as the solution, and reflected waves take place due to the discontinuity. Details are provided in next section.

A mutual inductance variation is introduced by increasing or decreasing the separation between two adjacent elements, as shown in Figure 3.2, where $M'$ is the mutual inductance at the point of discontinuity. The mutual inductance could happen when the relative position between two elements changes or some elements are decoupled with the waveguide. For example, if the attached exposed wire of an element along an MI waveguide is broken by corrosion, leaving the resonant circuit open, then the element is decoupled from its neighbors. The energy is transmitted from its left-side neighbor to its right-side neighbor directly through a different mutual coupling.

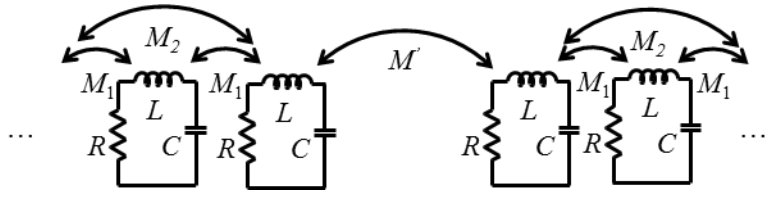


Figure 3.2 Circuit model of MI waveguide with mutual impedance defect

We have the current and voltage relation as follows with the lumped-element circuit model shown in Figure 3.2.

$$\begin{bmatrix} Z_1 & j\omega M_1 & \cdots & j\omega M_S & & & & & \\ j\omega M_1 & Z_2 & j\omega M_1 & \cdots & & & & & \\ \cdots & \ddots & \ddots & \ddots & \cdots & & & & \\ \cdots & j\omega M_2 & j\omega M_1 & Z_{n-1} & j\omega M' & \cdots & & & \\ & & \cdots & j\omega M' & Z_n & j\omega M_1 & j\omega M_2 & \cdots & \\ & & & \cdots & \ddots & \ddots & \ddots & \cdots & \\ & & & & \cdots & j\omega M_1 & Z_{N-1} & j\omega M_1 & \\ & & & & j\omega M_S & \cdots & j\omega M_1 & Z_N & \end{bmatrix} \begin{bmatrix} I_1 \\ I_2 \\ \vdots \\ I_{n-1} \\ I_n \\ \vdots \\ I_{N-1} \\ I_N \end{bmatrix} = \begin{bmatrix} V_1 \\ 0 \\ \vdots \\ 0 \\ 0 \\ \vdots \\ 0 \\ 0 \end{bmatrix} \quad (3.2)$$

where the impedance matrix $\boldsymbol{Z}$ is an $N \times N$ matrix, and the corresponding current and voltage for elements are both $N \times 1$ vectors. The off-diagonal mutual impedance between $n$-1th and $n$th are $j\omega M'$. Similarly, the current distribution can be solved by multiplying the inverse of the impedance matrix by the voltage vector.

### 3.2.2 Transmission and Reflection

Figure 3.3 shows that the MI waveguide with element 0 has a transducer for defect detection. This transducer could introduce resistive, inductive, or capacitive impedance change $\Delta Z$ to the resonant circuit. Then self-impedance of the element becomes $R+j\omega L+1/(j\omega C)+\Delta Z$, where $R$, $L$, and $C$ are the nominal resistance, self-inductance, and capacitance of resonant circuit, respectively.

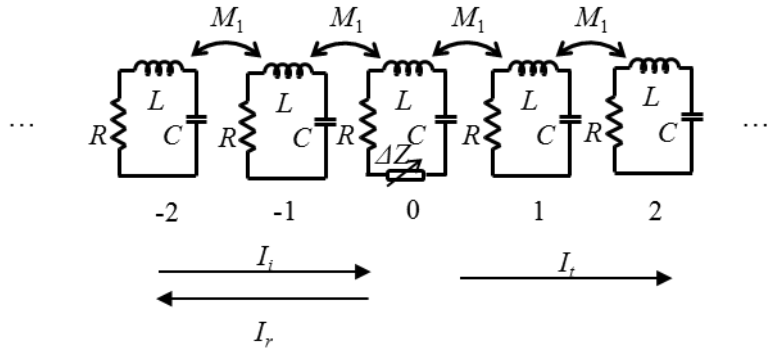


Figure 3.3 Simplified circuit model of MI waveguide with self-impedance defect

In Figure 3.3, only coupling with the nearest neighbor is considered. If $\Delta Z \neq 0$, the backward waves will be generated along the waveguide due to the impedance discontinuity, as shown in Figure 3.3, where $I_i$, $I_r$, and $I_t$ indicate the incident, reflected, and transmitted currents. The incident current $I_i$ is in the traveling wave form $I_n = I\exp(-nkd)$. Then the current in $n$th resonator $I_n$ can be described with the reflection coefficient $\Gamma$ and transmission coefficient $T$ as

$$I_n = \begin{cases} I_i + I_r = I\exp(-nkd) + \Gamma I\exp(nkd) & n \le 0 \\ I_t = TI\exp(-nkd) & n \ge 1 \end{cases} \tag{3.3}$$

The current in the elements before the discontinuity is a combination of incident and reflected current. After the junction, the current is the traveling wave with an amplitude of $TI$. We assume element 0 has the same coupling with its neighbors as do the other elements. The currents and voltages at the junction satisfy the following relation with only the nearest interaction:

$$\begin{aligned} Z^{'}I_0 + X_1 I_1 + X_1 I_{-1} &= 0 \\ ZI_1 + X_1 I_0 + X_1 I_2 &= 0 \end{aligned} \tag{3.4}$$

where self-impedance $Z^{'} = R + j\omega L + 1/(j\omega C) + \Delta Z$, and mutual impedance $X_1 = j\omega M_1$. Substituting (3.3) into (3.4), the following is obtained:

$$\begin{aligned} Z^{'}(1+\Gamma) + j\omega M_1\left(\exp(kd) + \Gamma\exp(-kd) + T\exp(-kd)\right) &= 0 \\ ZT\exp(-kd) + j\omega M_1\left(1 + \Gamma + T\exp(-2kd)\right) &= 0 \end{aligned} \tag{3.5}$$

With the two equations above, the reflection coefficient $\Gamma$ and transmission coefficient $T$ are solved as

$$\Gamma = -\frac{ZZ^{'} + j\omega M_1 Z\exp(kd) + j\omega M_1 Z^{'}\exp(-kd)}{ZZ^{'} + j\omega M_1\exp(-kd)\left(Z + Z^{'}\right) + \left(j\omega M_1\right)^2\left(\exp(-2kd) - 1\right)} \tag{3.6}$$

$$T = -\frac{\left(j\omega M_1\right)^2\left(1 - \exp(2kd)\right)}{ZZ^{'} + j\omega M_1\exp(-kd)\left(Z + Z^{'}\right) + \left(j\omega M_1\right)^2\left(\exp(-2kd) - 1\right)} \tag{3.7}$$

Substituting $Z=-j\omega M_1(\exp(kd)+\exp(-kd))$ into (3.6) and (3.7), then simplifying the expression yields the following:

$$\Gamma = \frac{Z - Z^{'}}{Z^{'} + 2j\omega M_1 \exp(-kd)} \tag{3.8}$$

$$T = \frac{Z + 2j\omega M_1 \exp(-kd)}{Z^{'} + 2j\omega M_1 \exp(-kd)} \tag{3.9}$$

The above equation shows that if $Z \neq Z^{'}$, reflections take place. In addition to self-impedance mismatch, MI wave reflections also relate to the product of wavenumber $k$ and spacing $d$. Consider an MI waveguide formed by coaxially placed PSC with circuit parameters are $R$=0.8 Ω, $L$=1.36 μH, $C$=101 pF, and $M_1$=0.33 μH. We take only the magnetic coupling from the nearest neighbor into consideration:

(a)

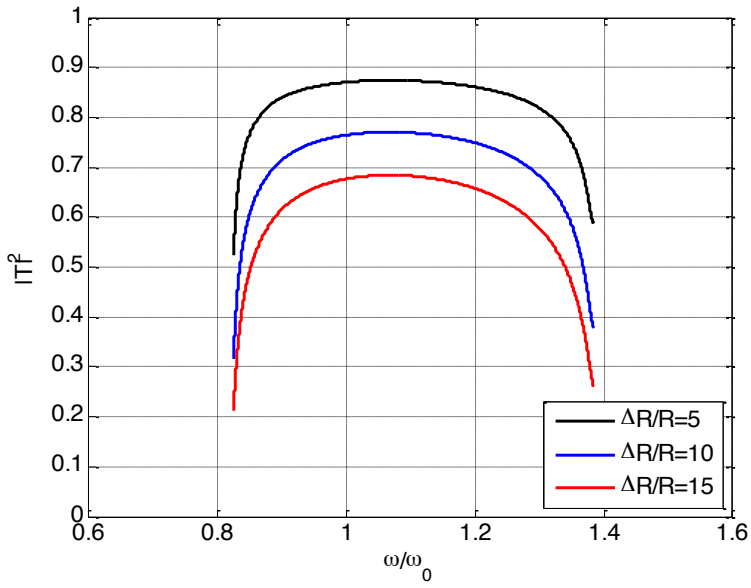


(b)

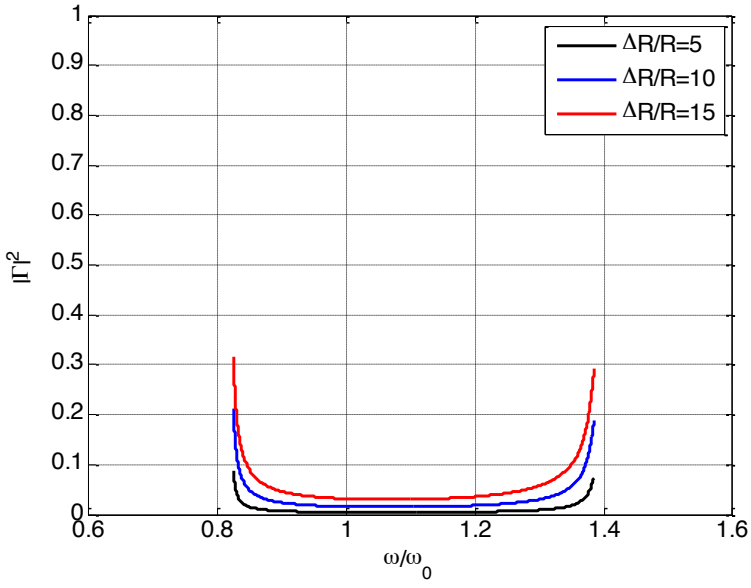


Figure 3.4 Power coefficient vs. Frequency with resistive transducer: (a) Transmission (b) Reflection

Figure 3.4 shows that the power reflection coefficient $|\Gamma|^2$ and transmission coefficient $|T|^2$, with resistive $\Delta Z$ as a function of frequency. The value of $\Delta Z$ is increased to simulate the

process of corrosion. The extra resistance $\Delta R$ is chosen as 4Ω, 8Ω, and 12Ω, respectively. With the analysis in Chapter 2, the traveling waves within the frequency band $0.82 \leq (\omega/\omega_0) \leq 1.39$ can be supported by this inductively coupled PSC array. Figure 3.4 shows that a higher impedance mismatch will introduce stronger reflection within the passband. In each case, $|\Gamma|^2$ gets a minimum value around the resonant frequency that corresponds to the optimum attenuation loss obtained by the dispersion relationship, and increases sharply toward the band edge. Near the resonant frequency, we neglect the propagation loss and may obtain

$$\Gamma \approx \frac{\Delta R}{\Delta R + R + 2\omega_0 M_1} \tag{3.10}$$

$$T \approx \frac{R + 2\omega M_1}{\Delta R + R + 2\omega_0 M_1} \tag{3.11}$$

(3.10) and (3.11) suggest $|\Gamma|^2+|T|^2 \leq 1$ due to the loss, and reflection happens when $\Delta R \neq 0$. Figure 3.5 presents $|\Gamma|^2$ and $|T|^2$ as a function of $\Delta R$. The reflected power increases gradually as the mismatch impedance $\Delta R$ increases.

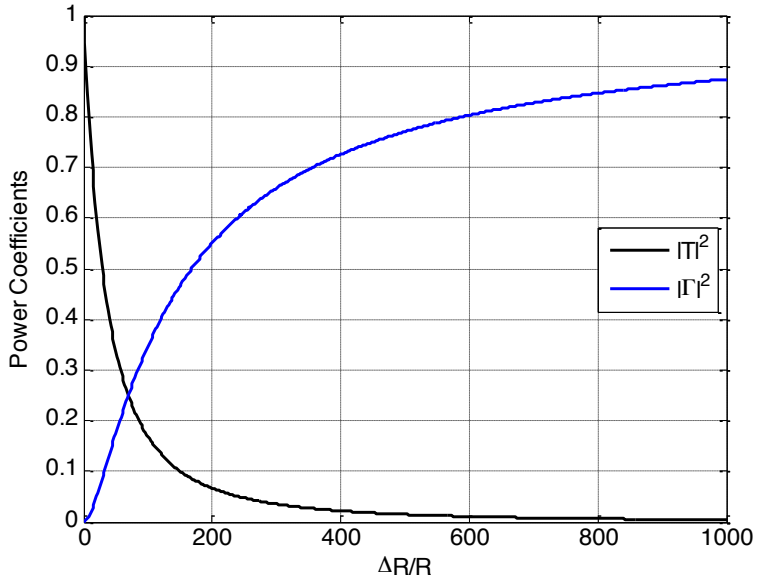


Figure 3.5 Power coefficient vs. $\Delta R/R$

(a)

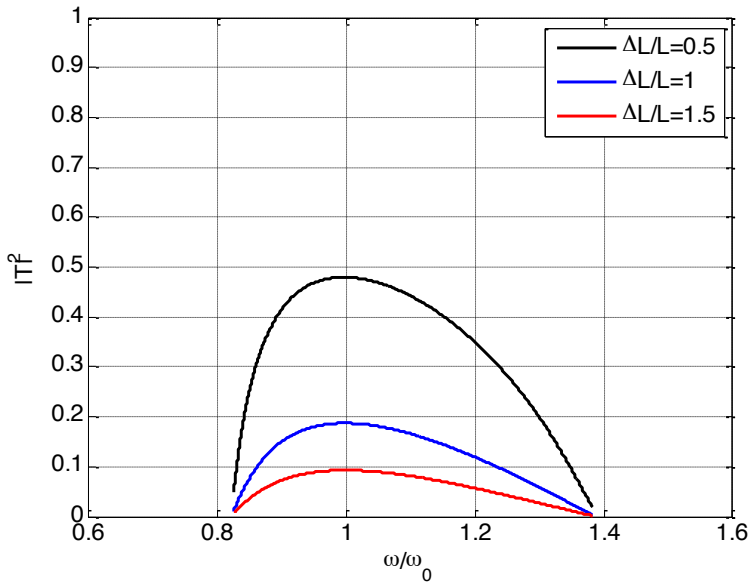


(b)

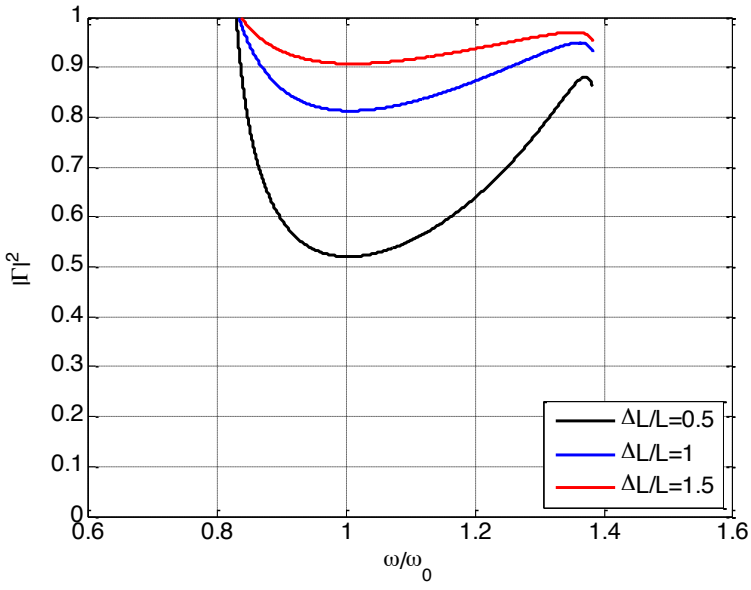


Figure 3.6 Power coefficient vs. Frequency with inductive transducer: (a) Transmission (b) Reflection

Figure 3.6 shows the variation of $|\Gamma|^2$ and $|T|^2$ with $\omega/\omega_0$ when $Z = R + j\omega(L+\Delta L) + 1/(j\omega C)$. The mismatch impedance $\Delta Z$ equals to $j\omega\Delta L$. The impedance of other resonators in the line and the coupling between elements are unaltered. The transmission is high near the center of band and decrease gradually toward the band edge. At the mid-band, the transmitted power decrease by half when $\Delta L = 0.5L$. If the relative inductive mismatch increased from zero, the transmitted and reflected power curves are shown in Figure 3.7. It shows the same trend. The reflected power gradually increases from zero as $\Delta L/L$ increases.

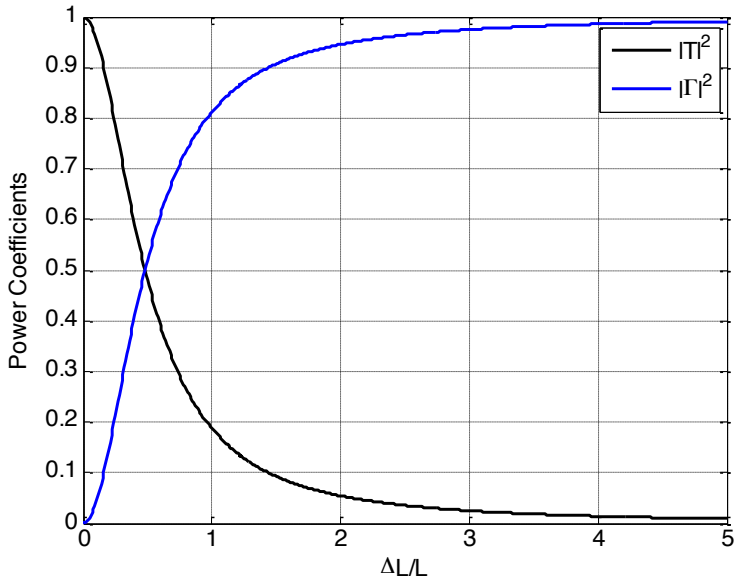


Figure 3.7 Power coefficient vs. $\Delta L/L$

The transmitted and reflected power coefficients are estimated over the passband if we assume the capacitance is tunable. The self-impedance becomes $Z=R+j\omega L+1/(j\omega(C+\Delta C))$. The curves with $\Delta C/C=0.5$, $\Delta C/C=1$ and $\Delta C/C=1.5$ are shown in Figure 3.8.

(a)

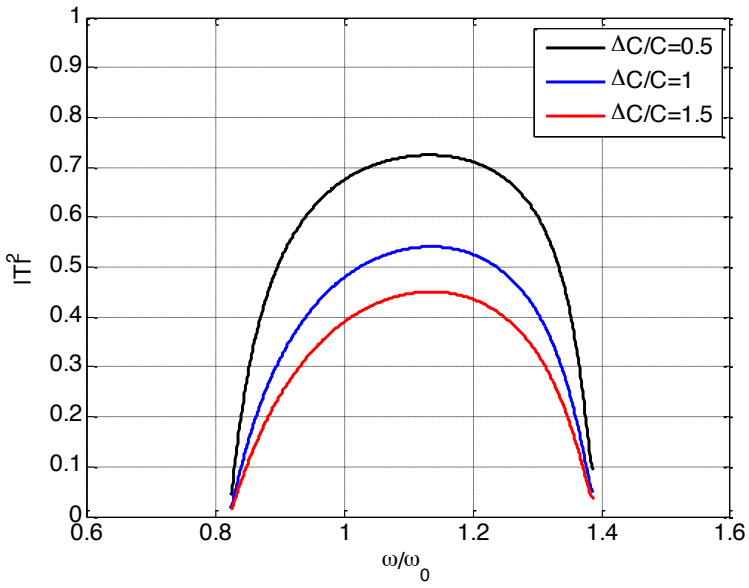


(b)

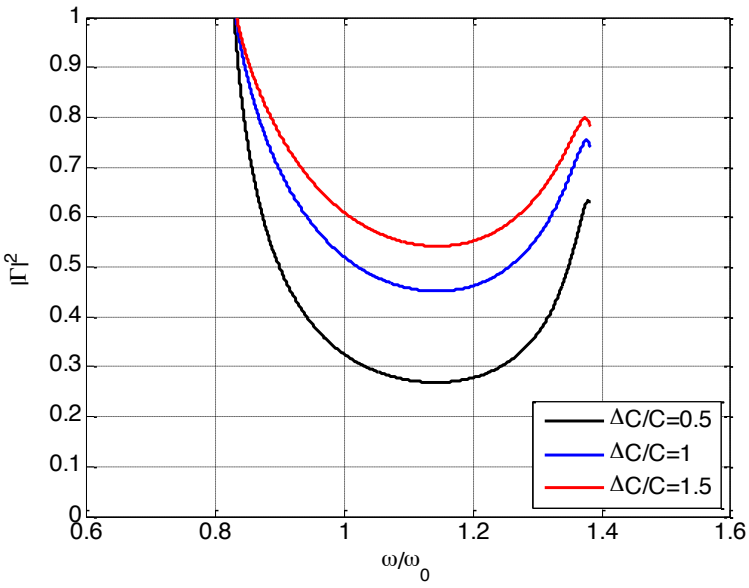


Figure 3.8 Power coefficient vs. Frequency with capacitive transducer: (a) Transmission (b) Reflection

Figure 3.8 also shows greater mismatch with the stronger reflection. The power coefficients $|\Gamma|^2$ and $|T|^2$ as a function of capacitance are shown in Figure 3.9. When $\Delta C/C$=-1, no

resonance in the circuit exists, and the power are all reflected. The transmitted power increases monotonically when total capacitance increase from 0 to the nominal capacitance, then decrease gradually as total capacitance increases. Both $\Delta C/C$=-0.325 and $\Delta C/C$=0.925 reflect half of the power.

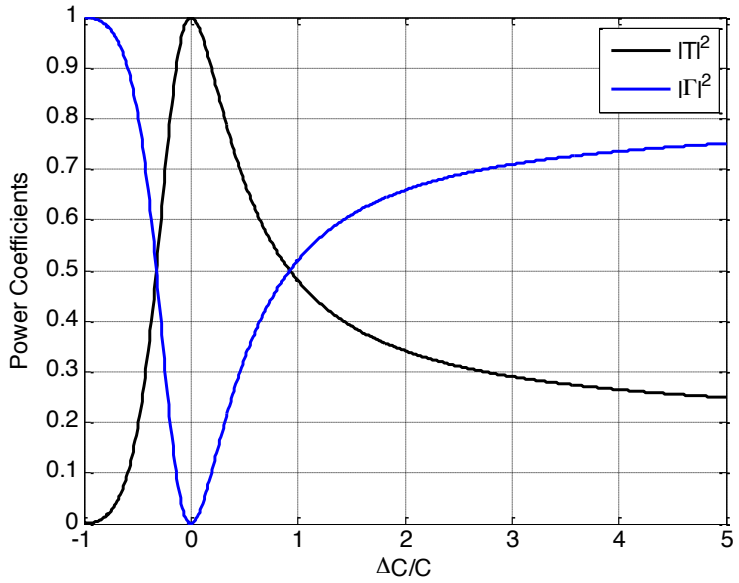


Figure 3.9 Power coefficient vs. $\Delta C/C$

The MI waveguide with mutual impedance discontinuity can be analyzed with the same method. If nearest interaction is taken only, the circuit model is simplified as

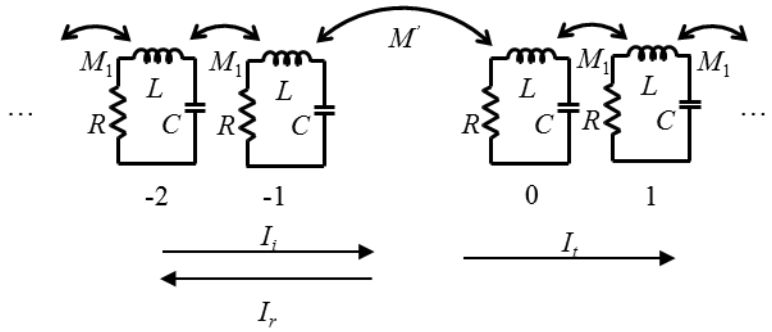


Figure 3.10 Simplified circuit model of 1-D magneto-inductive waveguide with one defect

The -1$^{th}$ element is coupled to its nearest neighbor at the right-side element 0 through mutual inductance $M$' instead of $M_1$. $I_i$, $I_r$, and $I_t$ indicate the incident, reflected, and transmitted

wave caused by mutual inductance discontinuity between element -1 and element 0. The current in the *n*th resonant circuit could be described as

$$I_n = \begin{cases} I_i + I_r = I\exp(-nkd) + \Gamma I\exp(nkd) & n \le -1 \\ I_t = TI\exp(-nkd) & n \ge 0 \end{cases} \tag{3. 12}$$

If only magnetic coupling with its nearest neighbor is considered, the relationship between the currents and voltages at the discontinuity is given as

$$\begin{aligned} ZI_{-1} + X_1 I_{-2} + X_2 I_0 &= 0 \\ ZI_0 + X_1 I_1 + X_2 I_{-1} &= 0 \\ ZI_1 + X_1 I_0 + X_1 I_2 &= 0 \end{aligned} \tag{3. 13}$$

where $X_1$ and $X_2$ are mutual impedance $X_1=j\omega M_1$ and $X_2=j\omega M^{'}$. Then substitute (3.12) into (3.13), and the equation set above yields the following:

$$\begin{aligned} Z_2(1+R) &= X_1 T \\ Z_1(\exp(kd)+\exp(-kd)R) &= X_2 T\exp(kd) \end{aligned} \tag{3.14}$$

The reflection coefficient $\Gamma$ and transmission coefficient $T$ are solved as

$$\Gamma = \frac{(M^{'2} - M_1^2)\exp(kd)}{M_1^2\exp(kd) - M^{'2}\exp(-kd)} \tag{3.15}$$

$$T = \frac{M_1 M^{'}(\exp(kd) - \exp(-kd))}{M_1^2\exp(kd) - M^{'2}\exp(-kd)} \tag{3.16}$$

(3.15) and (3.16) can be simplified as the following expression with $\mu = M^{'}/M_1$

$$\Gamma = \frac{(\mu^2 - 1)}{1 - \mu^2\exp(-2kd)} \tag{3.17}$$

$$T = \frac{\mu(1 - \exp(-2kd))}{1 - \mu^2\exp(-2kd)} \tag{3.18}$$

where $\mu$ represents mutual inductance difference. (3.17) shows the strength of reflection dependent on $\mu$ and value of $kd$. All energy will be transmitted when $M_1$equals to $M^{'}$.

(a)

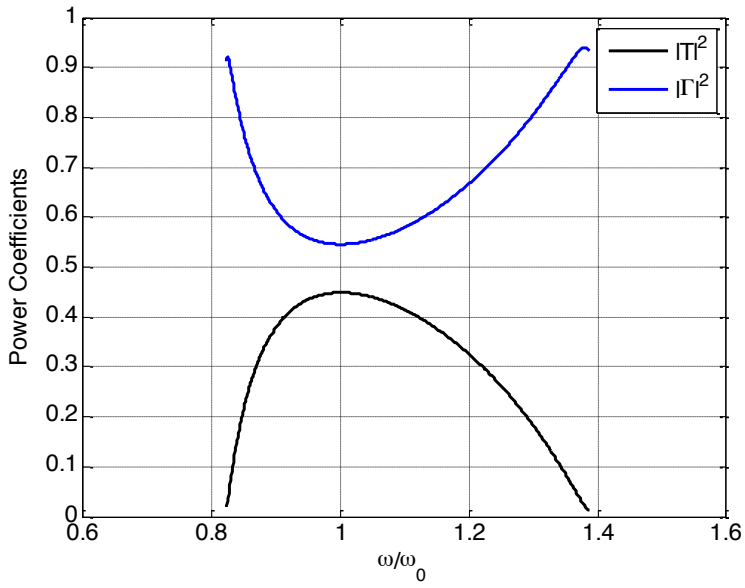


(b)

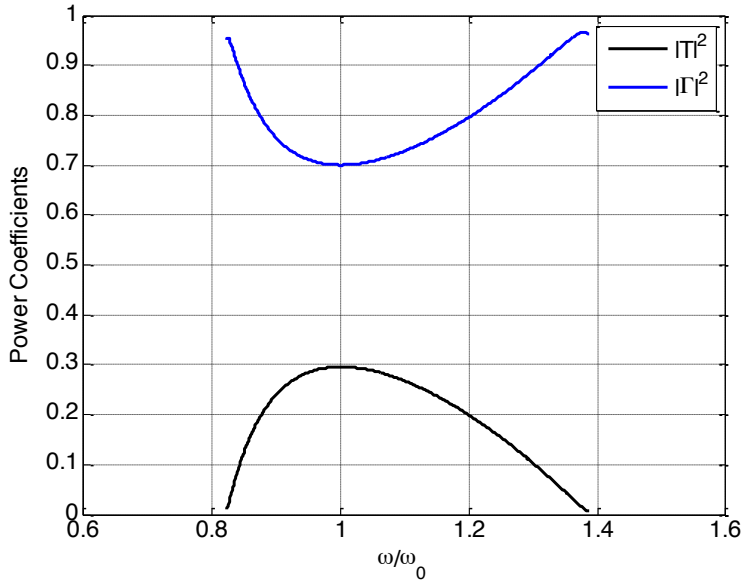


Figure 3.11 Power coefficients vs. Frequency: (a) $\mu$=0.39 (b) $\mu$=0.3

Using the same MI waveguide, if the $n^{th}$ sensor is open in the coaxial array, the $(n\text{-}1)^{th}$ element will be coupled to the $(n\text{+}1)^{th}$ element directly through $M_2$, which results in $\mu$=0.39 with $d$=1.4 cm and $\mu$=0.3 with $d$=2.7 cm. We compare the reflections and transmission coefficients

curves with two values of $\mu$, as shown in Figure 3.11. All curves show that minimum reflection occurs around the resonant frequency, and strong reflections take place towards band edge. The power transmission coefficient is 0.3 with $\mu$=0.3 at mid-band that is 0.45 with $\mu$=0.39, since they have greater impedance discontinuity.

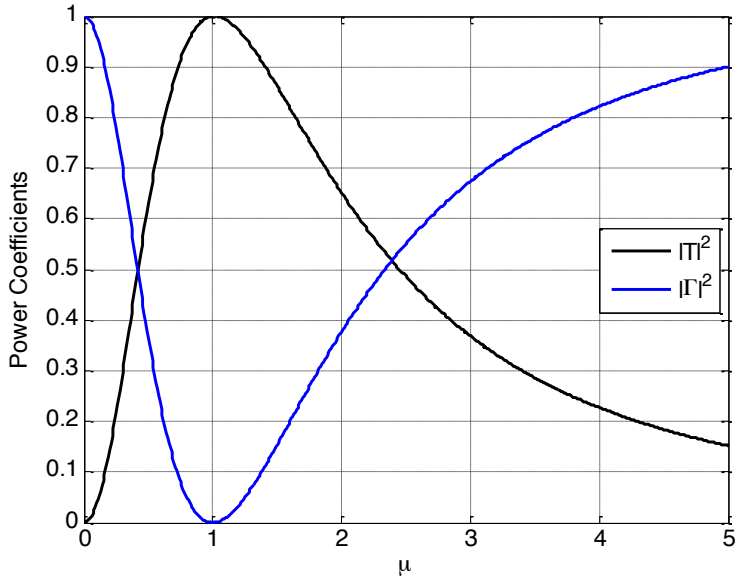


Figure 3.12 Power coefficient vs. $\mu$

The variances of power coefficients $|\Gamma|^2$ and $|T|^2$ are also plotted as $\mu$ increases. When $\mu$=0, there is no coupling between two neighboring elements and no power will be delivered. All power will be transmitted with no mutual inductance difference at the junction. The maximum $\mu$ depends on the value of maximum $M'$ and $M_1$. For MI waveguide with $d$=1.4 cm, the maximum $\mu$ is 4.2.

### 3.2.3 Sensing Mechanism

MI waveguides with different arrangement of coupled resonators have been designed for different applications. We would like to explore the sensing application of an MI waveguide to locate the defect along the line.

Consider a 20-element MI waveguide built with an array of resonant PSCs, the magnetically coupled circuit is implemented in PSpice with $R$=0.8 Ω, $L$=1.36 μH, $C$=101 pF, and $\kappa_1$=0.24. A Vpulse source is connected in a series with the first resonant circuit to generate a square voltage source with period of 20μs and a peak-to-peak value of 10V. The last element is terminated with a resistance of 27.8Ω in series. The current probes are placed in resonant circuits along the array and record the transient current.

Figure 3.13 shows induced currents in Coil 1, Coil 10, and Coil 20 for the 20-element terminated MI waveguide. With group velocity of 346 km/s, the estimated arrival time at Coil 10 and Coil 20 for the wave travels fastest around 0.33μs and 0.7μs. The value is consistent with the result by PSpice simulation, as shown in Figure 3.13. Since MI waves are dispersive, the wave shape gets distorted when propagating, and signal amplitude decreases because of propagation loss. Time-frequency analysis of MI waves will be provided later to increase the precision of locating coil.

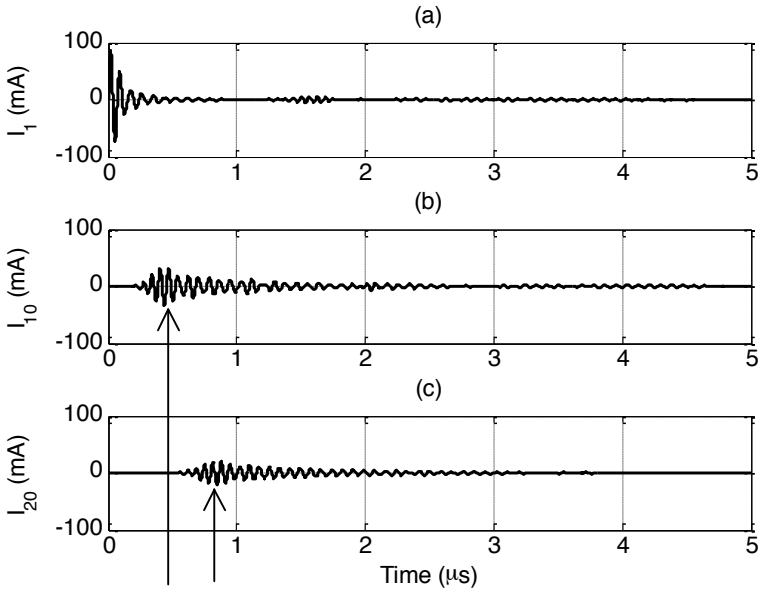


Figure 3.13 Current at different coils: (a) Coil 1 (b) Coil 10 (c) Coil 20

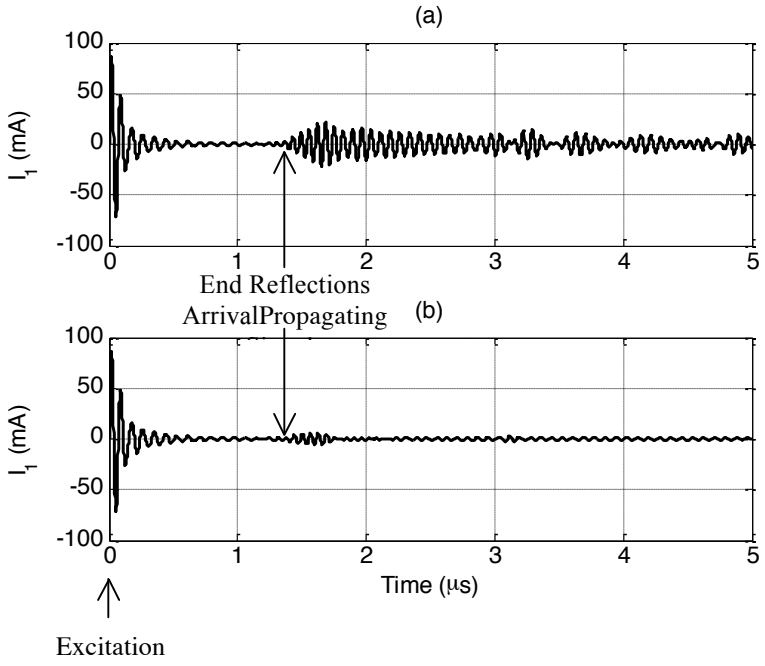


Figure 3.14 Current at diver coil: (a) Without matched load (b) With matched load

Figure 3.14 shows how the 27.8 Ω resistance helps to minimize end reflections. The input rectangular signal initiates the current at first coil at time 0. Figure 3.14(a) presents obvious end reflections that occur due to unmatched termination at the last element, while the most of end reflections are removed with the 27.8 Ω terminator, as shown in Figure 3.14(b). The reflections cannot be completely removed because the resistor is the characteristic impedance at resonant frequency and mismatch still exists over the band, thus weak end reflections are still observed in Figure 3.14(b).

With the group velocity study in Section 2.3.3, the frequency component at $\omega/\omega_0$=1.2 propagate with a maximum group velocity of 346 km/s with coupling only from its nearest neighbor. The travel distance is 0.48 m for a round-trip along the 20-element MI waveguide. The estimated arrival time is around 1.4μs by travel distance over group velocity, which matches

what we see in Figure 3.14. This is a rough method to determine the location of reflection—by investigating the relationship between distance and time given the group velocity.

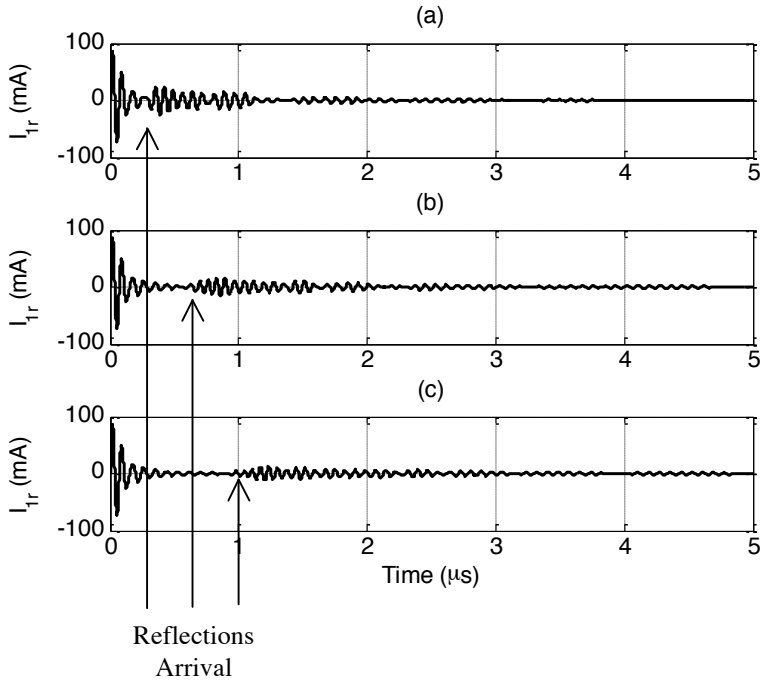


Figure 3.15 Current at driver coil with different locations of defect ($\Delta R$=50$R$): (a) Coil 5 (b) Coil 10 (c) Coil 15

If one defect is shown in the one-dimensional MI waveguide, it is a "mirror" introduced in the transmission line and reflections take place. Current probe at Coil 1 record both the incident signal and reflected signal. Figure 3.15 shows the current in Coil 1 with different locations for impedance discontinuities. The discontinuity is introduced by adding resistance $\Delta R$=50$R$ at Coil 5, Coil 10, and Coil 15, respectively. The reflected power coefficients are 0.34 by Figure 3.5. The arrival of reflected waves due to Coil 10 and Coil 15 are observed clearly at 0.66μs and 1.03μs, as shown in Figure 3.15(b) and (c). But the reflected signal by impedance discontinuity at Coil 5 overlaps with the excitation current, making it difficult to determine the arrival time. Thus, our solution is to subtract the baseline signal (Figure 3.14(a)) from the combined signal. The pure reflected signal is obtained as show in Figure 3.16.

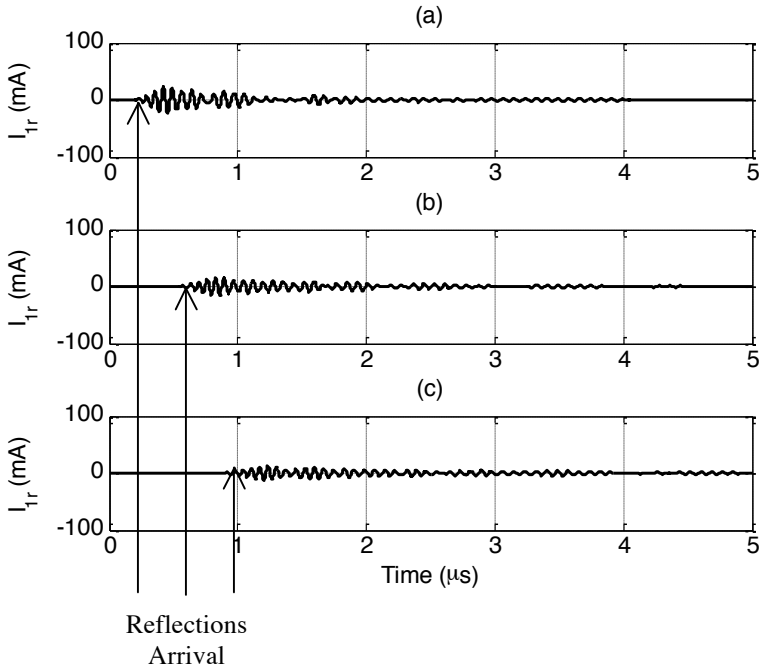


Figure 3.16 Reflected current at driver coil with different location of defect ($\Delta R$=50$R$): (a) Coil 5 (b) Coil 10 (c) Coil 15

Figure 3.16 gives a clear view of reflected waves. The arrival times are 0.3μs, 0.66μs, and 0.98μs, respectively. We also apply two other kinds of impedance as discussed in Section 3.2.2. The inductive case is to increase the self-inductance to 1.5 times the nominal value at Coil 5, Coil 10, and Coil 15, respectively. Then, the same PSpice simulations are run, and the results are shown in Figure 3.17.

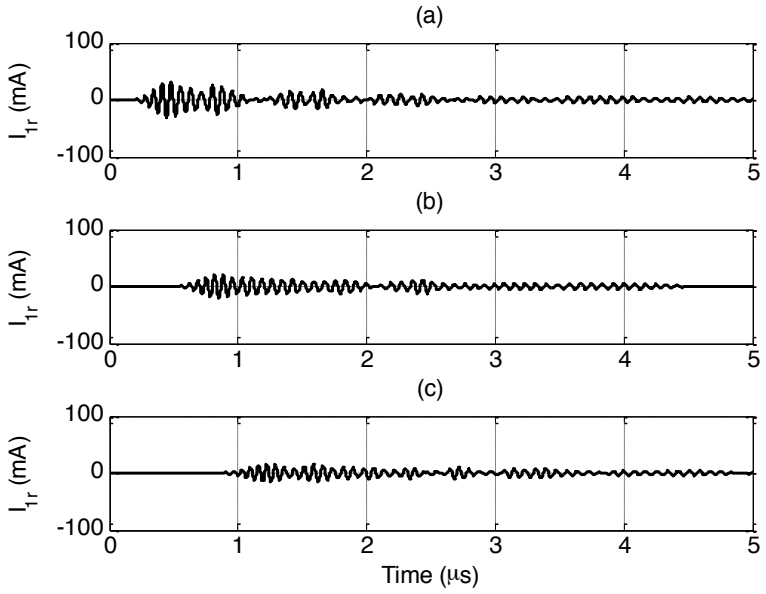


Figure 3.17 Reflected current at driver coil with different location of defect ($\Delta L$=0.5$L$): (a) Coil 5 (b) Coil 10 (c) Coil 15

Half of the power is reflected back based on our analysis in the previous section, and the wave packet amplitude in Figure 3.17 is larger than the waves shown in Figure 3.16 with $\Delta R$=50$R$. The impedance discontinuity also is implemented in the form of capacitance change. Figure 3.18 is the pure reflected current signal with modified capacitance of 1.5$C$ at Coil 5, Coil 10, and Coil 15, respectively. The corresponding power reflection coefficient is 0.39, showing that the signal strength is larger than the result in Figure 3.16 but smaller than that in Figure 3.17. Compare the nine figures in Figure 3.16–3.18. The arrival times of wave packet are only related to the position of discontinuity but not the type of discontinuity. The severity can be estimated by the signal strength of reflected waves.

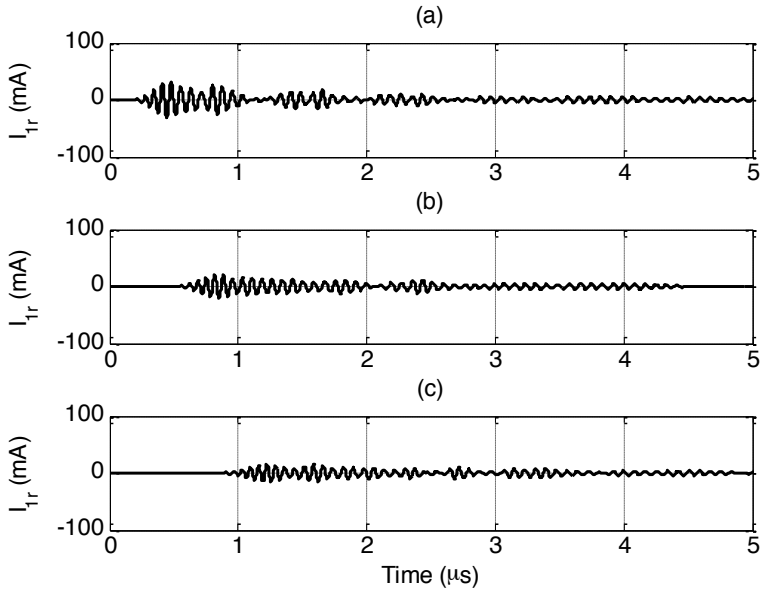


Figure 3.18 Reflected current at driver coil with different location of defect ($\Delta C$=0.5$C$): (a) Coil 5 (b) Coil 10 (c) Coil 15

In reality, to implement our sensing mechanism, MI waves must be recorded. It is hard to measure MI waves in the medium where the resonators are placed. Our solution is to observe the time-varying current in the resonator circuit. In the time domain, the current in an element will generate further current in its neighboring element. MI waves are incited by a step signal at the first coil, since the step signal contains a wide range of frequencies, while only the band around the resonant frequency can be supported. When an impedance mismatch takes place in the MI waveguide, the reflected current can be monitored by a current probe at the driver coil.

## 3.3 LOW-LOSS MI WAVEGUIDE WITH DISTRIBUTED DEFECTS

### 3.3.1 Circuit Model

One-dimensional MI waveguides with one defect have been investigated in the previous section. If each resonator combines with a transducer that reacts the same way, the MI waveguide is essentially still uniform but exhibits different resonator circuit parameters. Since it

is uniform along the line, so no reflections are expected. For example, if the resistive transducers along the MI waveguide were to corrode to the same extent, the extra resistance introduced for each element would be consistent. Then the self-impedance of each element changes, the dispersion relationship and characteristic impedance for the updated MI waveguide is modified. With different kinds of transducers, the lumped-element circuit model in general becomes

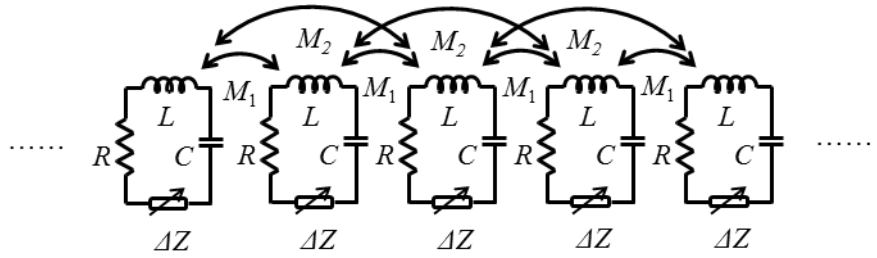


Figure 3.19 Circuit model of MI waveguide with distributed self-impedance defects

In Figure 3.19, self-impedance $Z_n^{'}$ for each element is $R+j\omega L+1/(j\omega C)+\Delta Z$ and mutual inductance $M_i$ ($i$=1,2,…) is unaffected. $\Delta Z$ indicates the impedance change by the attached transducer. If $\Delta Z$ is resistive, only the quality factor changes; if $\Delta Z$ is inductive or capacitive, both resonant frequency and quality factor change. The supported MI waves are subject to a new dispersion relationship. The current distribution along an $N$-element terminated array can also be solved by the following equation with self-impedance $Z_n^{'}$ with the circuit model in Figure 3.19.

$$\begin{bmatrix} Z_1^{'} & j\omega M_1 & \cdots & j\omega M_S & & & & \\ j\omega M_1 & Z_2^{'} & j\omega M_1 & \cdots & & & & \\ \cdots & \ddots & \ddots & \ddots & \cdots & & & \\ & \cdots & j\omega M_1 & Z_n^{'} & j\omega M_1 & \cdots & & \\ & & \cdots & \ddots & \ddots & \ddots & \cdots & \\ & & & \cdots & j\omega M_1 & Z_{N-1}^{'} & j\omega M_1 & \\ & & & j\omega M_S & \cdots & j\omega M_1 & Z_N^{'}+Z_t & \end{bmatrix} \begin{bmatrix} I_1 \\ I_2 \\ \vdots \\ I_n \\ \vdots \\ I_{N-1} \\ I_N \end{bmatrix} = \begin{bmatrix} V_1 \\ 0 \\ \vdots \\ 0 \\ \vdots \\ 0 \\ 0 \end{bmatrix} \tag{3.19}$$

Another case tests the bending, compression, or uniformed stretching of the MI waveguide, in which case the individual element is unaltered while mutual coupling between elements changes based on the new gap between elements along the array. This type of guide can be modeled by

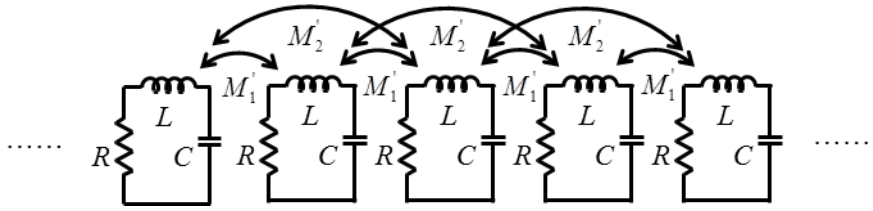


Figure 3.20 Circuit model of MI waveguide with distributed mutual impedance defects

The propagating MI waves characteristics is also modified due to the updated mutual inductance between elements, although the quality factor and resonant frequency remain constant. The lumped-element circuit model can be described in (3.20), and bends, compression, or stretches are simulated by a variation of mutual inductances:

$$\begin{bmatrix} Z_1 & j\omega M_1' & \cdots & j\omega M_s' & & & & \\ j\omega M_1' & Z_2 & j\omega M_1' & \cdots & & & & \\ \cdots & \ddots & \ddots & \ddots & \cdots & & & \\ & \cdots & j\omega M_1' & Z_n & j\omega M_1' & \cdots & & \\ & & \cdots & \ddots & \ddots & \ddots & \cdots & \\ & & & \cdots & j\omega M_1' & Z_{N-1} & j\omega M_1' & \\ & & & j\omega M_S' & \cdots & j\omega M_1' & Z_N + Z_t & \end{bmatrix} \begin{bmatrix} I_1 \\ I_2 \\ \vdots \\ I_n \\ \vdots \\ I_{N-1} \\ I_N \end{bmatrix} = \begin{bmatrix} V_1 \\ 0 \\ \vdots \\ 0 \\ \vdots \\ 0 \\ 0 \end{bmatrix} \tag{3.20}$$

### 3.3.2 Transmission and Reflection

Consider an $N$-element MI waveguide consists of a linear array of resonators with self-impedance $Z_n'=R+j\omega L+1/(j\omega C)+\Delta Z$. The last element is terminated with impedance $Z_t$, as shown in Figure 3.21.

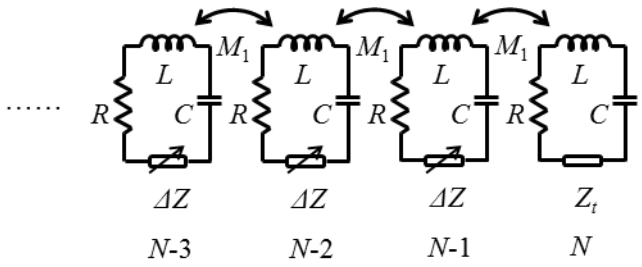


Figure 3.21 Simplified circuit model of MI waveguide with distributed self-impedance defects

In Figure 3.21, $Z_t$ is the matched impedance $\omega_0 M_1$ with $\omega_0 = 1/(2\pi\sqrt{(LC)})$. Extra end reflections are introduced by the mismatch at the last element since the characteristic impedance of the modified MI waveguide can be changed due to $\Delta Z$. The end reflection coefficient with load $Z_t$ is

$$\tau = \frac{Z_t - Z_t^{'}}{Z_t + Z_t^{'}} \tag{3.21}$$

where $Z_t^{'}$ is the characteristic impedance $j\omega M_1 \exp(-k^{'} d)$ for an MI waveguide with self-impedance $Z_n^{'}$, and $k^{'}$ is the propagation constant of MI waves solve by the dispersion relationship with updated resonant frequency and quality factor. When $\Delta Z$ is not zero, the characteristic impedance at mid-band changes due to the new propagation constant. Figure 3.22 shows the end reflections with difference resonator circuit parameter:

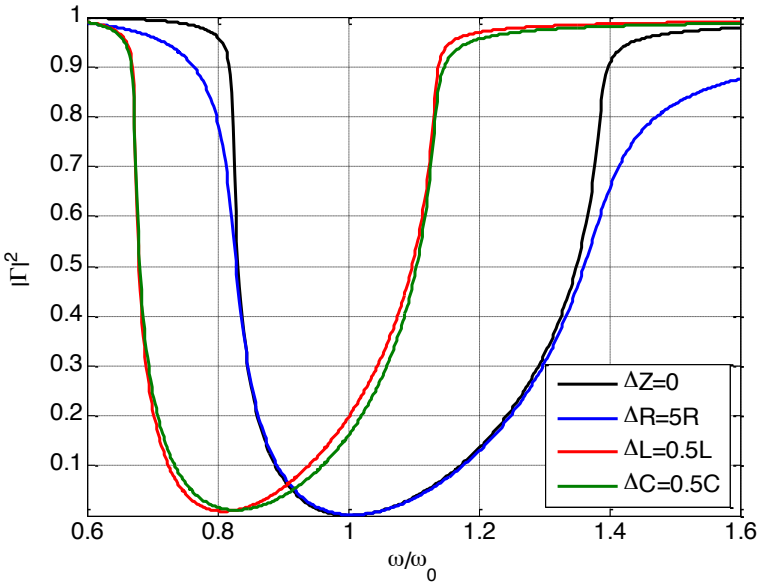


Figure 3.22 Power reflection coefficients vs. Frequency for MI waveguide with distributed self-impedance defects

The x-axis is normalized to the angular resonant frequency with $f_0$=13.56 MHz. The applied circuit parameters are $R$=0.8 Ω, $L$=1.36μH, $C$=101 pF, and $M_1$=0.33μH with gap $d$=1.4 cm. The black curve is the end reflection coefficient without any self-impedance change. The extra resistance of 5$R$ does not increase the end reflections over the passband. When the inductance of all elements increases by 0.5$L$, the propagating signal above frequency $\omega/\omega_0$=1.14 is nearly reflected. If the capacitances are tuned at 1.5$C$, the power reflection coefficient curve is similar to the curve with $\Delta L$=0.5$L$ for the same reason.

The characteristic impedance is also affected by mutual inductance $M_1$. With an $N$-element MI waveguide, if the axial spacing changes due to an external force, the mutual inductance could increase or decrease from the nominal value, as shown in Figure 3.23 with the same individual lumped-element circuit components.

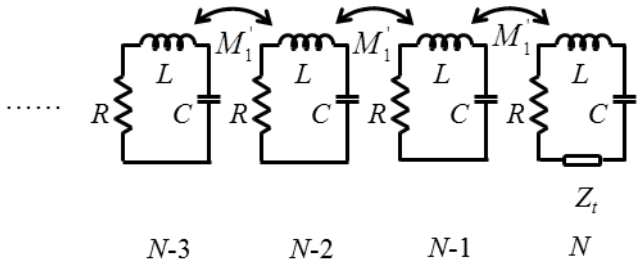


Figure 3.23 Simplified circuit model of MI waveguide with distributed mutual impedance defects

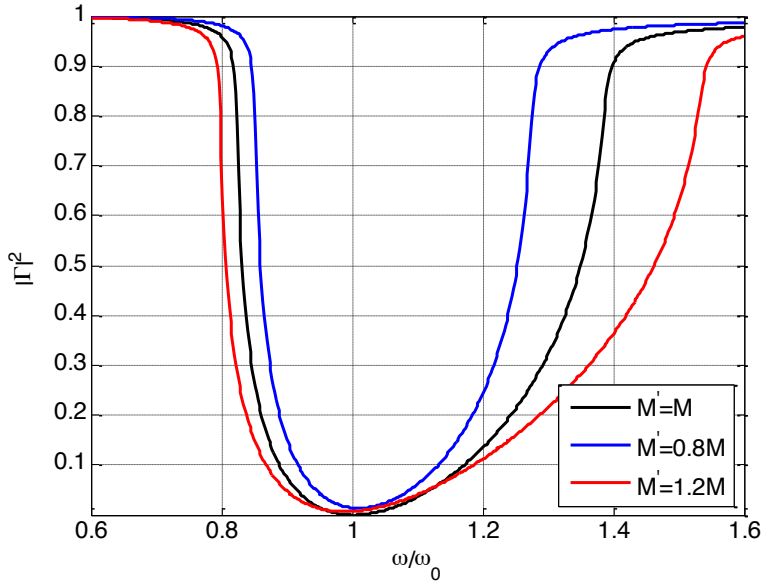


Figure 3.24 Power reflection coefficients vs. Frequency for MI waveguide with distributed mutual impedance defects

Figure 3.24 shows the variation of power reflection coefficients $|\Gamma|^2$ with different mutual inductance. The transmission is high in the mid-band for all three curves. The reflections are stronger with smaller mutual inductance at a frequency further away from mid-band due to the impedance mismatch. This also reflects the passband width that an MI waveguide with different mutual inductance can support. With the analysis in Section 2.3, the passband width of the MI waveguide is proportional to the coupling factor, and the MI waveguide with $M'=1.2M$ can support band $0.8 \leq \omega/\omega_0 \leq 1.54$. It agrees with the band shown in Figure 3.24.

### 3.3.3 Sensing Mechanism

MI waveguides with distributed defects described in previous section do not introduce impedance discontinuity along the line. The change of frequency-dependent characteristic impedance introduces end reflections. As an illustration, we chose the same axial MI waveguide described in Section 3.2.3 with parameters $N$=20, $R$=0.8 Ω, $L$=1.36μH, $C$=101 pF, and $\kappa_1$=0.24. The first element is driven by a square voltage $V$, while the last element being terminated with resistance of 27.8Ω.

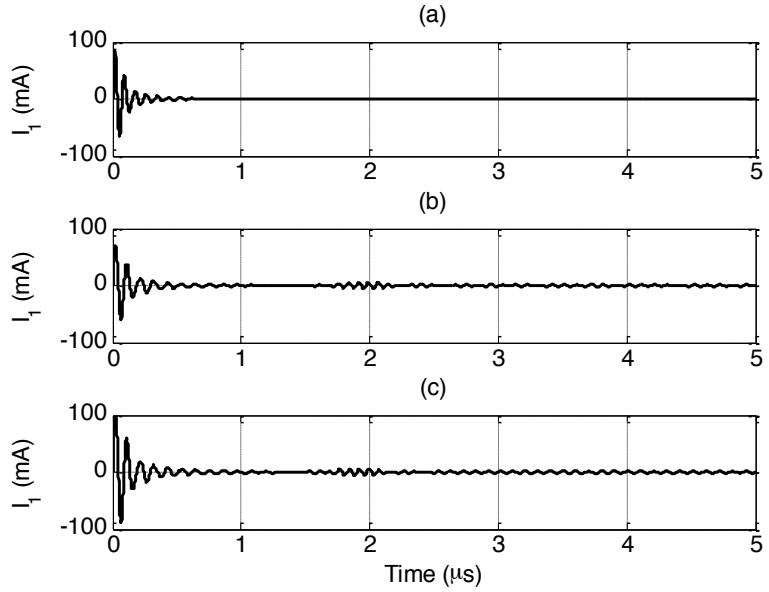


Figure 3.25 Current at driver coil: (a) Δ$R$=5$R$ (b) Δ$L$=0.5$L$ (c) Δ$C$=0.5$C$

We show the current in the diver coil for the MI waveguide with different self-impedance changes in Figure 3.25. The quality factor decreases to 19.7, the energy of reflected waves are dissipated along the line and no end reflections are observed in Figure 3.25(a). So a high-$Q$ element is critical for MI waveguides to support propagating waves. Figure 3.25(b) is the current signal in the driver coil that includes incident signal and end reflections. The updated quality factor, resonant frequency, and coupling factor are 177, 11.1 MHz, and 0.16, respectively. The end reflections happen at Coil 20 and travel back to the driver coil after 1.7$\mu$s. That is slower

than the reflected signal when $\Delta Z=0$ in Figure 3.13(b) because the corresponding group velocity is less than that of the original MI waveguide, as shown in Figure 3.26. When the capacitance is modified by $\Delta C=0.5C$, the reflected wave spends the same amount of time to propagate back. This can be also explained by the group velocity curve in Figure 3.26.

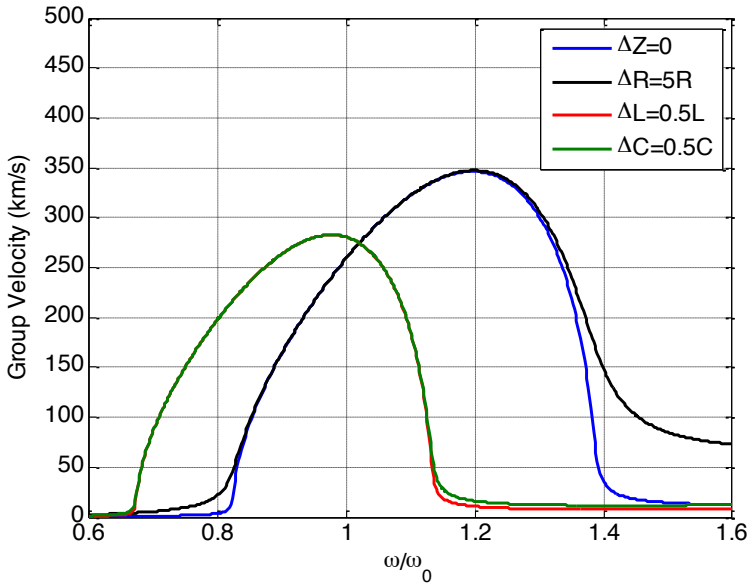


Figure 3.26 Group velocity vs. Frequency with different self-impedance

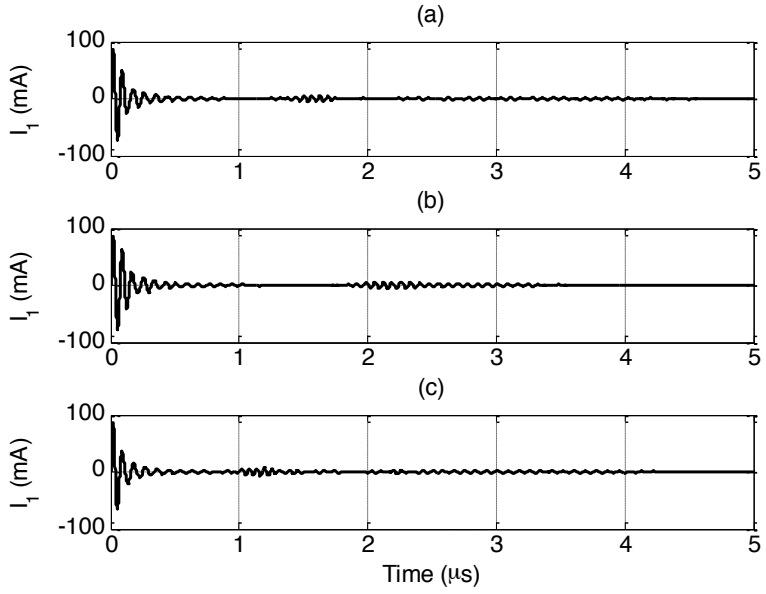


Figure 3.27 Current at driver coil: (a) $M^{'}=M$ (b) $M^{'}=0.8M$ (c) $M^{'}=1.2M$

Figure 3.27 shows how the mutual inductance affects the property of propagating MI waves. The MI waveguide is still uniform. It is shown that the wave packet with strong coupling can propagate travel fast along the guide. In Figure 3.27, the arrival times for $M^{'}$=0.8$M$, $M^{'}$=$M$, $M^{'}$=1.2$M$ are 1.95μs, 1.4μs, and 1μs, respectively. The corresponding maximum group velocity is 254 km/s, 345 km/s and 483 km/s, as shown in Figure 3.28. The proposed method is to monitor the arrival time of end reflections, calculating the new group velocity, analyzing the reflected MI signal in the time domain.

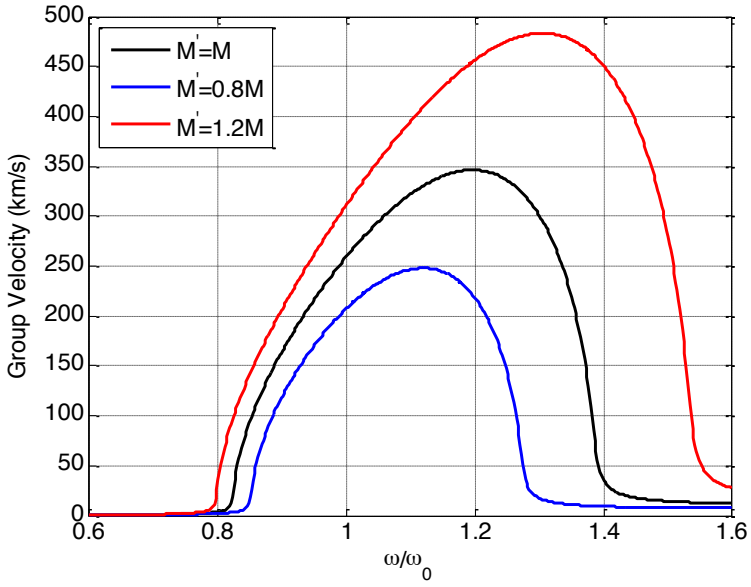


Figure 3.28 Group velocity vs. Frequency with different mutual inductance

## 3.4 SUMMARY

MI waveguides with both one and distributed defects were investigated in this chapter. The transmission and reflection coefficients were solved as functions of frequency and impedance match based on the circuit model of MI waveguides. For MI waveguides with one defect, reflected waves took place due to the impedance discontinuity along the coupled array

and were observed by implementing the circuit model in PSpice. The reflected MI signal was sinc-like in shape because the MI waveguide behaved as a passband filter in the frequency domain. The arrival time of the burst signal depended on the location of discontinuity, and related to the travel distance by group velocity. Thus, the defect is located through multiplying group velocity by the arrival time, and the severity of defect depends on the signal strength of reflected waves. MI waveguides with distributed defects remained uniform, and no reflected waves were introduced, but the end reflections are stronger due to the difference between the load and new characteristic impedance. The group velocity could also be affect when the distributed defect is non-resistive. The proposed method is to monitor the signal strength and arrival time of end reflections to infer the severity of defect.

# Chapter 4 Experimental Results and Analysis

## 4.1 INTRODUCTION

The purpose of this chapter is to present experimental results for developed one-dimensional MI waveguide with and without defects and verify the proposed sensing mechanism. First, the MI waveguide are constructed by equally spaced PSCs designed in Section 2.2. Then, the passband characteristics in frequency domain are measured for MI waveguides with different length and axial spacing to verify low-loss property. Furthermore, a pitch-catch measurement system is built to detect traveling MI signal in time domain, and a pulse-echo measurement system is designed to monitor reflected MI signal. The MI signal in time domain are captured and analyzed by TFR methods. Smoothed SWVD is the TFR method to be adopted. Experimental results investigating the waveguide with one defect and distributed defects conclude this section.

## 4.2 LOW-LOSS MI WAVEGUIDE

One-dimensional MI waveguides are constructed by an array of inductively coupled print spiral coil resonators, as shown in Figure 4.1.

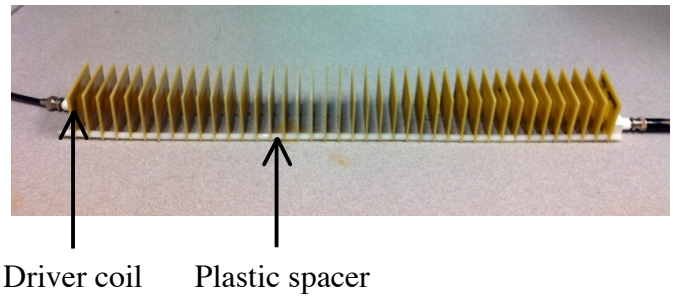


Figure 4.1 Photo of low-loss MI waveguide with $d$=1.4 cm

The first element serves as the driver coil, and the last element is terminated with mid-band–matched impedance $\omega_0 M_1$. In this case, it is a resistor of 27Ω. All resonant elements are aligned by inserting a plastic spacer. The driver coil will be connected to a power source to excite MI waves propagating along the inductively coupled array. In the experiment, the transducer is not added to each sensor. We simulate the defect by inserting a resistor or capacitor, or by opening the circuit directly.

The resonant PSCs are five-turn square-shaped PCS on the FR-4 substrate. An external capacitor of 101 pF is connected in series to tune the resonant frequency as 13.56 MHz. Fifty elements are measured showing that they resonate in the frequency range of 13.6±0.1 MHz and have quality factors of 161±12. The resonators are placed coaxially and separated equally by inserting plastic spacers between them, as shown in Figure 4.1.

## 4.3 VALIDATION OF LOW-LOSS MI WAVEGUIDE

We first measure the insertion loss of designed coaxial MI waveguide without any defects to verify the low propagation loss. The tests are repeated with different axial spacing and different length.

### 4.3.1 Frequency Domain Experimental Setup

The frequency responses are firstly obtained for MI waveguides with different axial separations *d*, which are 1.4 cm and 2.7 cm. Resistors with a value of 27Ω and 11Ω are chosen to terminate the two waveguides respectively. The data are acquired using the HP 4194A Impedance/Gain-Phase Analyzer. The experimental set-up schematic diagram is shown in Figure 4.2.

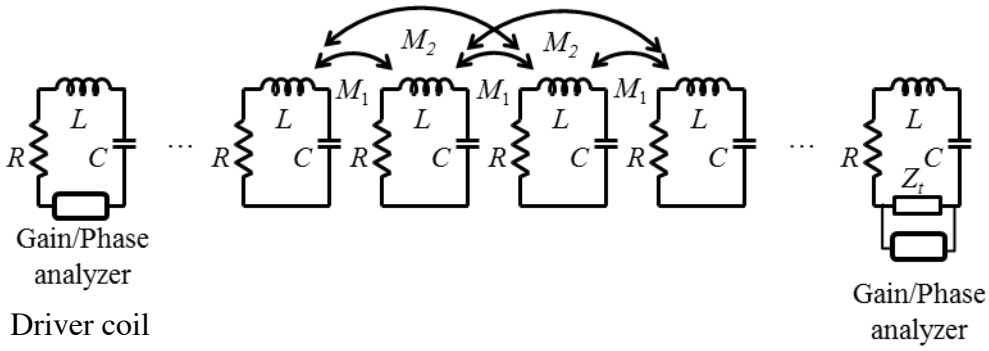


Figure 4.2 Schematic diagram of frequency domain measurement set-up

In Figure 4.3, the driver coil connects the input port of the HP 4194A Impedance/Gain-Phase Analyzer through BNC connector, while the output port is connected across the matched impedance at the last coil. The experimental setup photo is shown in Figure 4.3.

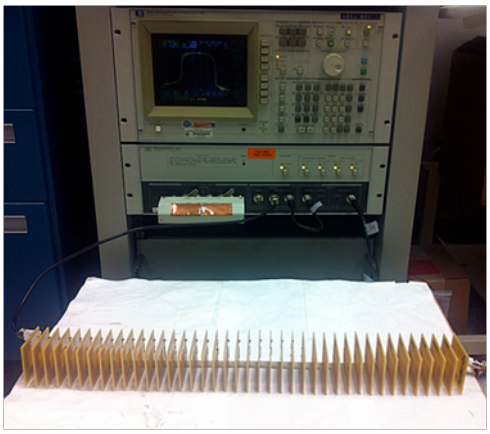

Figure 4.3 Photo of frequency domain measurement set-up

### 4.3.2 Results and Validations

The measured insertion loss curves for one-dimensional coaxial resonator arrays with $d$=1.4 cm and $d$=2.7 cm are presented in Figure 4.3. Both MI waveguide consists of 20 resonant PSCs. The x-coordinate is normalized to the frequency of 13.6 MHz.

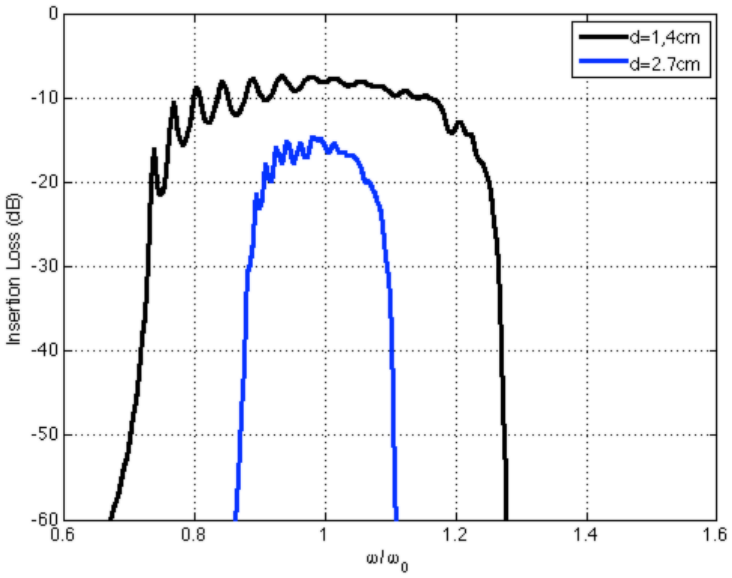


Figure 4.4 Insertion loss vs. Frequency with different axial spacing

The two curves in Figure 4.4 both show that they can only support a band around element resonant frequency. Narrower spacing ($d$=1.4 cm) holds wider passbands and higher transmissions due to stronger coupling. The measured width of a passband for the MI waveguide with $d$=1.4 cm is around 7.32 MHz while the value decrease to 2.71 MHz with double spacing. The values agree with the simulated results in Section 2.3.2. The minimum insertion loss for the 20-element MI waveguide that happens at the mid-band is -7.4 dB for $d$=1.4 cm and -14.7 dB for $d$=2.7 cm. High transmission is obtained during the passband; however, small ripples take place toward the band edge because the resistive load cannot match the characteristic impedance over the all band.

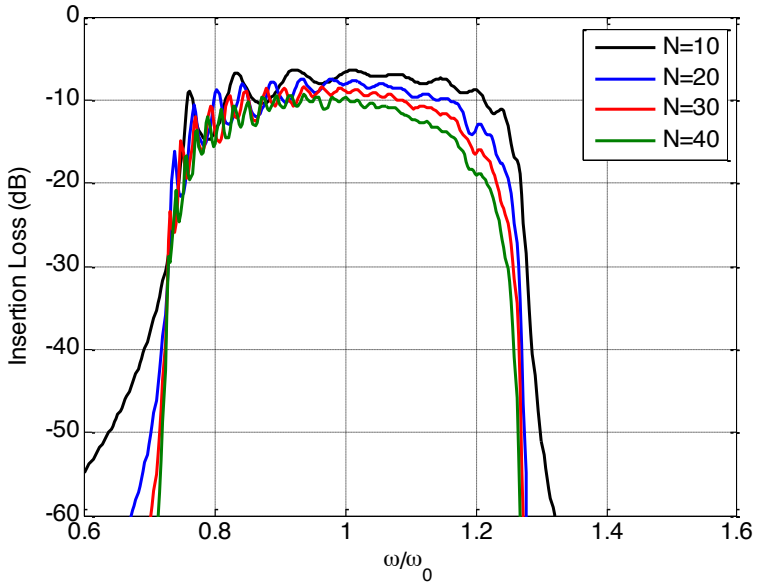


Figure 4.5 Insertion loss vs. Frequency with different length

Figure 4.5 shows the experimental insertion loss for an MI waveguide ($d$=1.4 cm) of different length. The number of elements rises to 40. The results demonstrate that the insertion loss increase with more number of elements making up an MI waveguide while the passband width remains unchanged.

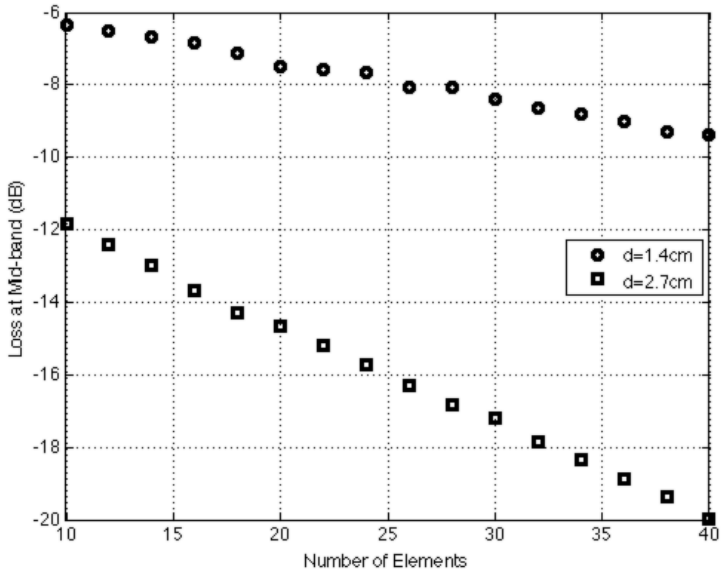


Figure 4.6 Mid-band loss vs. Number of elements

The test is repeated with two different axial spacing. We extract the insertion loss at mid-band from $N$=10 to $N$=40 and plot the value in Figure 4.6 as a function of the number of elements. It shows that the mid-band insertion loss for MI waveguides rises almost linearly. When the axial separation is greater, the linked flux will leak into the air instead of coupling to the next coil. With axial separation of $d$=1.4 cm, the average additional loss per element is about 0.098 dB, and for the 2.7 cm-resonator array 0.27 dB by the slope. The results are in accord with the simulation results of 0.096dB and 0.27dB in Section 2.3.4.

### 4.3.3 Time Domain Experimental Setup

The time domain experiment is used to verify the group velocity of supported MI waves. The induced current by travelling MI waves is recorded at the end element. The schematic diagram to measure propagating MI wave signal is shown in Figure 4.7.

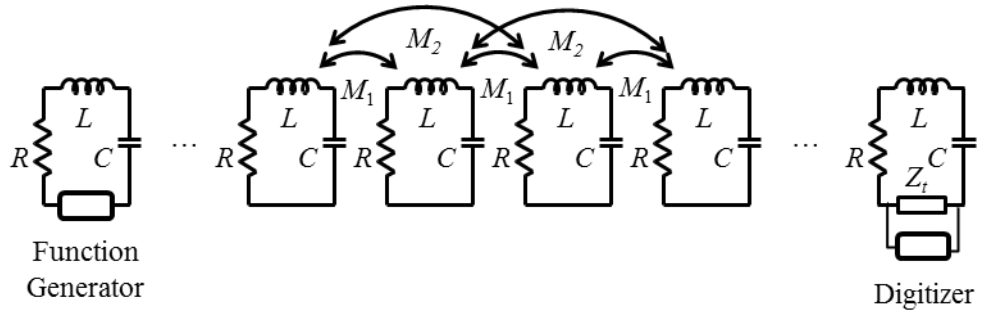


Figure 4.7 Schematic diagram for MI waveguide for pitch-catch measurement

The MI waveguide under test is driven by a function generator in the first coil. A digitizer is connected across the resistive load to measure the voltage and then deduce the current signal at the final coil. A measurement system is built to provide the source and record the current signal when the waves arrive at the end.

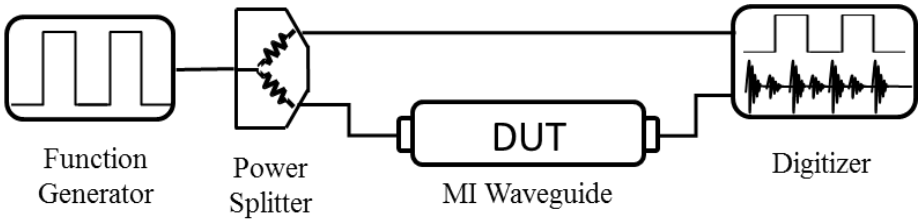


Figure 4.8 Schematic diagram of pitch-catch measurement setup

The pitch-catch measurement system is designed in Figure 4.8 and consists of a function generator, a 3-dB power splitter, an MI waveguide as device under test (DUT), and a digitizer. A 3-dB power splitter is inserted between the function generator and the MI waveguide so that the digitizer can monitor the excitation signal at the first coil and the arrival signal at the last element simultaneously. Only then the time-of-flight can be observed by comparing the two signals.

### 4.3.4 Results and Validations

To measure the traveling MI signal, the digitizer is connected across the resistor at the final element but not elements between, in case reflections take place due to the introduced impedance mismatch. The digitizer is served as a voltage probe, and current information can be obtained through voltage divided by resistance. MI waveguides with different lengths are built and the current signals at the end are recorded. The real measurement system is shown in Figure 4.9 as follows:

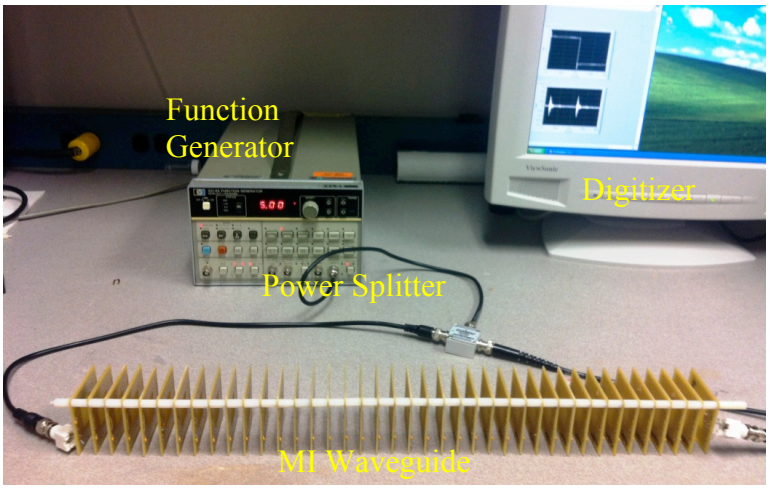


Figure 4.9 Photo of pitch-catch measurement setup

Figure 4.9 is the measurement system photo. The MI waveguide under test consists of a line of resonators coaxially placed, with separation of 1.4 cm. The HP 3341A arbitrary waveform generator is used to generate square waves with a period of 20μs and a peak-to-peak amplitude of 10V. The signal is divided by a 3-dB power splitter with two equal signals having a decreased peak-to-peak value of 6.5 V. One output port of the power splitter is connected to an NI pxi-5122 digitizer directly to monitor the initiation time of every step, and another port is connected to the first element of the MI waveguide and served to excite the MI signal. The generated MI waves travel along the MI waveguide and are captured at the last element across a 27 Ω terminator.

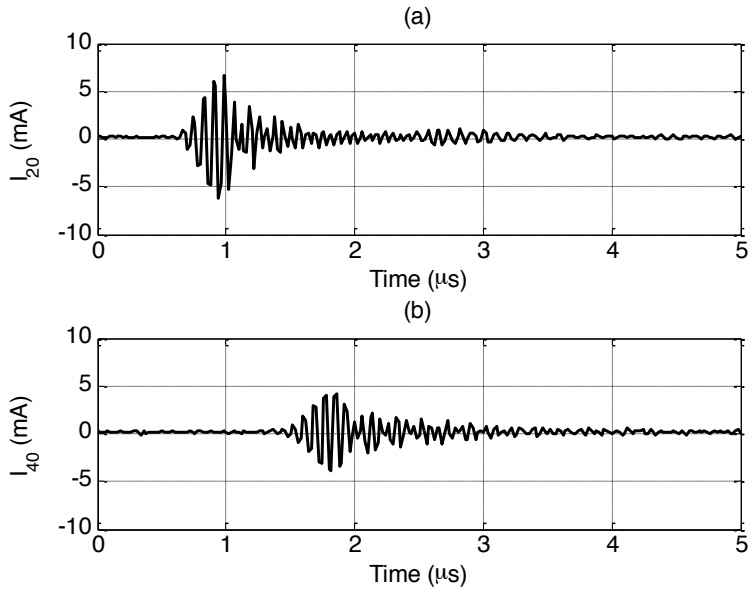


Figure 4.10 Measured transient current: (a) Coil 20 (b) Coil 40

The measurements run for MI waveguides with different lengths. Results for the 20-element and 40-element MI waveguides are shown in Figure 4.10. The received signal is discretized with a sampling frequency of 100 MHz. The arbitrary waveform generator fires at $t$=0, and the transient current value is obtained by the collected voltage across a resistance of 27Ω. From Figure 4.10, the amplitude of wave packet at Coil 40 is smaller than that at Coil 20 due to propagation loss. The induced current at Coil 20 shown in Figure 4.10(a) happens at 0.65μs, and the known travel distance is 0.24 m. The deducted maximum group velocity is 370 km/s, which is close to the simulated maximum group velocity of 372 km/s, taking the three nearest interactions in Section 2.3.3. But it cannot provide the frequency information of arrived signal. In Figure 4.10(b), the arrival time is 1.48μs, and the travel distance for a 40-element MI waveguide with $d$=1.4 cm is 0.5 m. The estimated maximum group velocity is 338 km/s, which is different from the estimated value by a 20-element waveguide. That is because the arrival time is chosen when the first-cycle sinc-like signal is observed. This method could be too rough; thus,

the time frequency representations of MI signals are provided for a more thorough understanding.

### 4.3.5 Extraction of Group Velocity

To relate the measured MI signal with defects more effectively, the group velocity should be provided to give an estimation of how fast MI waves travel along a specific waveguide. In this section, the group velocity over the band is extracted with arrival time and a known travel distance of MI signals. TFR of the signal is presented. We adopt the smoothed Wigner-Ville distribution (WVD) to obtain the 'local' frequency information.

The smoothed WVD method is considered as an intermediate distribution between the short-time Fourier transform (STFT) and the original WVD. The STFT is the simplest example of a TFR. The basic idea is to divide the signal in the time domain into a number of small overlapping pieces [53]. Each piece is windowed and the STFT is applied. It does not suffer from cross-term interference between two signals, but it is unable to undergo satisfactory resolution in the time and frequency domains simultaneously. The original WVD for the signal $s(t)$ is the Fourier transform with respect to $\tau$ of $s(t+\tau/2)s^*(t-\tau/2)$ [53]. It exhibits better temporal and frequency resolutions in general and can locate sinusoids, Dirac impulse, and linear chirps. However, it will introduce additional interference in addition to the desired signals. The smoothed WVD is a compromise between these two demands. The smoothed WVD filters the original WVD with a two-dimensional filter $G$ [53]. The two-dimensional filter $G$ can be used to suppress the interference terms without having much of an effect on the desired signal. To some extent, it sacrifices the time-frequency resolution compared to the original WVD method. The expression for the smoothed WVD is

$$SWVD(f,t) = \int_{-\infty}^{\infty}\int G(f - f', t - t')WVD(f', t')dt'df' \tag{4.1}$$

where

$$WVD(\omega,t) = \int_{-\infty}^{\infty} s(t + \tau/2)s^*(t - \tau/2)e^{-j\omega\tau}d\tau \tag{4.2}$$

The smoothed WVD method with hamming window is applied on the arrival waves in Figure 4.10(a). The window width is chosen as one-quarter of the data length. Figure 4.11 is the smoothed WVD absolute value of the MI waves, with time on the horizontal axis and frequency on the vertical axis. It shows that the maximum spectral amplitude occurs at a frequency of 12 MHz. The MI waveguide can support MI waves with a frequency range of 10.5 MHz to 16 MHz. The experimental frequency component with maximum amplitude and MI waves bandwidth match the minimum attenuation point and passband width in the dispersion relationship shown in Figure 2.18 (b).

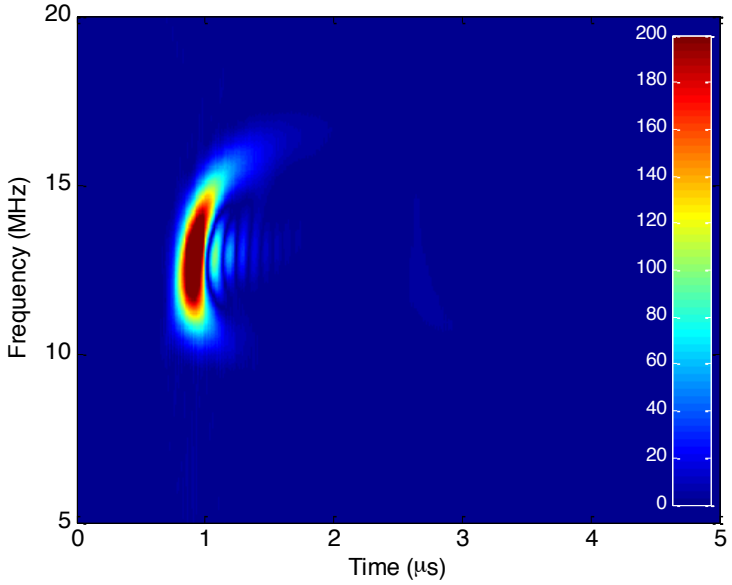


Figure 4.11 Smoothed WVD of MI signal

(a)

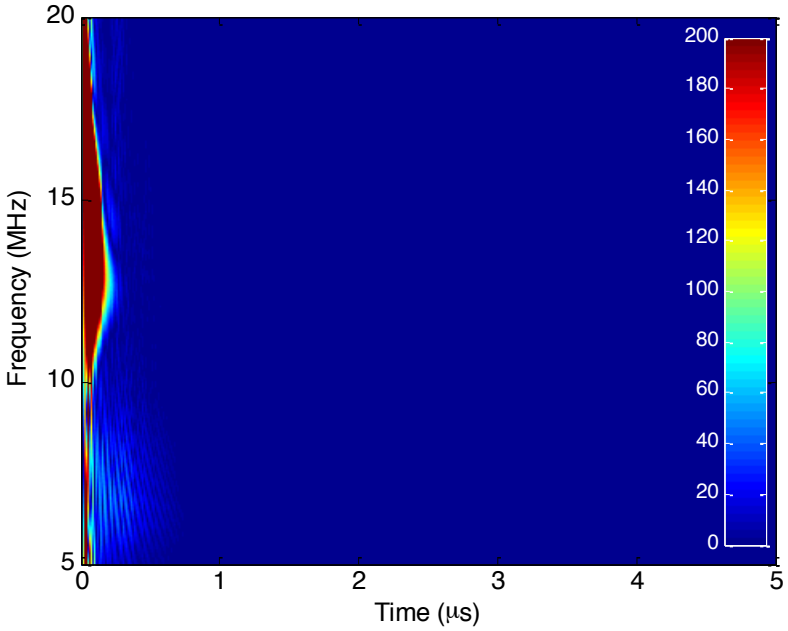


(b)

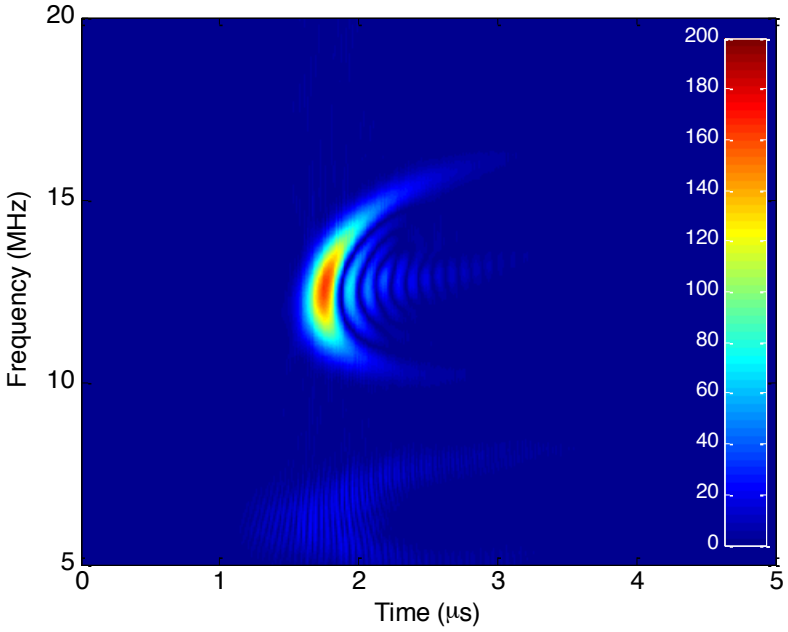


Figure 4.12 Smoothed WVD of MI signal: (a) Coil 2 (b) Coil 40

In time domain, the time-of-flight is determined from the corresponding peak in the smoothed WVD for each frequency component. Then the group velocity equals the travel distance over the time of flight. First, we observe propagating MI waves and the calculated smooth WVD of MI waves at two different locations—Coil 2 and Coil 40. Figure 4.12 shows the smoothed WVD of the MI waves at Coil 2 and Coil 40.

If we plot out the smoothed WVD of the MI signal only as a function of time at a single frequency, the corresponding peak value time can be seen clearly. Smoothed WVD of MI waves at Coil 2 and Coil 40 at a frequency of 12 MHz are shown below. The smoothed WVD curve is normalized to its maximum smoothed WVD value at 12MHz. The time corresponding to the peak for Coil 2 and Coil 40 are 0.07 μs and 1.74 μs, so the time of flight is 1.67 $\mu$s. Given the distance of 0.545 m, the extracted group velocity is around 326.8 km/s at a frequency of 12 MHz. We use this method to estimate group velocity over the passband, and the results are shown in Figure 4.14. The agreement with simulated results is adequate for a group velocity diagram. Given the group velocity, TFRs of the MI signal can be used to decide the travel distance by extracting time information.

(a)

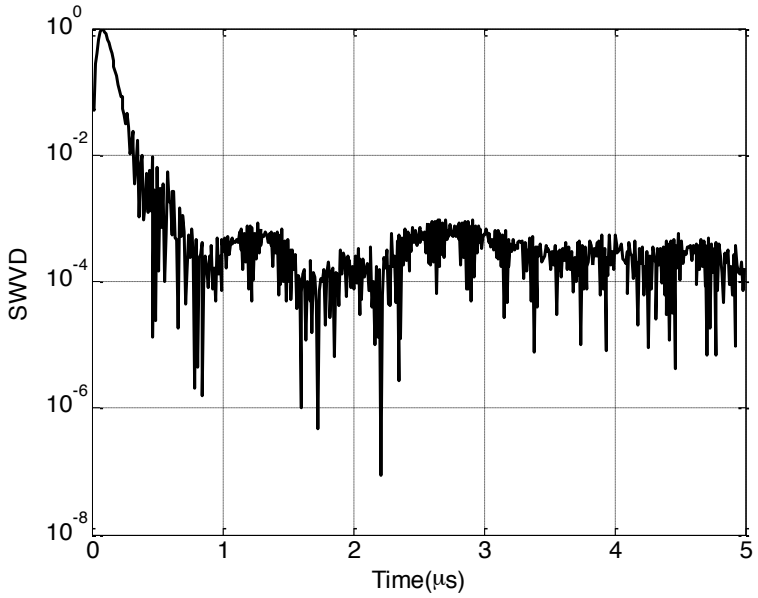


(b)

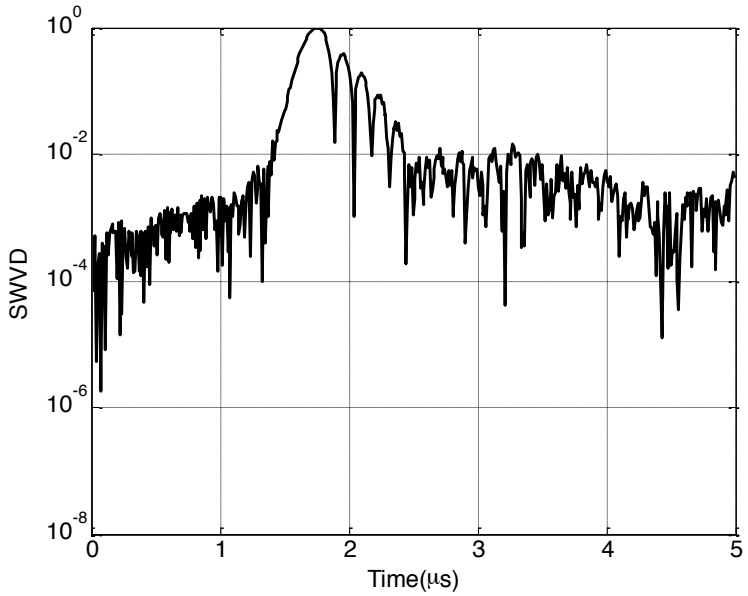


Figure 4.13 Smoothed WVD of MI signal at 12MHz: (a) Coil 2 (b) Coil 40

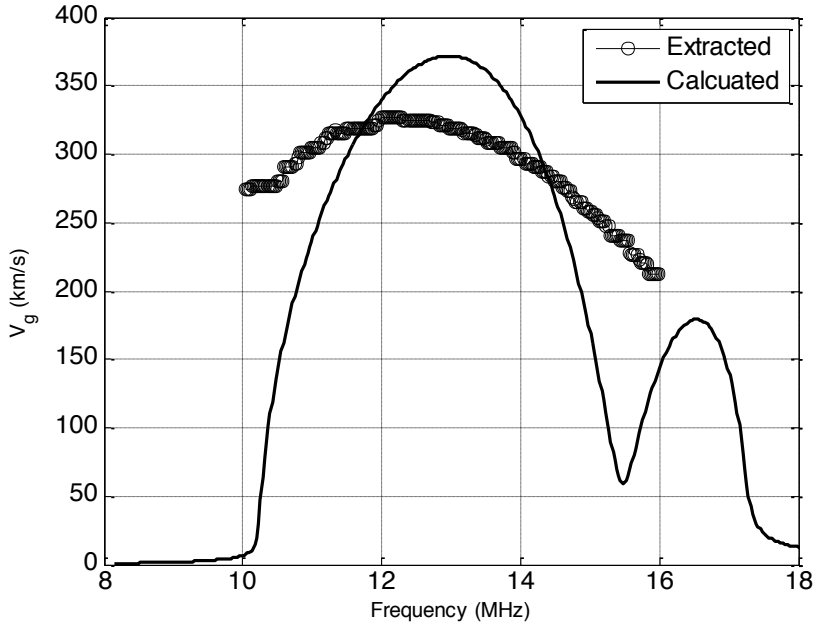


Figure 4.14 Extracted group velocity of MI waves

## 4.4 VALIDATIONS OF SENSING MECHANISM

The sensing mechanisms proposed in Section 3.2.3 and 3.3.3 are based on the analysis of MI waves in the time domain. In this section, a measurement system is designed to measure the reflected MI signal. The set-up in the previous section cannot locate discontinuity along an MI waveguide because only the transmitted signal is measured and the arrival time is not effected by the defect location. The digitizer needs to be placed at the first element to capture the reflected waves. The pulse-echo experimental setup is provided, and the measurement results of a 40-element MI waveguide with differing location of defect are provided. The time domain measurements illustrate reflections that take place when discontinuity exists in the line.

### 4.4.1 Time Domain Experimental Setup

The schematic diagram to measure reflected MI waves is shown in Figure 4.15.

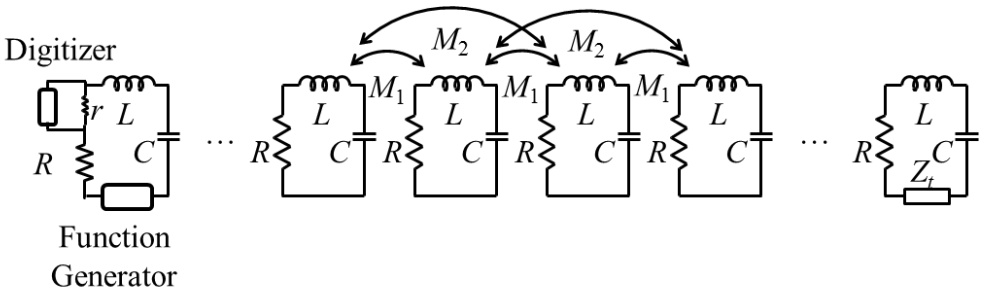


Figure 4.15 Schematic diagram of MI waveguide for pulse-echo measurement setup

In Figure 4.15, the first coil differs from what we used in the previous section. A small resistor with $R$=2.7Ω is added at the first coil as a voltage sensor. The voltage across the resistor is collected by the digitizer, which provides information about both the incident and reflected MI signal. The real measurement system is shown in Figure 4.14.

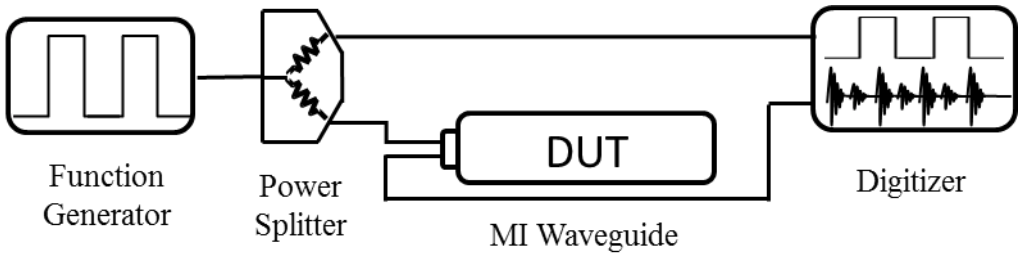


Figure 4.16 Schematic diagram of pulse-echo measurement setup

Figure 4.16 shows the measurement system constructed with the same equipment in Figure 4.8 but connected another way. The input square signal arrives at the first coil after a 3-db power splitter and the voltage across a 2.7Ω resistor is recorded by the digitizer. The copy of an input rectangular signal is also monitored by the digitizer through another output of the 3-db power splitter.

### 4.4.2 Results and Validations

The MI waveguide consist of an array of equally spaced 40 PSCs that resonate at 13.56 MHz. The voltage of extra 2.7Ω resistor in series with the first resonant circuit component is

recorded to monitor the reflected MI signal. The photo of the pluse-echo measurement setup is shown in Figure 4.17.

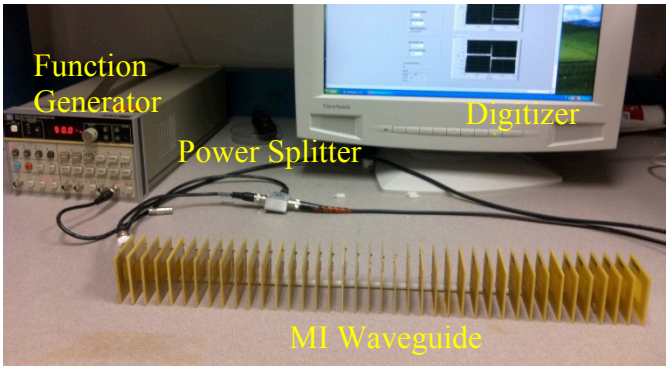


Figure 4.17 Photo of pulse-echo measurement setup

A defect is introduced by making the resonant circuit open at a specific location. The current signals through the resistor with differing locations of defect are shown below.

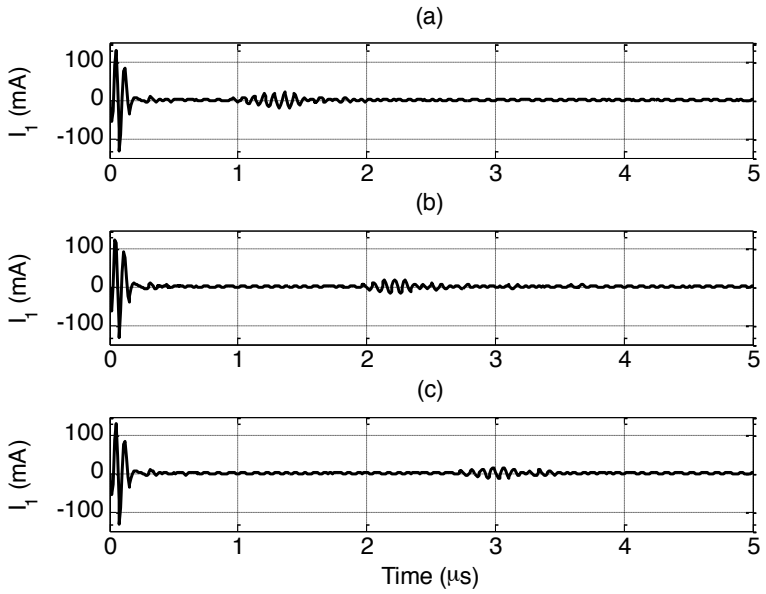


Figure 4. 18 Measured transient current with different location of defect: (a) Coil 15 (b) Coil 25 (c) Coil 35

Figure 4.18 is the time-domain signal with a different location of defect in our waveguide. We can see the burst signal with three cycles in each plot at the beginning of the test, which represents the initiation of the MI waves at the first element. A much weaker burst

observed later is the reflected signal by the intended defect along the MI waveguide. The smoothed SWD of the transient current is shown in Figure 4.19. With defect at Coil 15, the maximum spectral amplitude occurring at a frequency of 12 MHz is observed at 1.32 μs. The time of flight for reflected waves with defect 25 and defect 35 are 2.17μs and 2.98μs, respectively. The group velocity is known to be 326.8 km/s from the previous section. The estimated round-trip travel distance $l$ should be 0.43 m, 0.71 m, and 0.97 m.

The number of defective elements is defined by $l/2/d_c$, where $d_c$ is center-to-center distance between two coaxial PSCs. Since the gap between elements is 1.27 cm and the substrate thickness is 0.16 cm, the defect is supposed to occur at Coil 15, Coil 25, and Coil 34. The estimated value has one tag difference when the defect is at Coil 35.

(a)

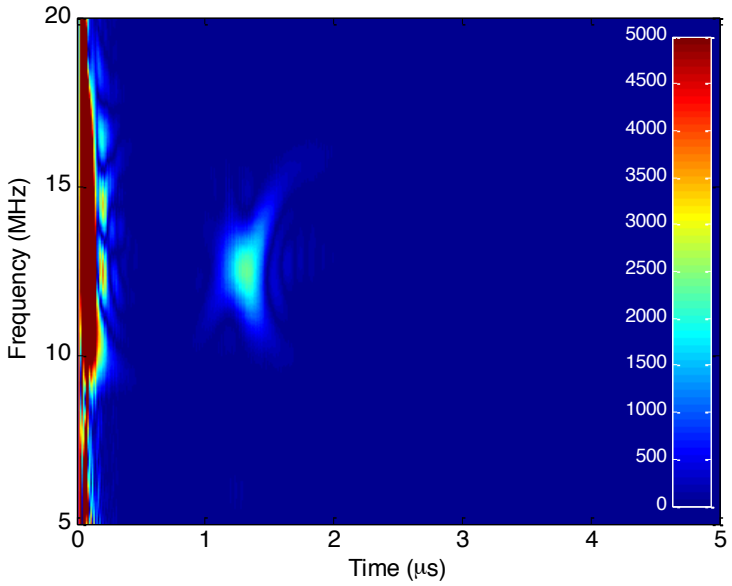


Dgespc 4.19

(b)

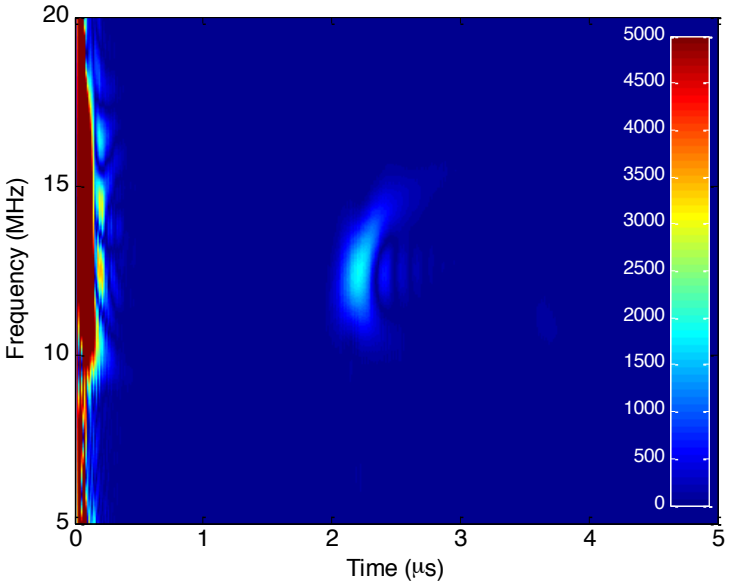


(c)

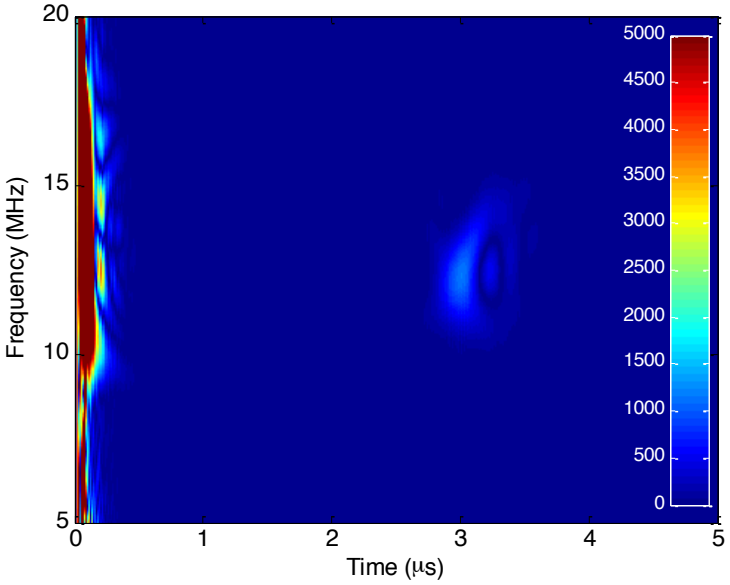


Figure 4.19 Smoothed WVD of MI signal with reflections (a) Coil 15; (b) Coil 25; (c) Coil 35

From the analysis above, the smoothed WVD can effectively generate the envelope of time-varying MI waves and present the time-frequency information. MI waves show great potential in detecting defects, which introduces discontinuities and give rise to reflected waves.

## 4.5 SUMMARY

One-dimensional MI waveguides with and without defect have been tested in this chapter. In the frequency domain, the insertion loss of MI waveguides without defects was measured with different spacings and lengths. A 0.098 dB loss per tag was achieved by PSCs designed in Chapter 2 at separation of half an inch. In the time domain, the measurement systems were built by a function generator, a 3-dB power splitter, and digitizer to monitor both incident and reflected MI signal. The group velocity for low-loss MI waveguides was extracted by the TFR of traveling MI signals, and the maximum group velocity was found to be at 326.8 km/s. For the MI waveguide in meters, the time of flight could be observed by a digitizer with a sampling rate of 100 MHz. The reflected waves were collected at the first coil to demonstrate a method to detect one defect along the waveguide. The arrival time was used to estimate the traveling distance with group velocity.

MI waveguides with distributed defects were also tested. The uniform defects resulted in a different set of supported waves. End reflections with different amplitude and arrival time were monitored due to modified characteristic impedance and group velocity. With known length information, the updated group velocity was obtained, and then the circuit parameter change introduced by different transducers was concluded.

# Chapter 5 Conclusions

To make use of MI waves for sensing applications, the characteristics of MI waveguides with different kinds of defects were studied, and the corresponding sensing mechanisms were validated in this work.

MI waveguide was a periodic magnetically-coupled resonator array. The single-layer square-shaped PSC with lumped capacitor was adopted as the resonant element. The performance of coil was optimized by adjusting its geometric parameters using well-established design methodology. The designed PSCs were fabricated on the FR-4 substrate and measured with an impedance analyzer. Their resonant frequency was 13.6±0.1 MHz with a quality factor of 161±12. A high-$Q$ component with strong magnetic coupling was shown to be necessary to achieve low propagation loss and support strong signal. Then the one-dimensional MI waveguide was constructed by a line of coaxially placed PSCs, and their characteristics were studied with a lumped-element circuit model. The dispersion relationship showed that the MI waveguide could support a set of slow waves around the resonant frequency. The bandwidth was proportional to the magnetic coupling strength. The group velocity was also derived using the dispersion relationship. When building the MI waveguide, it was determined that the circuit component tolerance could not be overlooked either. The effect of tolerances on delivered power was also studied, and findings revealed that it is best to have a tolerance of less than 5 percent.

MI waveguides with the one and distributed defects were then investigated. The transmission and reflection coefficients were solved as function of frequency and impedance match based on the circuit model of MI waveguides. MI waves in the time domain were simulated with PSpice. Its sinc-like shape was owing to passband frequency characteristics.

Multiplying the time of flight with group velocity determined the position of defect. MI waveguides with distributed impedance did not introduce reflected waves inside the guide because the modified impedance were same along the line. But strong end reflections and different arrival times could be introduced, depending on the type of transducers used. Given the known MI waveguide length, the updated group velocity was obtained by monitoring end reflections. The circuit parameter change due to transducer is deduced by the new group velocity.

One-dimensional MI waveguides with and without defects were built and tested in both frequency and time domains. In the frequency domain, it was verified that the design of the MI waveguide could have propagation loss as low as 0.098 dB per tag at separation of half an inch. In the time domain, the group velocity for low-loss MI waveguides was extracted by time frequency representations of traveling MI signals. The maximum group velocity was 326.8 km/s. For MI waveguide in meters, the time of flight could be captured by a digitizer with a sampling rate of 100 MHz. The reflected waves were collected and processed, and the results validated the sensing mechanisms for the detection of one defect along the waveguide. MI waveguides with distributed defects were also tested. The uniform defects resulted in a different set of supported waves. End reflections were monitored to deduce the kind of circuit parameter change introduced by different transducers. The experiments demonstrated that the sensing mechanism works for the MI waveguide.

The first possibility of the future work is to embed MI waveguide with transducers in concrete. The periodic array would provide a read range larger than the single embedded sensor, and new measurement techniques based on time-domain signals may be developed. The second possibility of future work is to explore the use of the MI waveguide as a strain gauge. Different resonant elements may be designed, and the group velocity change can be monitored based on

the shape transform. Finally, it may be possible to use MI waveguides as a discrete power source or transmitter. Each element could be designed for incorporating NFC technology.

## References


[1] J. B. Pendry, "Negative Refraction Makes a Perfect Lens," *Physical Review Letters,* vol. 85, p. 3966, 2000.

[2] E. Shamonina, V. Kalinin, K. H. Ringhofer, and L. Solymar, "Magneto-inductive waveguide," *Electronics Letters,* vol. 38, pp. 371-373, 2002.

[3] C. R. Simovski and P. A. Belov, "Backward wave region and negative material parameters of a structure formed by lattices of wires and split-ring resonators," in *Antennas and Propagation Society International Symposium, 2003. IEEE*, 2003, pp. 659-662 vol.4.

[4] R. R. A. Syms, E. Shamonina, and L. Solymar, "Magneto-inductive waveguide devices," *Microwaves, Antennas and Propagation, IEE Proceedings -,* vol. 153, pp. 111-121, 2006.

[5] E. S. a. L. Solymar, "Magneto-inductive waves supported by metamaterial elements: components for a one-dimensional waveguide." vol. 37, 2004, p. 362.

[6] M. C. K. Wiltshire, E. Shamonina, I. R. Young, and L. Solymar, "Dispersion characteristics of magneto-inductive waves: comparison between theory and experiment," *Electronics Letters,* vol. 39, pp. 215-217, 2003.

[7] R. R. A. Syms, L. Solymar, and E. Shamonina, "Absorbing terminations for magneto-inductive waveguides," *Microwaves, Antennas and Propagation, IEE Proceedings -,* vol. 152, pp. 77-81, 2005.

[8] M. C. K. Wiltshire, E. Shamonina, I. R. Young, and L. Solymar, "Experimental and theoretical study of magneto-inductive waves supported by one-dimensional arrays of "swiss rolls"," *Journal of Applied Physics,* vol. 95, pp. 4488-4493, 2004.

[9] R. R. A. Syms and et al., "Low-loss magneto-inductive waveguides." vol. 39, 2006, p. 3945.

[10] M. J. Freire, R. Marques, F. Medina, M. A. G. Laso, and F. Martin, "Planar magnetoinductive wave transducers: Theory and applications," *Applied Physics Letters,* vol. 85, pp. 4439-4441, 2004.

[11] R. R. A. Syms, E. Shamonina, and L. Solymar, "Positive and negative refraction of magnetoinductive waves in two dimensions." vol. 46, 2005, pp. 301-308.

[12] M. J. Freire and R. Marques, "Planar magnetoinductive lens for three-dimensional subwavelength imaging," *Applied Physics Letters,* vol. 86, pp. 182505-182505-3, 2005.

[13] E. Shamonina, V. A. Kalinin, K. H. Ringhofer, and L. Solymar, "Magnetoinductive waves in one, two, and three dimensions," *Journal of Applied Physics,* vol. 92, pp. 6252-6261, 2002.

[14] C. W. T. Chan and C. J. Stevens, "Two-dimensional magneto-inductive wave data structures," in *Antennas and Propagation (EUCAP), Proceedings of the 5th European Conference on*, pp. 1071-1075.

[15] C. J. Stevens, C. W. T. Chan, K. Stamatis, and D. J. Edwards, "Magnetic Metamaterials as 1-D Data Transfer Channels: An Application for Magneto-Inductive Waves," *Microwave Theory and Techniques, IEEE Transactions on,* vol. 58, pp. 1248-1256, 2010.

[16] R. R. A. Syms and et al., "Broadband coupling transducers for magneto-inductive cables." vol. 43, 2010, p. 285003.

[17] S. Zhi and I. F. Akyildiz, "Magnetic Induction Communications for Wireless Underground Sensor Networks," *Antennas and Propagation, IEEE Transactions on,* vol. 58, pp. 2426-2435, 2010.

[18] S. Zhi and F. A. Ian, "Underground wireless communication using magnetic induction," in *Proceedings of the 2009 IEEE international conference on Communications* Dresden, Germany: IEEE Press, 2009.

[19] Z. Sun, P. Wang, M. C. Vuran, M. A. Al-Rodhaan, A. M. Al-Dhelaan, and I. F. Akyildiz, "MISE-PIPE: Magnetic induction-based wireless sensor networks for underground pipeline monitoring," *Ad Hoc Networks,* vol. 9, pp. 218-227, 2011.

[20] J. I. Agbinya and M. Masihpour, "Excitation methods for magneto inductive waveguide communication systems," in *Broadband and Biomedical Communications (IB2Com), 2010 Fifth International Conference on*, 2010, pp. 1-6.

[21] C. J. Stevens, C. W. T. Chan, K. Stamatis, and D. J. Edwards, "Magnetic Metamaterials as 1-D Data Transfer Channels: An Application for Magneto-Inductive Waves," *Microwave Theory and Techniques, IEEE Transactions on,* vol. 58, pp. 1248-1256.

[22] I. S. Nefedov and S. A. Tretyakov, "On potential applications of metamaterials for the design of broadband phase shifters," *Microwave and Optical Technology Letters,* vol. 45, pp. 98-102, 2005.

[23] Z. Sun and I. F. Akyildiz, "Magnetic induction communications for wireless underground sensor networks." vol. 58: IEEE, 2010, pp. 2426-2435.

[24] C. W. T. Chan and C. J. Stevensy, "Two-dimensional magneto-inductive wave data structures," in *Antennas and Propagation (EUCAP), Proceedings of the 5th European Conference on*, 2011, pp. 1071-1075.

[25] L. Solymar, O. Zhuromskyy, O. Sydoruk, E. Shamonina, I. R. Young, and R. R. A. Syms, "Rotational resonance of magnetoinductive waves: Basic concept and application to nuclear magnetic resonance," *Journal of Applied Physics*, vol. 99, pp. 123908-8, 2006.

[26] R. R. A. Syms and et al., "Thin-film magneto-inductive cables." vol. 43, 2010, p. 055102.

[27] P. Pasupathy, M. Zhuzhou, D. P. Neikirk, and S. L. Wood, "Unpowered resonant wireless sensor nets for structural health monitoring," in *Sensors, 2008 IEEE*: IEEE, 2008, pp. 697-700.

[28] Y. Chen, S. Munukutla, P. Pasupathy, D. P. Neikirk, and S. L. Wood, "Magneto-inductive waveguide as a passive wireless sensor net for structural health monitoring," in *SPIE Smart Structures and Materials+ Nondestructive Evaluation and Health Monitoring*: International Society for Optics and Photonics, pp. 764749-764749-9.

[29] Y. Chen, P. Pasupathy, T. Trivedi, D. P. Neikirk, and S. L. Wood, "Improved magneto-inductive waveguide as wireless sensor net for structural health monitoring," in *SPIE Smart Structures and Materials+ Nondestructive Evaluation and Health Monitoring*: International Society for Optics and Photonics, pp. 83472H-83472H-8.

[30] S. B. Chase, "Dynamics and field testing of bridges in the new millennium: A look forward," 1999.

[31] http://www.electrawatch.com/ECI.html.

[32] http://www.tinyos.net.

[33] S. Robert, M. Alan, P. Joseph, A. John, and C. David, "An analysis of a large scale habitat monitoring application," in *Proceedings of the 2nd international conference on Embedded networked sensor systems* Baltimore, MD, USA: ACM, 2004.

[34] K. Sukun, S. Pakzad, D. Culler, J. Demmel, G. Fenves, S. Glaser, and M. Turon, "Health Monitoring of Civil Infrastructures Using Wireless Sensor Networks," in *Information Processing in Sensor Networks, 2007. IPSN 2007. 6th International Symposium on*, 2007, pp. 254-263.

[35] M. M. Andringa, D. P. Neikirk, and S. L. Wood, "Unpowered wireless analog resistance sensor," in *Smart Structures and Materials*: International Society for Optics and Photonics, 2004, pp. 356-367.

[36] M. M. Andringa, D. P. Neikirk, N. P. Dickerson, and S. L. Wood, "Unpowered wireless corrosion sensor for steel reinforced concrete," in *Sensors, 2005 IEEE*: IEEE, 2005, p. 4 pp.

[37] M. M. Andringa, J. M. Puryear, D. P. Neikirk, and S. L. Wood, "Low-cost wireless corrosion and conductivity sensors," in *Smart Structures and Materials*: International Society for Optics and Photonics, 2006, pp. 61740X-61740X-9.

[38] M. M. Andringa, J. M. Puryear, D. P. Neikirk, and S. L. Wood, "In situ measurement of conductivity and temperature during concrete curing using passive wireless sensors," in *The 14th International Symposium on: Smart Structures and Materials & Nondestructive Evaluation and Health Monitoring*: International Society for Optics and Photonics, 2007, pp. 65293M-65293M-10.

[39] N. P. Dickerson, M. M. Andringa, J. M. Puryear, S. L. Wood, and D. P. Neikirk, "Wireless threshold sensors for detecting corrosion in reinforced concrete structures," in *Smart Structures and Materials*: International Society for Optics and Photonics, 2006, pp. 61741L-61741L-8.

[40] N. P. Dickerson, J. T. Simonen, M. M. Ardringa, S. L. Wood, and D. P. Neikirk, "Wireless low-cost corrosion sensors for reinforced concrete structures," in *Smart Structures and Materials*: International Society for Optics and Photonics, 2005, pp. 493-503.

[41] P. Pasupathy, D. P. Neikirk, and S. L. Wood, "Improved reading techniques for electronic structural surveillance tags," in *The 15th International Symposium on: Smart Structures and Materials & Nondestructive Evaluation and Health Monitoring*: International Society for Optics and Photonics, 2008, pp. 693214-693214-12.

[42] P. Pasupathy, S. Munukutla, D. P. Neikirk, and S. L. Wood, "Versatile wireless sacrificial transducers for electronic structural surveillance sensors," in *Sensors, 2009 IEEE*: IEEE, 2009, pp. 979-983.

[43] A. Radkovskaya, O. Sydoruk, M. Shamonin, C. J. Stevens, G. Faulkner, D. J. Edwards, E. Shamonina, and L. Solymar, "Transmission properties of two shifted magnetoinductive waveguides," *Microwave and Optical Technology Letters,* vol. 49, pp. 1054-1058, 2007.

[44] R. R. A. Syms, O. Sydoruk, E. Shamonina, and L. Solymar, "Higher order interactions in magneto-inductive waveguides," *Metamaterials,* vol. 1, pp. 44-51, 2007.

[45] R. R. A. Syms, L. Solymar, and I. R. Young, "Three-frequency parametric amplification in magneto-inductive ring resonators," *Metamaterials,* vol. 2, pp. 122-134, 2008.

[46] I. Gil, J. Bonache, J. Garcia-Garcia, and F. Martin, "Tunable metamaterial transmission lines based on varactor-loaded split-ring resonators," *Microwave Theory and Techniques, IEEE Transactions on,* vol. 54, pp. 2665-2674, 2006.

[47] A. Radkovskaya, O. Sydoruk, M. Shamonin, E. Shamonina, C. J. Stevens, G. Faulkner, D. J. Edwards, and L. Solymar, "Experimental study of a bi-periodic magnetoinductive waveguide: comparison with theory," *Microwaves, Antennas & Propagation, IET,* vol. 1, pp. 80-83, 2007.

[48] R. R. A. Syms and L. Solymar, "Bends in magneto-inductive waveguides," *Metamaterials,* vol. 4, pp. 161-169, 2010.

[49] A. Radkovskaya, M. Shamonin, C. J. Stevens, G. Faulkner, D. J. Edwards, E. Shamonina, and L. Solymar, "An experimental study of the properties of magnetoinductive waves in the presence of retardation," *J Magn Magn Mater,* vol. 300, pp. 4-4, 2006.

[50] J. Uei-Ming and M. Ghovanloo, "Design and Optimization of Printed Spiral Coils for Efficient Inductive Power Transmission," in *Electronics, Circuits and Systems, 2007. ICECS 2007. 14th IEEE International Conference on*, 2007, pp. 70-73.

[51] S. S. Mohan, M. del Mar Hershenson, S. P. Boyd, and T. H. Lee, "Simple accurate expressions for planar spiral inductances," *Solid-State Circuits, IEEE Journal of,* vol. 34, pp. 1419-1424, 1999.

[52] H. M. Greenhouse, "Design of Planar Rectangular Microelectronic Inductors," *Parts, Hybrids, and Packaging, IEEE Transactions on,* vol. 10, pp. 101-109, 1974.

[53] M. Niethammer, L. J. Jacobs, J. Qu, and J. Jarzynski, "Time-frequency representations of Lamb waves." vol. 109, 2001, pp. 1841-1847.